POLITECNICO
MILANO 1863

SCUOLA DI INGEGNERIA INDUSTRIALE
E DELL'INFORMAZIONE

TU Delft

Delft University of Technology

Application of body force modeling to aeroengine fan blade design

Tesi di Laurea Magistrale in
Aeronautical Engineering - Ingegneria Aeronautica

Author: **Gabriele Morvillo**

Student ID: 925784
Advisor: Prof. Paolo Gaetani
Co-advisors: PhD Evert Bunschoten
Academic Year: 2020-2021

Alla mia famiglia.

Abstract

In connection with the constant strife for commercial aeronautical engines performances improvement, an investigation of an alternative fluid dynamic simulation model for fan blade design has been performed.

A study has been carried out regarding the application of body force modeling to fan blades shape optimization, looking for an efficient and reliable design tool, able to replace the state of the art expensive 3D simulation programs. The referred model was analyzed for the NASA Rotor 67 testcase in order to evaluate the computational time, the accuracy and the sensibility to blade design variables with respect to other commonly used high-fidelity methods. An almost completely automated design cycle has been implemented, allowing the user to evaluate different geometries and design solution by writing a single input file.

From the results it emerges that the overall performance of the stage predicted by BFM are slightly different from what can be obtained with higher fidelity computations. Moreover the obtained computation time reduction factor is greater than 3 orders of magnitude. On the other hand the model fails to represent the local 3D nature of the flow across the blade region, not being able to capture the supersonic behaviour induced by the physical blade. This and the stratification of results result in the significant discrepancies between design variables sensitivities, making the shape optimization not feasible at the moment.

The conclusion is that the proposed model constitutes a reasonable preliminary design tool for supersonic fan, but not accurate enough to be applied in shape optimization yet. Despite this limitation the research was able to delineate the major areas of development for future studies on the model.

Keywords: Fan, design, CFD, body-force model, rotor67, sensitivity analysis

Abstract in lingua italiana

Il settore commerciale aeronautico e' costantemente alla ricerca di aumentare le performance dei motori per aeromobili. A tal proposito, in questa tesi, e' stato analizzato un modello di CFD alternativo per il design di pale nei turbofan.

Nel presente lavoro e' stata studiata la possibile applicazione del 'body-force model' (BFM) nell'ottimizzazione di design per pale di fan. Lo scopo e' quello di ottenere uno strumento di design accurato e veloce, che possa sostituire le tipiche metodologie di simulazione fluidodinamica dall'elevato costo computazionale. Il modello citato e' stato analizzato nel caso del Rotor67 della NASA, al fine di valutare il tempo computazionale, l'accuratezza e la sensibilita' alle variabili di design rispetto a quanto ottenibile con le simulazioni classiche. Seguendo un'ottica di design, nel presente studio, e' stato costruito un ciclo quasi completamente automatizzato, che permettesse di valutare molteplici geometrie e soluzioni a partire da un singolo file di input.

Dai risultati ottenuti si evince che le performance generali predette tramite BFM si discostino di poco da quanto si ottenga con classici metodi piu' accurati. Inoltre il tempo di calcolo risulta ridursi di piu' di 3 ordini di grandezza. Purtroppo pero' il modello non appare capace di catturare la complessa natura tridimensionale del flusso, in quanto non e' in grado di riprodure il corretto comportamento supersonico indotto dalla pala. Questo, unito anche alla stratificazione del flusso riscontrata, porta a differenze significative nella sensibilita' alle variabili di design, rendendo al momento infattibile procedere all'ottimizzazione della geometria.

Dalla ricerca risulta che il modello proposto costituisca un ragionevole strumento di design preliminare, ma non sia abbastanza accurato per essere applicato in processi di ottimizzazione. Il lavoro e' tuttavia stato utile a determinare i punti di forza e le limitazioni dell'attuale implementazione, delineando le basi per studi futuri.

Parole chiave: Fan, design, CFD, body-force model, rotor67, sensitivity analysis

Contents

1 | Introduction

1.1. Research motivations

The aeronautic industry is constantly striving to reduce fuel consumption and pollutant emissions. One of the major stagnation factor is the design of more efficient turbofan engines, which improvement seems to be limited by a required paradigm shift in the current configuration.

Recent turbofan development trend (see Fig.1.1) highlights that higher fan bypass ratio and lower pressure ratio [12] are required to increase these machines performances. These changes would in fact result in significant increases in propulsive efficiency, while maintaining thrust requirements, as it can be concluded from the turbofan efficiency and thrust formulas hereby reported:

$$\eta_{propulsive} = \frac{2}{1 + \frac{u_e}{u_{fs}}} \tag{1.1}$$

$$F = \dot{m}(u_e - u_{fs}) \tag{1.2}$$

where u_e is the jet exhaust velocity and u_{fs} is the free stream velocity of the external flow. The pressure ratio increase does in fact reduce the velocity difference, which in turns raise the engine efficiency. At the same time the thrust produced can be kept constant by processing greater mass flow using larger machine diameters.

Several solutions have been proposed, such as large dimensions geared fan, which come with the drawback of greater drag and weight penalties, and in-wake placed engines, which would make use of the low-momentum wake produced by the aircraft to generate thrust. A peculiarity linking these alternatives is the presence of a significant boundary layer ingestion (BLI) that would inevitably affect the flow pattern at the fan inlet. Such BLI has been shown to be a possible positive effect in the efficiency rise as presented in [25].

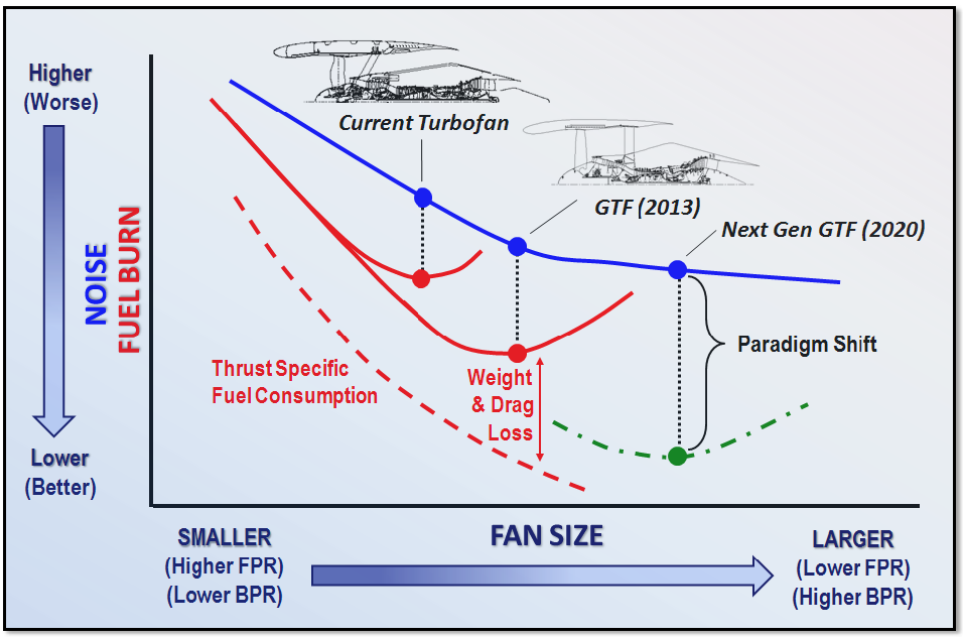

Figure 1.1: Turbofan development trend [12] highlights the short geared engines promising performances.

The BLI alters the flow pattern at the fan inlet, making in non symmetric and creating 3D unsteady effects. In order to study this effects the use of current high-fidelity CFD methods is not practically feasible: even though they can well represent the full-annulus 3D flow they are too computationally expensive to fully capture the unsteady nature of the problem.

The alternative many researchers have adopted is the use of Body Force Modeling (BFM). Such method has already been implemented by different authors, but not yet applied in the design phase of the engine except from preliminary computations as far as the writer knows. The key principle this formulation is to replace the physical blade with a volumetric force field and to model the flow turning and the losses separately. Such artifice would grant a remarkable computational time saving thanks to the coarser mesh, while at the same time produces results with reasonable level of accuracy [23].

The scope of this thesis is to verify the applicability of BFM to the design of an aeronautical fan, both in terms of computational cost and level of fidelity, and to produce an automated design workflow.

1.2. Research questions

As a means to carry out this thesis a set of guiding research questions has to be asked:

1. **What are the differences between BFM and physical blade transonic fan simulations results?**
   (a) **Which level of domain discretization is required to achieve grid convergence in BFM?** This question is fundamental to make the comparison between BFM and common CFD methods possible. The influence of difference mesh parameters over the results must be assessed thoroughly.
   (b) **What discrepancies can be found in terms of global and local flow characteristics?** The complex nature of the flow heavily influences the efficiency of transonic fans. In order to apply BFM as a design tool, the model must capture this complex flow characteristics.
   (c) **How do the simulation results differ between the two BFM implementations in SU2? What are the results differences between single-passage and full-annulus simulations?** The comparison of different BFM formulations can help understand the implementation quality of each method and their suitability to axial symmetric or distorted 3D flows.
2. **To which degree can BFM approach be used for blade shape optimization in transonic fans?** In order to evaluate the applicability of this method as a design tool two things must be checked: the efficiency (time required to perform the simulation) and the effectiveness (accuracy of the simulation).
   (a) **What level of time saving with respect to classical approach can be achieved with this model?** The computational time for the various method adopted must be quantified.
   (b) **How close are the sensitivity analysis results from BFM and physical blade simulations?** With the aim of applying the BFM in a optimization cycle, such as a gradient-based optimization, the sensitivity of the overall results to the design variables must be assessed. If the procedure produces significantly different outcomes then the optimization cannot be performed at the time being.
   (c) **Which features must be implemented in order to improve BFM design applicability?** The results of the analysis will eventually delineate the way to improve the proposed methodology with the aim of future design application.

1.3. Thesis structure

With the aim to answer the main research question this report has been divided into 6 sections. In chapter 2 the main literature text used for this work is reported. Here the physical principles at the base of BFM can be found as well as their integration into an automated design workflow. Chapter 3 shows the programs used for the study and their settings as well as their connection to recreate an automated workflow for the whole process. In the subsequent chapters 4 and 5 the computations performed to evaluate respectively the BFM flow behaviour and the sensitivity analysis are described. Here the time efficiency and the global accuracy of the approach are also depicted and comparison plot between BFM and classical approach are shown. Additional plots for the exhaustive description of the turbomachinery flow pattern can be found in the appendices. Lastly in chapter 6 the reader can look at the final conclusions and suggestions for future work.

The main structure and conclusions found in this work can also be found in the attached executive summary [10].

2 | Literature review

In this chapter the background knowledge regarding body-force modeling and blade shape optimization is reported. This technique will be confronted, throughout this work, with the common simulation procedure used in computational fluid dynamic, hereby referred to as "physical blade computation" (PBC), a term used to distinguish the presence of substantial blades in the domain, in opposition to BFM simulation.

2.1. Body force model

Body-force model (BFM) was first theorized by Marble in 1964 [16] as a mean of reproducing an axisymmetric blade row by substituting the blades with an equivalent force field (see fig.2.1). These forces model the flow deflection through source terms in the governing flow equations.

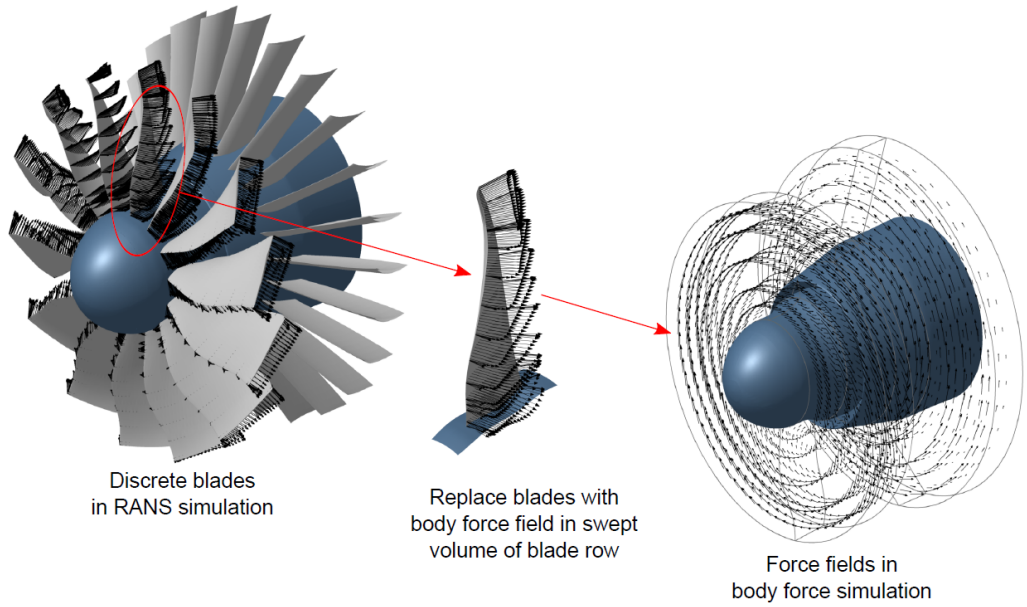

Figure 2.1: In BFM the fan physical blades are replaced with a circumferential averaged force field [19].

The main advantages of such method can be found in the coarser mesh required for the simulation: because of the physical blade absence, it is not necessary to model the blade boundary layer. As a consequence BFM can adopt a less refined mesh, while the BL effect can be accounted for using a separated correction. Despite the benefit in terms of computational cost this involves the drawback of requiring a complex study for losses, since it's no more possible to capture the wake behaviour or shock interactions with BL. Another advantage is the absence mixing plane between turbomachinery rows since the channel can now be represented as a single mesh zone which presents different source terms across the various sections.

Following Marble's work several researchers have adopted and developed such method for different applications (see [13], [20]) . Between these methods it is possibile to distinguish two general categories: the 2D throughflow methods and the 3D ones.

The 2D methods are the simplest ones and they constitute quick initial design instruments commonly used for turbomachinery projects. In this category it is indeed found the Streamline Curvature method (SLC) and the axisymmetric Euler throughflow one. Both rely on solving the equilibrium over streamlines that are bent according to the blade shape. The limitations of these methods come in the form of necessary empirical relations for losses due to their intrinsic 2D nature.

The 3D methods constitute a wide class of techniques able to represent more complex geometries without the need for empirical correlations. They represent a good candidate for blade shape optimization and also for taking into account possible instabilities at the inlet of the engine, one of the main point of interest of BFM in the BLI research field. Between these methods another subdivision can be made according to Thollet [23]:

- Explicit body force models, in which the turning forces imposed by the blades and the losses are directly modeled using first base principles instead of empirical correlations;
- Interpolation from database, in which the forces extraction relies on previous RANS simulations to generate a look-up table;
- Semi-explicit models, similar to explicit ones but with some of the variables computed by means of empirical relations;
- Immersed boundary, in which, instead of modeling explicit forces, the 3D flow turning is prescribed similarly to the 2D throughflow methods;
- other approaches to fit specific machines issue such as wake modeling.

Due to the nature of this thesis the an explicit procedure constitutes the most suited approach. This is the kind of model it is used since it allows for the local computation of the flow and does not require for previous database generation, allowing this way to evaluate the effect of shape parameters change over the overall fan performance. The two explicit processes currently implemented in SU2 (Hall and Thollet) are hereby reported.

2.1.1. Governing equations

As previously mentioned the model is based on the assumption of representing the blades effect on the flow adding source terms to the general equations. This can be reported in the differential form of the Navier Stokes equations at the base of CFD computation as follow:

$$\frac{\partial \rho}{\partial t} + \frac{\partial \rho u_i}{\partial x_i} = S_{BFM} \tag{2.1}$$

$$\frac{\partial \rho u_i}{\partial t} + \frac{\rho u_i u_j}{\partial x_j} = -\frac{\partial p}{\partial x_i} + \frac{\partial \tau_{ij}}{\partial x_j} + F_{BFM,i} \tag{2.2}$$

$$\frac{\partial \rho e_t}{\partial t} + \frac{\partial (\rho u_i h_t)}{\partial x_i} = -\frac{\partial q_i}{\partial x_i} + \frac{\partial (\tau_{ij} v_i)}{\partial x_j} + \dot{Q}_{BFM} \tag{2.3}$$

In which the only volumetric source terms considered are the one coming from body-force model. In particular S_{BFM} is the BFM continuity source term, $F_{BFM,i}$ is the body-force vector governing flow deflection, and Q_{BFM} is the work of the body-forces applied to the flow.

The energy term introduced by the BFM can be represented as the total stagnation enthalpy introduced by rotating blades as

$$\dot{Q}_{BFM} = r\Omega F_{BFM,\theta} \tag{2.4}$$

Where r is the local radius, Ω is the angular velocity of the blade and $\dot{F}_{BFM,\theta}$ is the body-force in tangential direction.

The viscous term is generally neglected according to the need for an initial design not to exactly evaluate the flow behaviour. Such choice allows for faster resolution of the fluid problem. Some of the model proposed bring back the viscous effect into the computation modelling the blade losses in term of parallel force (see section 2.1.3), making the endwall viscous losses the only parameter effectively neglected. Without this contribution and neglecting boundary heat fluxes the system of equations appears to be

$$\frac{\partial}{\partial t}\begin{bmatrix}\rho\\ \rho u_1\\ \rho u_2\\ \rho u_3\\ \rho e_t\end{bmatrix}+\frac{\partial}{\partial x_i}\begin{bmatrix}\rho u_i\\ \rho u_i u_1+p\\ \rho u_i u_2+p\\ \rho u_i u_3+p\\ \rho u_i h_t\end{bmatrix}=\begin{bmatrix}S_{BFM}\\ F_{BFM_1}\\ F_{BFM_2}\\ F_{BFM_3}\\ r\Omega F_{BFM,\theta}\end{bmatrix} \tag{2.5}$$

2.1.2. Hall's formulation

Hall [9] presented in his work a interesting development of the previous successful method from Gong [26]. The model aims to reproduce the flow turning, pressure rise and temperature rise using a pitchwise averaged distribution of force field resembling the physical blade. These source terms are extracted by the 3D blade geometry and the local flow conditions in the blade row. In Gong's approach the momentum sources are decomposed in normal and parallel components, where the first is used to model flow turning and the second is used for the losses computation.

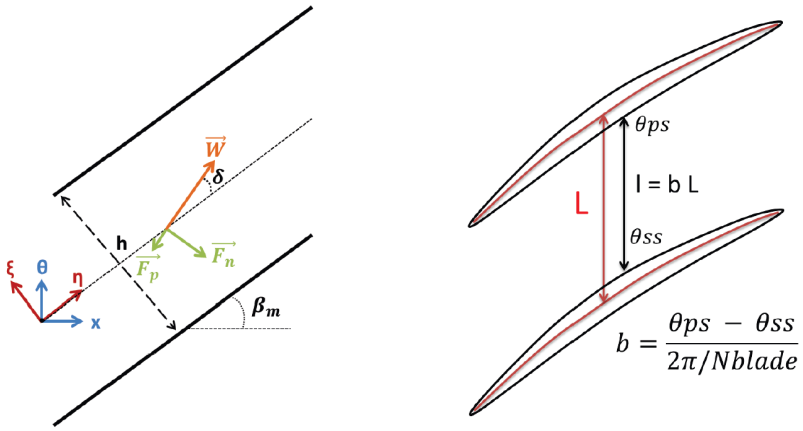

(a) Body forces decomposition (b) Blockage factor

Figure 2.2: BFM main contributions are represented in terms of forces decomposition from Gong's model (left) and of metal blade blockage introduced later by Thollet (right) [23].

In his work Hall opted to ignore the parallel loss component shown in Fig. 2.2a to focus on the normal one, aiming to obtain a completely local formulation of the BFM that does not require a previous calibration from single passage RANS as in Gong. Moreover he did not take into consideration the blade metal blockage over the mass flow through the channel. The source term S_{BFM} in eq. 2.5 is then equal to zero. This would lead to

higher mass flow rate with respect to the real one.

Hall's model main assumptions regarding the flow are:

- Incompressible;
- Inviscid;
- Quasy-steady;
- Locally axisymmetric.

The incompressible assumption has been subsequently corrected by Thollet ([23]) and such correction has been used to implement Hall's formulation on SU2 [14] because of the requirement to simulate turbomachinery compressible flows. The last two assumptions are easily met in case of axisymmetric inlet but as shown in [9] they can be respected also in case of BLI according to the high characteristic length of the circumferential distortion and the small time scale of the induced flow structures with respect to the throughflow ones.

The model force normal to the blade can be expressed as:

$$F_n = K_{Mach}\rho\pi W^2\delta\frac{1}{s|n_\theta|} \tag{2.6}$$

where K_{Mach} is the compressible correction, W is the relative velocity magnitude, δ is the local angle of attack, s is the blade pitch and n_θ is vector of camber normal projected in tangential direction.

The corrections reads:

$$K_{Mach} = \begin{cases} \min\left(\frac{1}{\sqrt{1-M_{rel}^2}}, 3\right), & M_{rel} < 1 \\ \min\left(\frac{4}{2\pi\sqrt{M_{rel}^2-1}}, 3\right), & M_{rel} > 1 \end{cases} \tag{2.7}$$

This force can then be defined in Cartesian space through algebraic transformations and inserted in the BFM equations (eq. 2.5) as the forcing term, obtaining:

$$\frac{\partial}{\partial t}\begin{bmatrix}\rho\\ \rho u_1\\ \rho u_2\\ \rho u_3\\ \rho e_t\end{bmatrix}+\frac{\partial}{\partial x_i}\begin{bmatrix}\rho u_i\\ \rho u_i u_1+p\\ \rho u_i u_2+p\\ \rho u_i u_3+p\\ \rho u_i h_t\end{bmatrix}=\begin{bmatrix}0\\ F_{n,1}\\ F_{n,2}\\ F_{n,3}\\ r\Omega F_{n,\theta}\end{bmatrix} \tag{2.8}$$

2.1.3. Thollet's formulation

In his work Thollet [23] resorted to Hall's BFM to develop a deeper representation of the flow physical behaviour. In order to do so he added three main aspects to the previous model:

- compressibility correction, as reported in eq. (2.7);
- metal blockage effect, to mimic the presence of physical blade on the mass flow passing through the channel;
- profile drag correction, to account for profile losses.

The metal blockage stands for the effect of the channel obstruction represented by the physical blade geometry. The thickness does in fact reduce the amount of area at disposal of the flow to pass through, inducing local acceleration and deceleration due to the equivalent converging and diverging channels. In order to represent this behaviour a geometric parameter called blockage factor b can be used. It must be noted that such parameter is not extensively accounting for all the mass change due to the blade presence since another contribution, not modeled by Thollet, is the aerodynamic blockage induced by the BL presence. Nonetheless the blockage factor will help in correcting the mass flow rate by introducing a new contribution to the right hand side forcing terms in BFM equations. This parameter can be defined by the sole geometry as

$$b=\frac{s'}{s} \tag{2.9}$$

Where s is the camberline bade pitch and s' is local effective faces pitch as shown in fig. 2.2b

$$s=\frac{2\pi r}{N_b}\quad and\quad s'=r(\theta_{PS}-\theta_{SS}) \tag{2.10}$$

b is inversely proportional to the local blade thickness. Thollet used the divergence of the blockage factor to add the acceleration contribution of decreasing b (decreasing section)

and the opposite in case of increasing one.

The other fundamental advancement introduced by Thollet is the modelization of viscous profile losses previously neglected by Hall. Such model will be postulated reintroducing the parallel force as shown in previous work such as Gong's one, with the difference this time of formulating it without the need for previous calibration. The main sources of losses that can be found in fan are profile losses, endwall losses (which enclose secondary ones) and shock losses. Of these three the endwall are generally low in value (see section 3.1.1) and neglected in BFM, while the shock losses are very case dependant and difficult to represent in terms of base first principles. Thollet therefore concentrate on representing the profile losses keeping in mind that the final efficiency will be nevertheless overstimated, with respect to usual high-fidelity methods, even if closer to the real one than in the Hall's simulation. The formulation used to represent profile losses makes use of the flat plate boundary layer loss model to reproduce the parallel force (see fig. 2.2a)

$$F_p = \rho C_f W^2 \frac{1}{sb|n_\theta|} \tag{2.11}$$

$$with \quad C_f = \frac{0.0592}{Re_{ax}^{-0.2}} \qquad Re_{ax} = \frac{\rho W(x - x_{LE})}{\mu} \tag{2.12}$$

where C_f relation has been obtained through reference data calibration. In the Re_{ax} formula $x - x_{LE}$ is the difference between generic chordwise section and LE axial position.

With the addition of the terms presented the BFM problem equations become:

$$\frac{\partial}{\partial t}\begin{bmatrix}\rho\\ \rho u_1\\ \rho u_2\\ \rho u_3\\ \rho e_t\end{bmatrix} + \frac{\partial}{\partial x_i}\begin{bmatrix}\rho u_i\\ \rho u_i u_1 + p\\ \rho u_i u_2 + p\\ \rho u_i u_3 + p\\ \rho u_i h_t\end{bmatrix} = \begin{bmatrix}0\\ F_{n,1} + F_{p,1}\\ F_{n,2} + F_{p,2}\\ F_{n,3} + F_{p,3}\\ r\Omega \dot{F}_{BFM,\theta}\end{bmatrix} - \frac{1}{b}\begin{bmatrix}\rho u_i \dfrac{\partial b}{\partial x_i}\\ \rho u_1 u_i \dfrac{\partial b}{\partial x_i}\\ \rho u_2 u_i \dfrac{\partial b}{\partial x_i}\\ \rho u_3 u_i \dfrac{\partial b}{\partial x_i}\\ \rho h_t u_i \dfrac{\partial b}{\partial x_i}\end{bmatrix} \tag{2.13}$$

2.2. Sensitivity analysis and blade shape optimization

In the search for improved efficiency the blade shape optimization represent a great opportunity for aeronautical field. Several attempts to increase the shape performances have been performed but a common pitfall can be found in the computational cost represented by standard high-fidelity models. Several alternatives have been explored such as quasi-3D simulations [15] or methamodel [6] but the limitations come in the form of accuracy or great number of calibration run requested. In this environment the BFM could represent a great trade-off option if set correctly.

The typical optimization problem can be formulated as

$$\begin{cases} min\ f_i(\boldsymbol{X})\ i = 1, ...l \\ subject\ to: g_j(\boldsymbol{X}) \leq 0,\ j = 1, ..., m \\ h_k(\boldsymbol{X}) = 0,\ k = 1, ...n \\ x_p^{min} \leq x_p \leq x_p^{max},\ p = 1, ..., q \end{cases} \tag{2.14}$$

Where f_i, g_j, h_i, x_p and $\boldsymbol{X}$ respectively stand for objective functions, inequality constraints, equality constraints, domain bounds and design variables vector. The turbomachinery case in general constitutes a complex multi-disciplinary design optimization problem as there are several functions f_i to be optimized.

It is possible to adopt numerous different optimization techniques to perform the desired design enhancement, but they can be generically subdivided into two main categories: gradient-free methods and gradient-based ones. The first are easier to implement and can handle discontinuous, noisy and multi-modal functions but require a huge amount of evaluation to find the optimum. This makes gradient-free methods not suited for computationally expensive processes as CFD. On the other hand the gradient-based approach is much more efficient in finding the result thanks to the search direction computed from the gradients. The drawbacks of this method are the poor performance in case of noise and the fact that it finds the local minimum instead of the global one. Nonetheless the gradient based optimization method has been proven itself fairly useful and has been used extensively in the field as shown in [14] and [15].

Due to the complexity of turbomachinery design problems and the number of variables involved some adjustment must be done prior the optimization. A fundamental and extremely useful tool to apply in such regard is the sensitivity analysis. The main advantages

of such method are:

- it identifies the most important variables and their influence over the objective functions, allowing for a preliminary screening of the unnecessary parameters;
- it allows to understand the performance output linked to a change in a certain parameter, giving the search direction to follow in gradient based optimization;
- helps to identify issues in the model and non-linearity, robustness and smoothness linked to specific variables.

Such advantages makes the performing of a preliminary sensitivity analysis an insightful check to understand whether or not the BFM implemented is in line with the high-fidelity simulation. According to the results an optimization run can then be executed.

In order to carry out a sensitivity analysis it is required a number of simulations is proportional to the design variables. The computational cost can then become prohibitively elevated if the parameters are numerous such as in the case of this thesis. Previous SU2 works (see [14]) used adjoint method to estimate sensitivity analysis for Hall's BFM without the need to perform a huge amount of runs. This method is based on the substitution of the flow derivatives over each design variables with an adjoint vector when computing the objective function derivative. Despite being an efficient approach, this method presents two limitations in terms of complexity to be implemented, and memory cost for the machine. Instead in this thesis it has been chosen to adopt classic finite difference method for sensitivity analysis. This approach comes with the downside of step size uncertainty and high computational cost. Since it provides easily accessible results for the preliminary S.A. and given the stress applied on the BFM time efficiency researched in this thesis, this method has been deemed more suitable in the limited time frame of the work.

3 | Design workflow settings

The aim of the present work is to apply the body-force model presented by Hall and Thollet on the design of transonic fan blades. In order to do so an automated process able to iterate over changing geometry has been build up. Almost the whole process has been enclosed in python environment to allow the user to perform a complete test in a single run. The only exception is represented by the comparison high-fidelity CFD simulations performed in ANSYS CFX [2]. Since they are severely time demanding they have not been inserted in the automated cycle, even if that was possible. Rather they have been performed on a separated high performance cluster (HPC) environment, making use of greater computational power.

The process can be subdivided into 3 different conceptual blocks:

- Blade geometry generation;
- CFD simulation;
- Sensitivity analysis and optimization.

The clear blocks distinction allows to operate and modify each one on its own, making the implementation of alternative features easy and accessible.

3.1. Blade geometry generation

In this section the design variables are defined and the parametric representation of the blade is carried out, reproducing a 3D geometry with the related files necessary to run the simulations.

The workflow created in this thesis can be used to create a the blade shape using the two programs called *Meangen* [8] and *Parablade* [1]. As shown in figure 3.1 a distinction must be made according to the kind of blade to be studied: if the blade is being designed from zero a conceptual meanline design (block 2) must be performed. This is necessary to obtain duty coefficients and generate the initial parameters for the 3D geometry with the help of Meangen (block 3). On the other hand, if the blade shape is available, Parablade can be

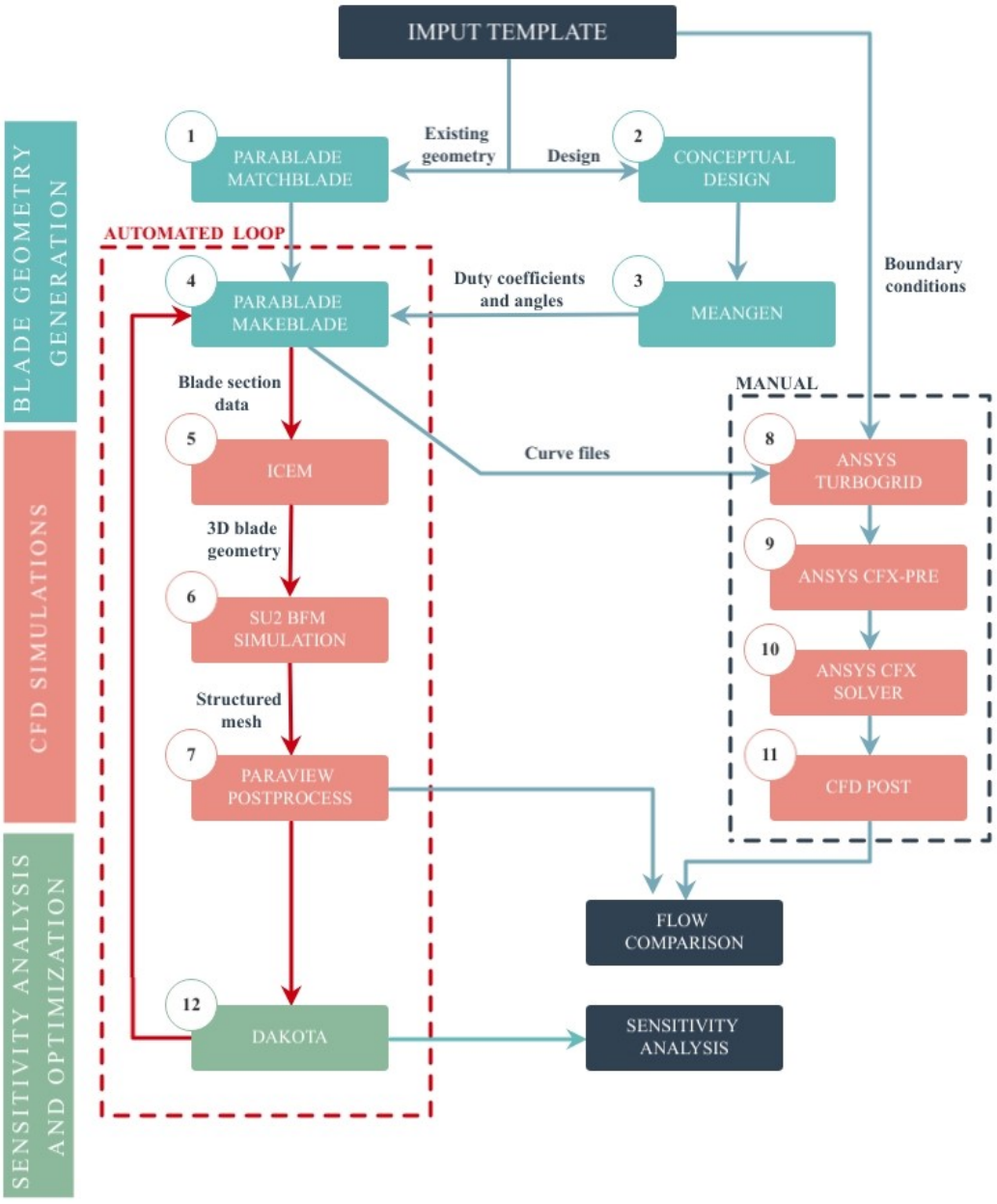

Figure 3.1: An almost automated process has been developed for BFM fan design. The workflow is subdivided in 3 main blocks linked together.

used to recover such parameters using the *MatchBlade* script. Once the design parameter are obtained the Parablade function *MakeBlade* (block 4) can be used to generate the 3D blade geometry.

3.1.1. Meangen

Meangen is a branch program of the 3D CFD solver Multall [8], a turbomachinery design system created by Prof. John Denton at Cambridge University. Meangen is a one-dimensional mean-line design program that from a set of duty coefficients, mass flow rate and estimation of incidence and deviation angle for each stage is able to recreate the meridional flow path of the turbomachine. It is fundamental to prescribe a previously computed efficiency ratio since the program is not able to compute it.

In the preliminary design of the blade it the losses to be account for are:

- profile losses, modeled with the Lieblein's approximation

$$Y_{Lieblein} = \frac{2\,\frac{\vartheta}{c}\frac{\sigma}{cos\beta_2}\left(\frac{cos\beta_1}{cos\beta_2}\right)^2\left(\frac{2H}{3H-1}\right)}{\left(1-\frac{\vartheta}{c}\frac{\sigma}{cos\beta_2}H\right)^3} \tag{3.1}$$

  Where ϑ is the boundary layer momentum thickness, c is the axial chord, σ is the solidity, β_1 and β_2 are respectively the inlet and outlet relative flow angles and H is the BL shape factor;

- Endwall and secondary losses, accounted for with Howell

$$Y_{Howell} = \frac{(C_{Da} - C_{Ds})\,\sigma\, cos^2\beta_1}{cos^3\beta_m}$$
$$with \quad C_{Da} = 0.02\,\frac{s}{h} \quad and \quad C_{Ds} = 0.018\left(\frac{2\,(tan\beta_1 - tan\beta_2)\,cos\beta_m}{\sigma}\right)^2 \tag{3.2}$$

  Where C_{Da} and C_{Ds} are the annulus and secondary drag coefficients, h is the blade height and β_m is the mean relative flow angle.

- Clearance losses, accounted for with Lakshiminarayana

$$\Delta\eta = \frac{0.07\,\frac{\epsilon}{h}\psi}{cos\alpha_m}\left(1 + 10\sqrt{\frac{\phi\,\frac{\epsilon}{c}}{\psi\,cos\alpha_m}}\right) \tag{3.3}$$

  where ϵ is the tip gap, ψ is the work coefficient, ϕ is the flow coefficient and α_m is the mean absolute flow angle.

- shock losses, which represent the most important source in transonic fans but are extremely case dependant and not possible to be modeled a priori at the time being.

Since the significant blade span and sigma and the reduced flow deflection in the fan the endwall and secondary losses have been discarded in the simulation. This is in line with common practice in BFM simulation to simplify the viscous term in the equations (see section 2.1.1). In the same way the clearance losses have been taken out opting for a no-tip blade representation. This decision has been driven by to the current SU2 issue with BFM of backflow in the tip region. This way the study has been limited to the profile losses modeled by Thollet and the shock losses.

3.1.2. Parablade

Parablade [1] is a turbomachinery blades generation software used for high-fidelity parametric representation of the blade. It provides smooth blade geometries at a limited computational cost and allows the user to impose geometrical constraints from mechanical or aerodynamic requirements. These features makes the program a useful tool for shape optimization purposes.

The program uses Non-Uniform Rational Basis Spline (NURBS), a generalization of Brezier curves and B-splines, in order to represent the geometry. A NURB curve is a parametric curve defined as:

$$\boldsymbol{C}(u) = \frac{\sum_{i=0}^{n} N_{i,p}(u)\, w_i\, \boldsymbol{P_i}}{\sum_{i=0}^{n} N_{i,p}(u)\, w_i}, \quad with\ 0 \leq u \leq 1 \tag{3.4}$$

where p is the curve degree, $\boldsymbol{P_i}$ and w_i are the coordinates and the weight of the control points and $N_{i,p}$ are the B-splines basis function along the coordinate u. In a similar way

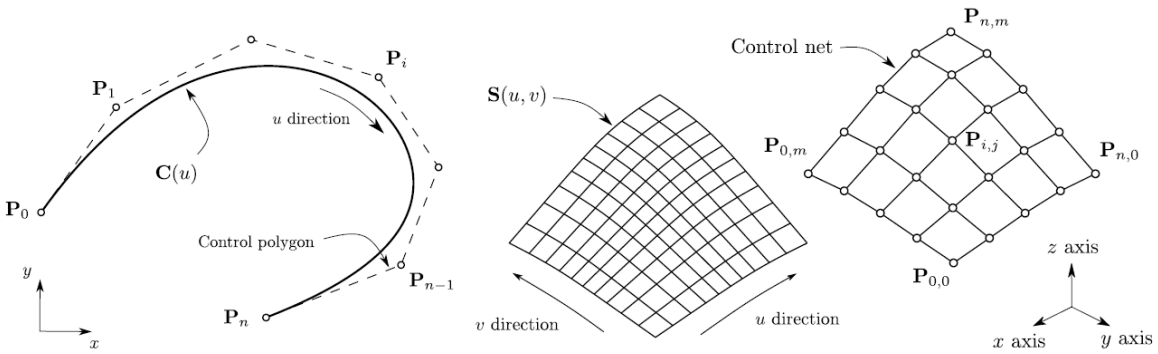

(a) NURBS curve construction **(b)** NURBS surface construction

Figure 3.2: Construction of a NURBS curve (left) and surface (right) [1].

NURBS surfaces can be defined. They show the useful characteristic of interpolating the end points and being tangent to the last segment, while at the same time it is possible to apply affine transformation to the whole curve by working directly on the control points.

The program generates the blade geometry starting from the 2D section creation according to the input variables reported in table 3.1

Firstly the camber line is created using a cubic B-spline from 4 control points using stagger angle, metal angles and axial chord (see figure 3.3). Afterwards the upper and lower thickness distribution are assigned along a user defined number of control points and the upper and lower sides are build using a fourth order B-spline. This is able to satisfy up to a continuous curvature rate of change in order to minimize the occurrence of flow detachment. Then the 3D extrusion of the blade is performed recurring to the spanwise variation of design variables and to the blade shape in meridional channel. The former is defined through a third degree B-spline with an arbitrary number of control points related to the shape complexity, while the latter is represented by the four limit curves (LE, TE, hub and shroud). Finally the flow domain boundary are modeled by extending the the various spanwise section camber lines in the different directions.

From the input parameters two main output files are produced: a .crv file containing the points coordinates necessary for reproducing geometry in other software and the .drg file with the parameters requested by SU2 to generate the force field for BFM computations. In addition to the blade geometry, in the BFM case, the program also computes the surface normals and the blockage factor distribution. The computational time required to recreate the blade is limited to a couple of seconds.

As anticipated another useful function of the program is the *MatchBlade* feature, a script able to reproduce an existing geometry from a set of points extracted from a mesh or a

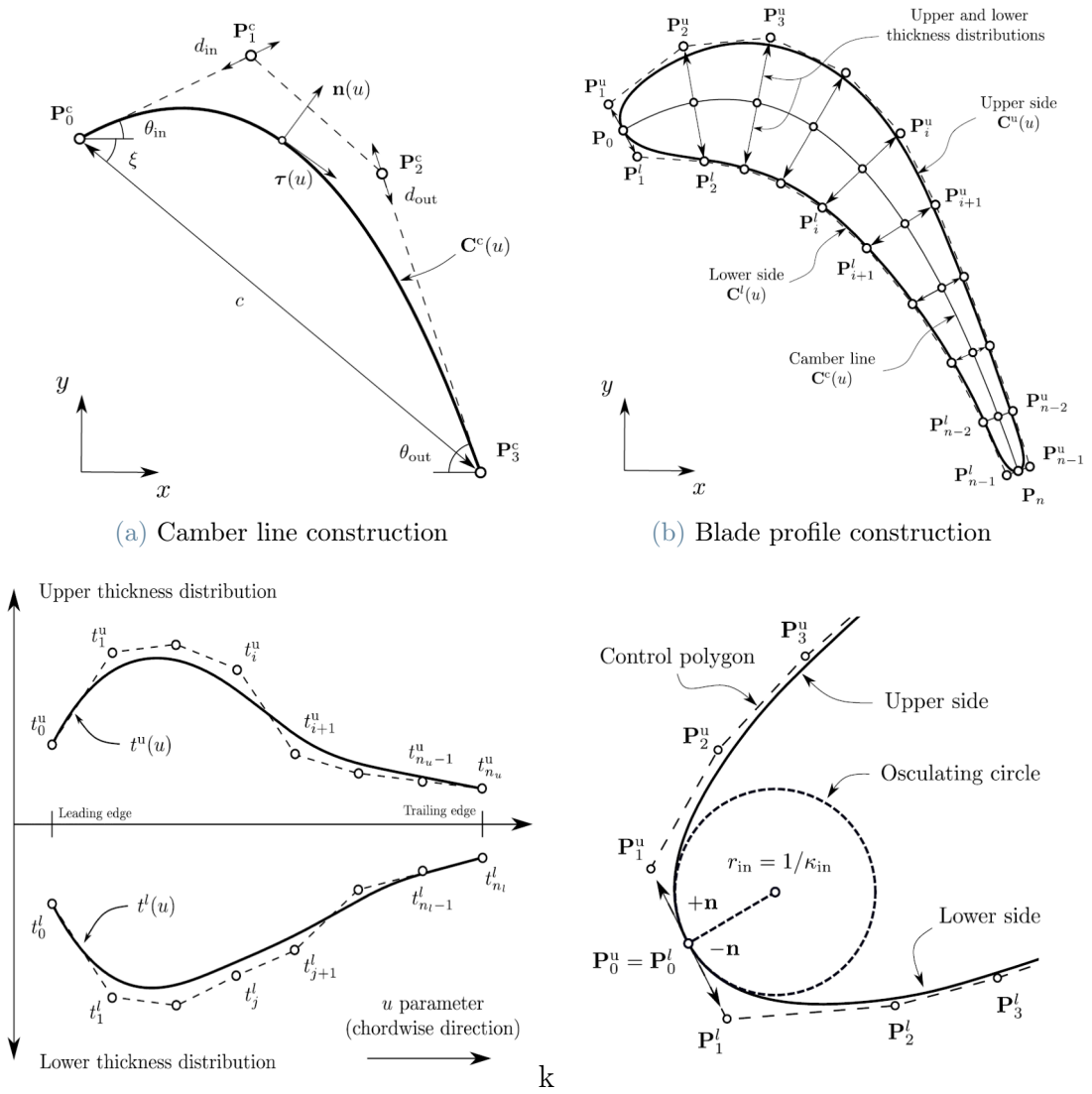

(a) Camber line construction (b) Blade profile construction

(c) Thickness distribution (d) Leading edge construction

Figure 3.3: The 2D blade section is built with an precisely tunable process [1].

Table 3.1: Three dimensional Parablade design variables.

Design variable	Symbol
Leading edge control points	x_1, z_1
Hub edge control points	x_2, z_2
Trailing edge control points	x_3, z_3
Shroud edge control points	x_4, z_4
Leading edge abscissa	y_{in}
Stagger angle	ϵ
Inlet and outlet metal angles	$\theta_{in}, \theta_{out}$
Inlet and outlet tangent proportions	d_{in}, d_{out}
Inlet and outlet curvature radii	r_{in}, r_{out}
Upper and lower thickness distribution	t_{up}, t_{low}

CAD model into parametric terms as in table 3.1. The process is divided into 3 steps:

- preliminary guess, in which the user tries to reproduce the blade at hand;
- point projection phase, where the distance between the prescribed points and the guess is minimized over the 2D parametric directions;
- geometry update phase, in which another geometry deviation minimization problem is performed for the design variables.

3.2. CFD simulations

This block constitutes the root of the experiment and it is itself subdivided into two conceptually different parts. Firstly a reference simulation is performed to obtain accurate flow data to compare with the BFM. This simulation must be initialized manually due to the need to mesh the physical blade. The second part is an iterative process made of the automated BFM mesh, the SU2 simulation and the data postprocess.

3.2.1. ANSYS Turbogrid

Turbogrid (block 8) is mesh generation software able to create structured meshes of complex blades and is commonly used in turbomachinery analysis. It was used to convert the curve files from parablade into a geometry that could be meshed.

Since this tool has been used to perform the high-fidelity analysis it has been deemed necessary to impose a very fine mesh, especially near the boundary walls. Moreover the presence of strong instabilities at the channel outlet as described in section 4.2 for the

fan required to extend the outlet distance from the TE in the files. These two reasons required a high number of nodes in order to mesh the blade, inducing this way a more significant simulation time.

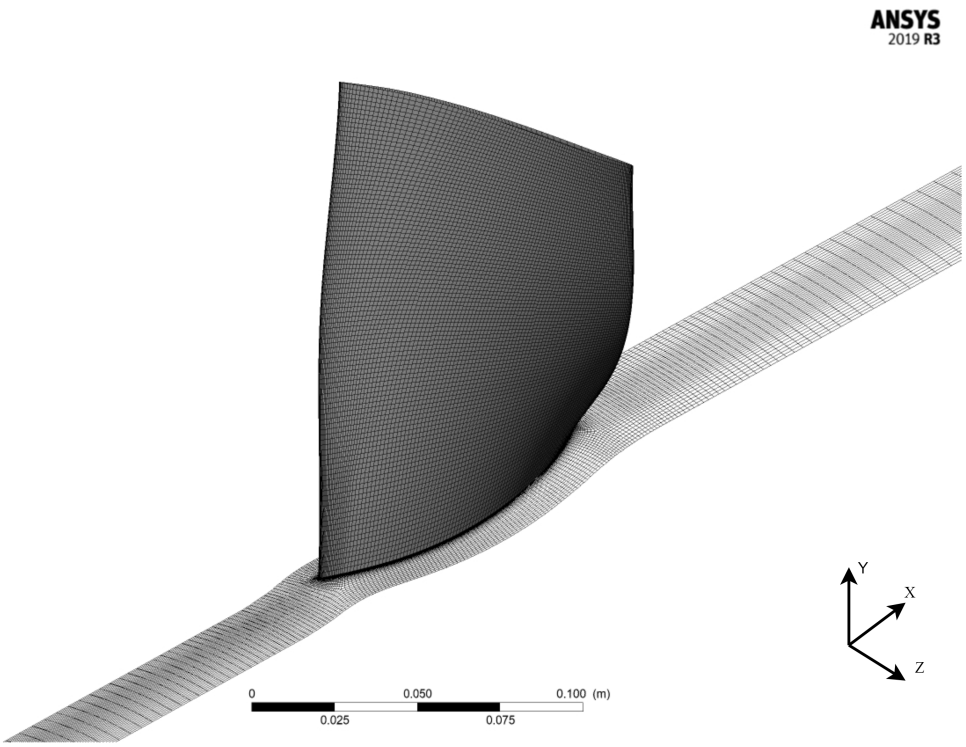

Figure 3.4: Isometric view of the blade mesh of the NASA rotor 67 geometry generated by TurboGrid.

3.2.2. ANSYS CFX

ANSYS CFX-Pre, CFX-Solver and CFD-Post (respectively block 9, 10 and 11 in Fig.3.1) are three connected modules of the ANSYS commercial code [2]. They are well suited for turbomachinery simulations and compressible fluids in general. The program has been used extensively for fan performance assessments and the literature about the chosen NASA Rotor67 is abundant.

In order to represent a fan it is advisable, to the writer's knowledge, to use as BC the inlet total quantities and the outlet corrected mass flow, avoiding this way the instabilities at the outlet caused by an higher back pressure. These issues are especially strong near the stall condition of the machine.

$$\begin{aligned} \dot{m} &= \dot{m}_{corr} \frac{\delta}{\sqrt{\theta}} \\ with \quad \delta &= \frac{P_t}{P_{ref}}, \quad \theta = \frac{T_t}{T_{ref}} \end{aligned} \tag{3.5}$$

Where P_{ref} and T_{ref} can be taken as inlet atmospheric values and P_{tot} and T_{tot} as outlet total ones.

A CFX simulation has been performed on a single machine, at the beginning of the process, in order to obtain reliable data to validate BFM results with. For this computation an highly refined mesh with full BL resolution was selected (see section 4.1). Such choice allows to avoid the need for a grid convergence study on CFX.

Subsequently, in order to carry out the sensitivity analysis reported in chapter 5, several more runs were required. These involved physical blade remesh, which can affect the results for large deformations. Luckily the blade deformation induced by the small parameters change is small, thus no mesh influence are considered reference chapter. Since this investigation needed significant time to be performed on a single machine, it has been deemed more effective not to automatize the process, but rather performing the necessary simulations on high performance computing (HPC) clusters at disposal to TU Delft researchers.

3.2.3. ICEM

ANSYS ICEM is an advanced meshing software with accurate diagnostic capabilities. It was selected as the main tool of the simulation loop because it produces highly tunable structured mesh for turbomachinery blades.

The main advantage of the BFM formulation is the possibility to generate a domain mesh without accounting for the physical blade presence, allowing this way to produce a structured mesh with great performance in terms of quality, angles and skewness. Such efficient mesh will grant fast CFD simulations convergence.

The iterative process was written to produce both a full-annulus (Fig. 3.6) mesh or a periodic one (Fig. 3.5), such that the results can be compared. For the periodic domain a 3 degrees wedge has been created, such that in the following grid convergence study (see 4.2.4) the elements size are equal to the FA ones. For this study a different number of nodes in axial, radial and tangential directions has been examined n order to underline the influence of the discretization in each direction. In ICEM this has been found to significantly affect the time required to perform the mesh generation, which rise with the

number of nodes as reported in table 3.2:

Table 3.2: Time required for meshing the domain in ICEM. The number of nodes is reported in terms of $N_{ax} \times N_{rad} \times N_{tan}$.

Number of nodes	**Time** $[s]$
60x40x1	2.81
60x40x2	2.97
60x40x3	3.67
60x40x120	17
60x40x240	32.58
60x40x360	49.09

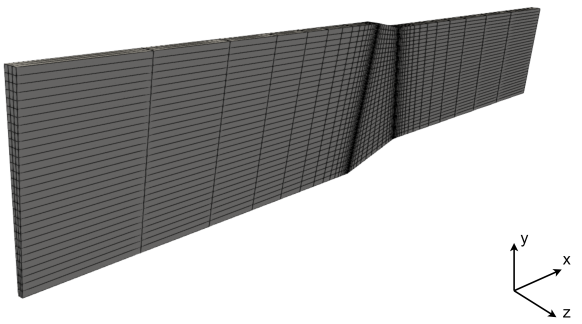

Figure 3.5: The periodic mesh allows to use a limited number of tangential nodes to represent a single channel passage.

3.2.4. SU2

Even though BFM has already been implemented in several different commercial CFD software as ANSYS CFX [20] and Fine/Turbo [13], other authors deemed more useful to implement the model on SU2 as reported in [4] and [14]. The main advantage of such choice is that SU2 is an open source software and the code can be modified according to the necessity. This program aims at solving partial differential equations (PDE) and their constrained optimization for unstructured mesh. It is specifically focused on RANS problems for compressible, turbulent flows, thus it fits well for simulating turbomachinery related problems. It consists in a standard compiled C++ and Python scripts ones that are divided into separated blocks for different functions such as CFD simulations, mesh analysis, gradients computation and others. The principal one is the SU2-CFD module,

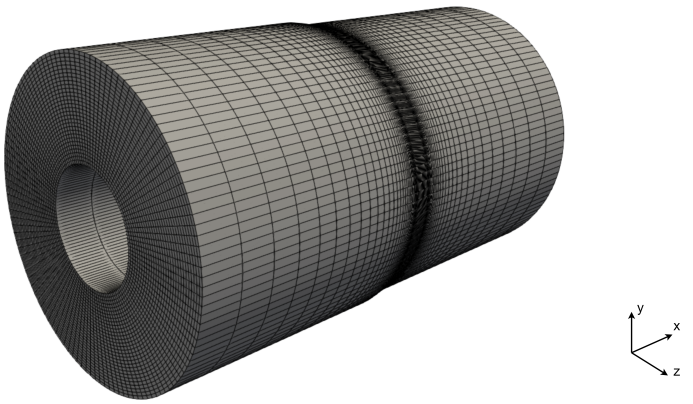

Figure 3.6: A full-annulus mesh has been created in order to evaluate possible non axisymmetric behaviours.

used to solve Euler, Navier-Stokes or RANS problems. The main characteristic of the code is the C++ object oriented formulation that enables to connect the different blocks using the same class design methodology throughout all of them.

The BFM formulation has been implemented on SU2 as described in [4] and [14] for both Hall's and Thollet's models. Since the model verification has already been performed in the cited works it has been deemed not necessary to do it again in the current thesis. SU2 BFM code takes as inputs a configuration file, the mesh in .CGNS format and the file previously produced by Parablade containing the extracted blockage factors and normal distributions over the blade surface. The program then performs a linear interpolation between these points and the structured mesh, inserting inside body-force affected region the source terms (fig. 3.7). This mechanism is the base of the BFM concept, allowing to neglect the physical blade presence typical of other commonly used methods.

SU2 is an always improving and developing code and which implies some differences between the versions. The version that has been used in this thesis is the 7.2.1 "Blackbird" one. It must be noted that there are some limitations with the current iteration of the code:

- the code is mainly formulated for Linux environment with a Windows limited support. This causes issues in compiling the code under Windows system (necessary for the automated workflow of this thesis) and it required the use of Windows Subsystem for Linux (WSL) software architecture [17] ;
- the outlet BC is currently limited only to static pressure for subsonic exit. This conditions causes instabilities at the exit in case of compressors due to back pressure

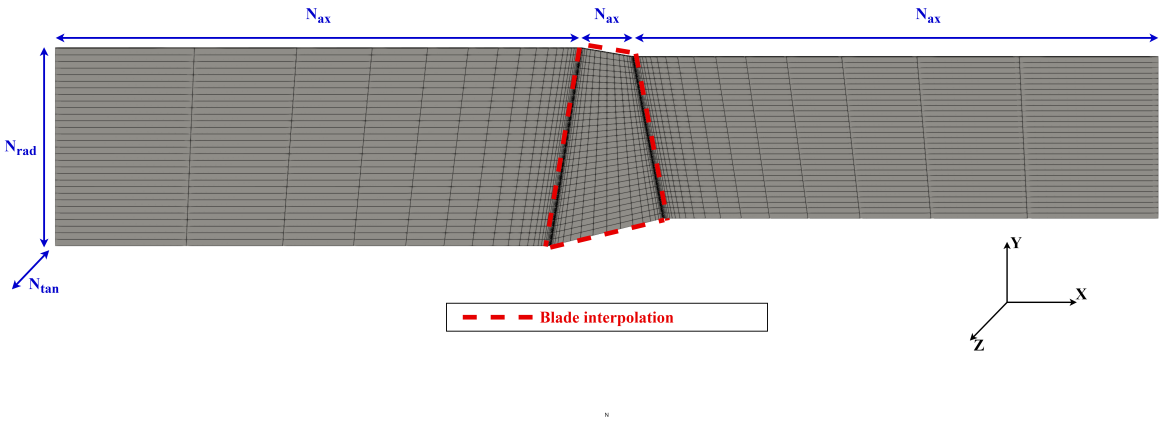

Figure 3.7: After the simple domain mesh has been created without accounting for the blade, this can be modeled with BFM and interpolated over the relative zone of influence.

and requires to elongate the domain;

- periodic boundary conditions are currently not robustly stable (see [22]) and induces issues as reported in 4.2.3.

3.2.5. Paraview

For data extraction and post-processing Paraview has been used. Paraview is an open source software for data analysis and visualization which presents the main advantage of being written in Python language. This makes the program inclusion in the iterative design cycle efficient. Moreover the wide range of program filters enable the user to tune the analysis at will, making this program one of the most used ones in CFD post-processing field.

For the final visualization of the flow field plots the Turbulucid package [24] has been used. This python written code allows for flexible graphical representation of the flow field from Paraview .vtk files to standard plots.

3.3. Sensitivity analysis and optimization

This section aims to evaluate the sensibility of the objective function, which in this work has been chosen to be the rotor isentropic efficiency, to design variables. Eventually an optimization run can be performed in order to produce an optimal geometry in BFM.

As reported in section 2.2 the finite differences method has been selected to carry out the sensitivity analysis.

Even though SU2 already presents the capability for gradient based and adjoint optimization these functionalities have not successfully been implemented for BFM simulations yet. The writer has then opted to adopt in the design cycle the program Dakota.

3.3.1. Dakota

Dakota [3] is a C++ written program used for optimization, sensitivity analysis and unsteady quantification. It provides a rapid and systematic way to improve the design under study and to understand the effect of each parameter thanks to a plethora of different iterative methods and algorithms it offers. The different functionalities are grouped under distinct block, the 3 most import ones are:

- Parameter study, to study the effect of parameters change over the whole simulation enabling to evaluate its smoothness, robustness and non linearity. The most used methods of this category are centered study, one-at-a-time and joint grid variation;
- Design of experiments, to generate a good coverage of the design variables space and study their influence over the global sensitivity of the objective. The most used method of this kind is the Latin Hypercube;
- Optimization, the block that tries to minimize the cost or maximize the performance of the objective at hand while enabling the user to specify any kind of constraint over the parameters. The algorithms used provides gradient-based methods, gradient free and global optimization. It is even possible to design for multi-objectives trade-off optimization.

In this thesis the method used is a simple local centered parameters study. This option was selected because of the great number of design variables characterizing the problem and connected computational cost. In order to evaluate the sensitivity analysis a basic forward finite differences approach has been adopted.

Another fundamental advantage of Dakota is the possibility to set up a single interface between the program and an outside simulation, enabling this way to change the iterative method and the algorithms used by modifying only the initial Dakota input file. Such coupling is generally referred as "Black Box" approach because the program has no information about what is occurring inside the simulation. More intrusive formulations are possible, but they require a deep modification of the source code, thus being extremely time consuming to implement.

4 | NASA Rotor67 testcase

In this chapter, the numerical settings for the chosen testcase are presented and the simulations results are reported, comparing the shortcomings encountered in SU2 and the flow pattern discrepancies.

In order to effectively apply BFM in the design process of a fan stage, first of all it must be verified whether or not it produces reasonable results for our transonic case. As such the widely tested NASA Rotor67 (fig.4.1) geometry was selected as a test case.

N_{blades}	22
RPM	16043
Tip speed	$429\,[m\,s^{-1}]$
Tip $M_{rel,in}$	1.38
Design $\dot{m}$	$33.25\,[kg\,s^{-1}]$
Choke $\dot{m}$	$34.96\,[kg\,s^{-1}]$
Π	1.63
Tip clearance	$1.016e^{-3}\,[m]$
Average aspect ratio	1.56
Tip solidity	1.29
Hub solidity	3.11
Tip r_{LE}	$0.257\,[m]$
Tip r_{TE}	$0.2425\,[m]$
Inlet r_{hub}/r_{tip}	0.375
Outlet r_{hub}/r_{tip}	0.478

Table 4.1: Rotor67 design point [21].

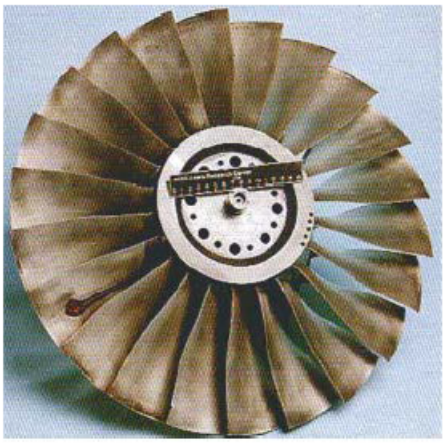

Figure 4.1: Rotor67 geometry [21].

NASA rotor 67 is the first row of a two stage transonic axial fan. It is composed of 22 blades with an aspect ratio of 1.56 based on average span/root axial chord. This machine has been chosen as a reference due to the exhaustive literature at disposal [21] as well as several design shape optimization studies. The machine has been studied only at its design point. The main characteristics of the fan are here reported in table 4.1.

The first thing that has been done is the blade match using Parablade (as per Fig.3.1 block 1), showing good agreement between the existing blade and the parametrized one as can be seen from Fig. 4.2.

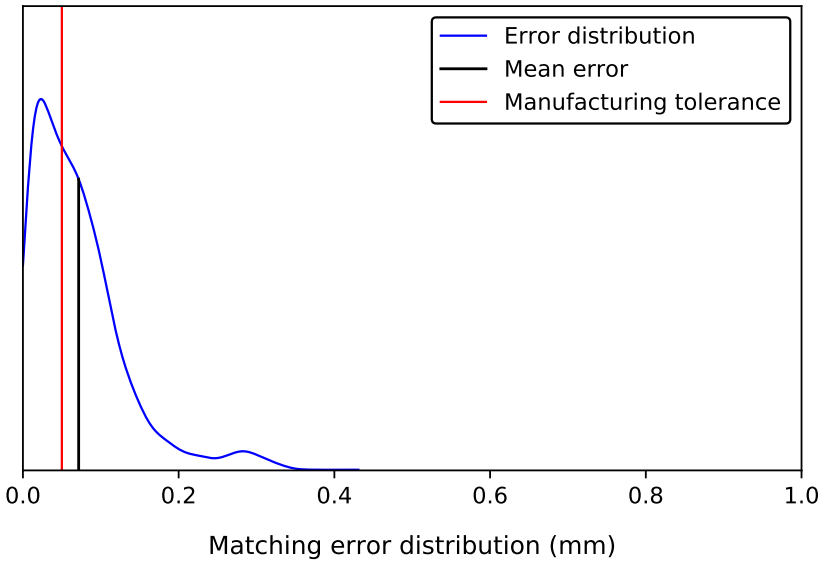

Figure 4.2: Error distribution computed as RMS difference between input blade coordinates and Parablade parametrized ones. The mean error is close to the typical manufacturing tolerance.

It must be noted that some modification to the original Parablade exit files are required to proceed with the simulations. One problem arises from the blade tip gap which, in the current BFM implementation on SU2, induces back flow phenomena in that region. Until future tip gap correction factor is inserted, this opening has then been eliminated from the produced geometry. Moreover the .crv files resulting from Parablade presents a short inlet and outlet section. Since they are not feasible for the simulation stability their distance must be increased. These boundaries are then placed at 2.5 times the blade span from the LE and TE.

4.1. CFX simulation

As a reference for assessing BFM reliability a high-fidelity cfd simulation has been performed. Here the simulation settings are reported as well as the comparison with experimental data.

4.1.1. CFX mesh

To create the mesh used for the simulation Turbogrid has been used. In this program the inlet, outlet and mid passage blocks are meshed to produce the domain for CFD computation. The middle section represent the most critical part due to the presence of the blade and its complex shape. An high number of spanwise layers has been used to represent it as indicated in table 4.2. This allows to capture the strongly twisted rotor blade shape. The necessity to mesh a long channel required a significant of nodes for the two external sections in order to avoid too large expansion ratio or large end channel elements which in turns would cause issues in solving the flow equations at the outlet section.

Table 4.2: Turbogrid mesh settings.

Setting	Type/Value
Topology	ATM Optimized
Layers mode	Manual-Uniform
Layers number	10
BL method	1^{st} Element Offset
Offset Y+	1
Expansion Rate	1.2
Re number	$2.2e^6$
Spanwise method	Uniform
Spanwise elements	100
Inlet elements	70
Outlet elements	70
Total elements	2192200

In order to fully address the turbulence induced by the blade it has been decided to place the first cell center in the viscous sublayer region. This way no wall model is used to represent the BL influence but it is fully resolved. A unitary $y+$ value has then been adopted, using a Re number of $2.2e^6$ obtained from:

$$Re = \frac{\rho W c}{\mu} \tag{4.1}$$

where W is the relative velocity at the blade LE and c is the blade mean chord.

4.1.2. CFX settings

Since the need to obtain reliable results for the comparison in a reasonable time a RANS simulation has been performed in CFX. Turbulence has been modeled using SST closure

method. This was chosen also to better represent the fan problem, since k-epsilon model tends to be unstable in case of pressure rising though the channel.

Residuals and total imbalances have been considered as convergence parameters of merit. These variables showed that the simulation fully converged despite a small residual oscillatory behaviour. This characteristic is probably linked to the intrinsic problem unsteadiness, which could not be completely resolved using RANS.

A first CFX simulation has been carried out on a single machine, so that a computational cost comparison can then be established with BFM computations. On the single machine the time required is approximately 7.5 hours. The following simulations used to perform the sensitivity analysis (see chapter 5) during the work were performed on the HPC to save time. For these runs the blade have been remeshed keeping the same parameters reported in table 4.2 but changing the geometry according to the updated Parablade output file.

Table 4.3: CFX problem definition.

Setting	Type/Value
Turbulence model	SST
Fluid	Air ideal gas
Analysis type	Steady state
Reference pressure	0 $[Pa]$
Heat transfer	Total energy

Table 4.4: CFX solver controls.

Setting	Type/Value
Advection scheme	High resolution
Turbulece numerics	High resolution
Max iterations	750
Timescale control	Auto
Timescale option	Conservative
Convergence	RMS
Residual target	$1e^{-6}$

Table 4.5: CFX boundary conditions.

Boundary	Boundary condition
Inlet	$P_t = 101325\ [Pa]$ $T_t = 288.2\ [K]$
Hub wall	Free-slip
Shroud wall	Free-slip
Blade	No-slip
Outlet	$\dot{m}_{corr} = 22\ [kg\ s^{-1}]$

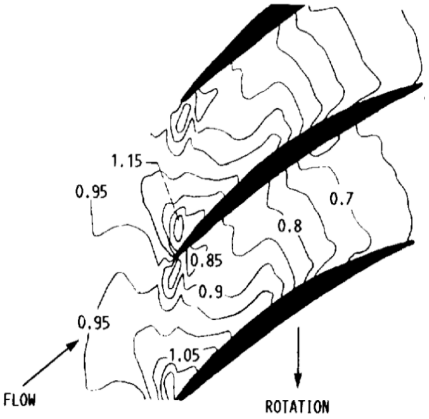

(a) Experimental at 30% span

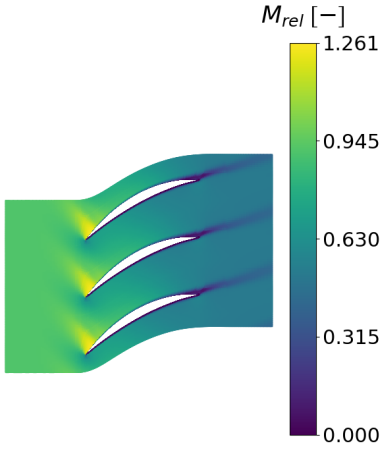

(b) CFX at 30% span

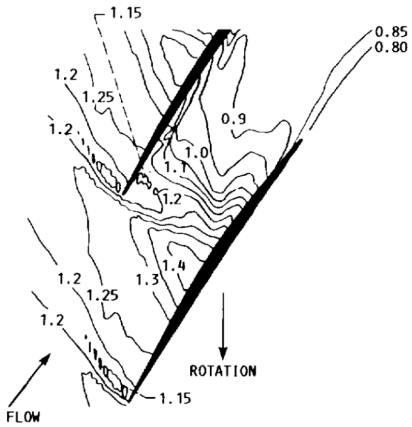

(c) Experimental at 70% span

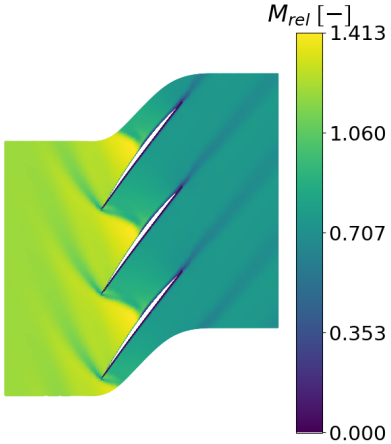

(d) CFX at 70% span

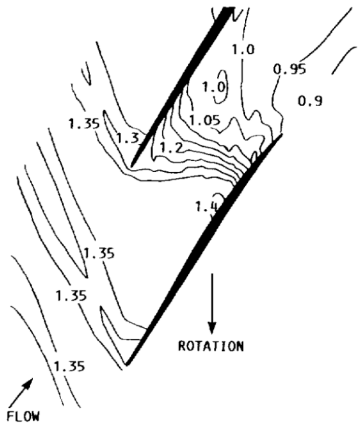

(e) Experimental at 90% span

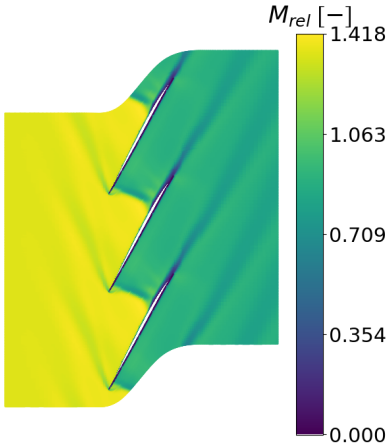

(f) CFX at 90% span

Figure 4.3: Comparison between rotor67 experimental results [21] and CFX. The blade-to-blade plane views at different spanwise sections show matching supersonic behaviour between the data.

4.1.3. CFX results validation

From the results obtained it can be seen how this simulation closely matches the global experimental data as reported in table 4.6. The small variation in efficiency and mass flow can be partially attributed to the absent blade tip gap and to the neglected viscous effect at the walls. Nevertheless these results constitute a useful comparison to study the BFM case.

Table 4.6: CFX results.

Performance	Experimental value	CFX value	Error
$\dot{m}$	$33.25\,[kg\ s^{-1}]$	$34.20\,[kg\ s^{-1}]$	2.85%
η	93%	93.06%	0.07%
Π	1.63	1.68	3.08%

The blade-to-blade section plane has been plotted 4.3 in order to show the close match between experimental and computed flow solutions. As it can be seen from the comparison, using blade geometry obtained from Parablade, CFX is able to reproduce the same supersonic structures registered in the experiments.

4.2. SU2

In this section the ICEM mesh and SU2 simulation settings and some of the software limitations are presented. Afterwards a grid convergence study is performed with the aim to minimize numerical errors due to the mesh refinement. Lastly the BFM and CFX results are compared

4.2.1. SU2 mesh

SU2 is currently able to process only .CGNS file or .SU2 file. A document of the first kind is produced by ICEM as described in section 3.2.3. The parameters used to generate the mesh are:

- the number of nodes in axial, radial and tangential directions;
- the inlet, outlet, LE and TE expansion coefficients, representing the rate of change for the cell size near the respective location;
- the first cell center offset;
- the wedge tangential degrees.

Different nodes numbers have been tested as reported in section 4.2.4. An advantage of specifying such parameter in each direction is that it allows to study the grid influence over the final flow results. This helps to understand what level of refinement is needed to obtain grid independent results. The writer's objective is to obtain accurate results with the minimum number of elements, such that the computational time is the lowest possible. The expansion coefficient has been fixed to 1.2 in each region, as this value has been found to discretize well the blade section while granting smooth cell growth in the outer ones. Regarding the first cell offset, it has been set to $5e^{-4}[m]$, a much larger value than the one resulting from the CFX settings. In BFM simulation this parameter is not necessary for BL modelization as in CFX, but rather it is used to fully capture the critical blade edges influence over the flow turning. Lastly the wedge used for the simulation is a 3 degree one in case of periodic domain and a 360 one for full-annulus. All the mesh design values presented are given by the user in the initial program input file (see appendix A) and a suitable mesh is produced.

The important distinction in terms of wedge angle between the problems studied must be further stressed: the methods proposed by Hall and Thollet have, in fact, the main scope of capturing non-uniformities in circumferential flow pattern due to non uniform inlet flow such in the case of BLI. This is achievable by using a full-annulus domain. On the other hand, the need to evaluate BFM for design purposes, led to the study of a uniform axisymmetric flow inlet in this thesis. For such flow the complete annulus reproduction is, in theory, not necessary, but a single passage representation can be used resorting to periodic boundary conditions. Due to BFM nature, which represents the blades effect as an averaged circumferential force field, it is possible in theory to represent even a thin wedge with a single tangential node. Clearly this option would massively decrease the number of grid elements and the associated computational time, but it should be verified before its design application. For this thesis both the full-annulus and a 3 degrees wedge have been studied so that comparison can be made in terms of accuracy and time requirements (see section 3.2.3).

4.2.2. SU2 settings

Here the settings for SU2 BFM simulation are reported. Noticeably, it is not currently possible to specify an outlet condition for mass flow rate as done in CFX. This limits the boundary conditions choice to the use of pressure based relations at both ends. Such initialization is not strongly stable for modeling compressor, but due to time constraints the writer was not able to implement a different subsonic BC on SU2. In order to obtain better agreement with high-fidelity CFD computations the outlet static pressure value

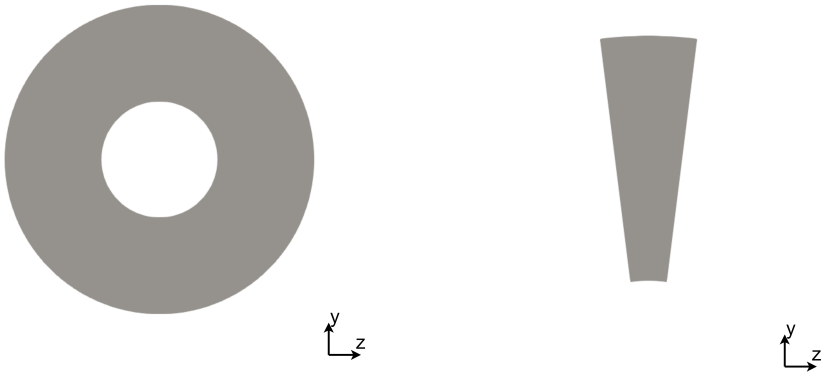

(a) Full-annulus domain (b) Periodic domain

Figure 4.4: BFM different domain geometries cross-sections.

can be obtained directly from CFX initial run.

As reported in table 4.7 the condition to impose free slip wall in SU2 at the hub and shroud is the symmetry wall one.

Table 4.7: SU2 boundary conditions for rotor67.

Boundary	Boundary condition
Inlet	$P_t = 101325\ [Pa]$ $T_t = 288.15\ [K]$
Outlet	$P_s = 126644\ [Pa]$
Blade wall	No-slip wall
Hub wall	Symmetry
Shroud wall	Symmetry
Side walls [1]	Periodic

[1] This BC is not present in the full-annulus case

Table 4.8: SU2 solver settings for rotor67.

Setting	Type	Value(s)
Solver	Euler	
BFM formulation	Hall/Thollet	Force rotation = 16043 $[RPM]$ Axis = $[1, 0, 0]$
Turbulence model	None	
Fluid model	Ideal gas	R = 287 $J\ [kg^{-1}K^{-1}]$ $\gamma = 1.4$
Viscosity model	Constant	$\mu = 1.3764E-5\ [kg\,m^{-1}\,s^{-1}]$ $T_{ref} = 273.15\ [K]$
Conductivity model	Constant Prandtl	$C_{KT} = 0.0257$
Spatial gradient model	Green-Gauss	
Linear solver	FGMRES	Error = $1e^{-4}$ Iter=5
Flow numerical method	Lax-Friedrichs	Sensor coefficient = 0.15 Entropy fix coefficient = 0.3
CFL number	Adaptive	CFL = 100 min = 1.0 max = 1000
Convergence criteria	Residual	$RMS < 1e^{-12}$

The CFL adaptive condition is imposed because of the unstable convergence connected to the low grid refinement. It has been noted that increasing the number of nodes during the experiments permits to use a fixed CFL number higher than 250. Such high value slightly reduces the computational time of the simulation.

A relevant restriction encountered during the work is the impossibility to converge for flow numerical methods with order higher than one. The writer was able to make the BFM simulation converge only using the highly dissipative Lax-Friedrich scheme. This limit is in contrast with what has been shown in [4], where the fourth order accurate JST advection scheme was used to simulate a turbine with BFM. Such issue can be addressed to the lower problem stability found in axial fan with respect to turbines, due to negative pressure gradients, and to the more complicated shape of the twisted blade. Future work in this sense can be performed to obtain more accurate simulations.

4.2.3. SU2 shortcomings

Some issues have been found in the current SU2 version by monitoring simulation results:

- the subsonic outlet BC restriction to static pressure limits the achievable stability in that region. By monitoring the residuals across the control volume it is in fact possible to observe how a strong inequality region develops at the exit. In particular for short channel configuration, the solver tends to converge until an inverse trend develops near the exit hub. This region does not allow the solver to fully converge and induces a backflow phenomena;
- the periodic boundary conditions are currently lacking in terms of stability. As can be seen from Fig.4.5 there is a mismatch between residuals on the left and right sides. While the left side residuals are null for the whole simulation, on the right one an unstable behaviour is registered. This mismatch is believed to be caused by a error in the Jacobian implementation in the code as reported on the development page [22]. Even if this does not cause a major discrepancy in the final results obtained by means of periodic boundary conditions, it is yet the cause of a delayed convergence;
- the solver is prone to high mass flow imbalance as shown in Fig.4.7.

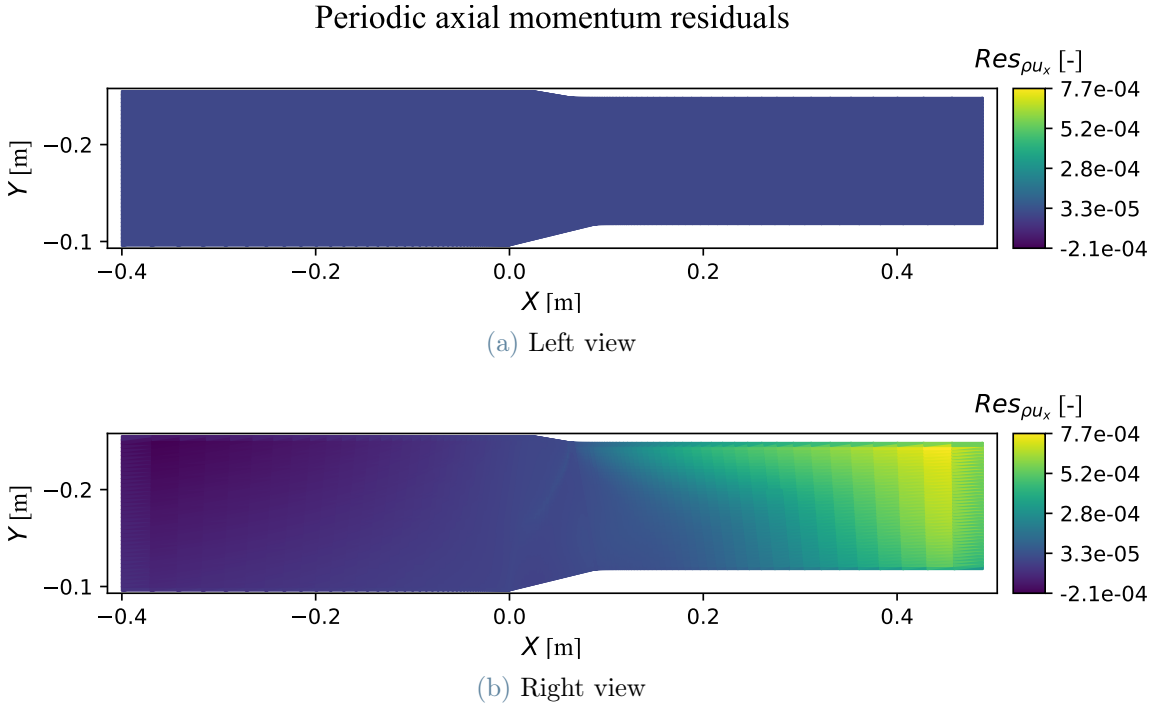

(a) Left view

(b) Right view

Figure 4.5: Periodic residual discrepancy is found in SU2. The homogeneous left boundary residuals remain zero while they vary on the non-homogeneous right side.

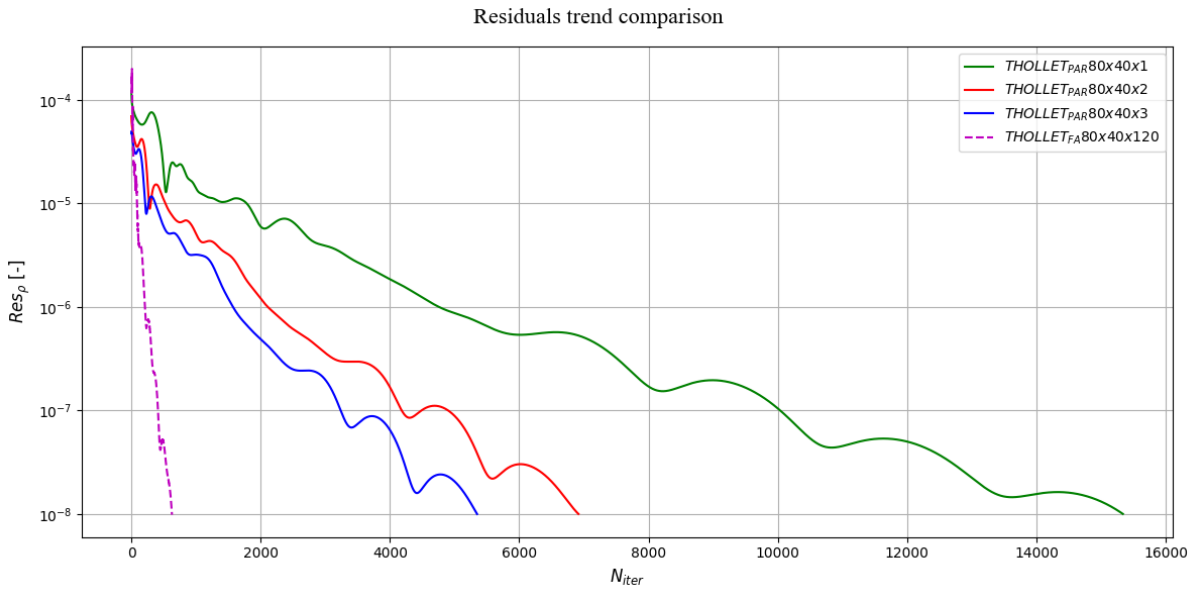

Figure 4.6: Number of iterations required by different boundary conditions and tangential discretization.

The reduced periodic stability effect can be furthermore observed comparing the global residual convergence trend for different number of tangential nodes. As can be seen from figure 4.6 in order to simulate the same problem with 1, 2 or 3 tangential nodes the required number of iteration is strongly affected. On top of that there is an even greater difference with respect to the full-annulus simulation. While full-annulus simulations take less than 600 iterations to convergence, in the periodic one the required number is at least one order of magnitude greater. This effect in theory should not be present and it has been recognized as the major drawback to time saving connected to periodic simulation as reported in chapter 4.3.4

The mass flow imbalance is a direct consequence of the discretization errors. It is, in fact, an intrinsic CFD spurious phenomena that does not make physical sense as reported in [7]. This defect is limited in the CFX fine grid simulations to $\Delta m = 0.001\%$ while in SU2 is generally more pronounced. As can be seen from Fig. 4.7 in the case at hand this behaviour is further stressed by the BFM and reaches different percentage points in some cases. From what can be seen a global mass imbalance near 1% can be found between inlet and outlet of the channel (as reported in table 4.9), while the biggest delta is located in the blade region. Even if this has to be expected in Thollet's formulation due to the continuity source term, it should not be present in Hall's computations. Nonetheless the region appears then to be critical for the solver to handle.

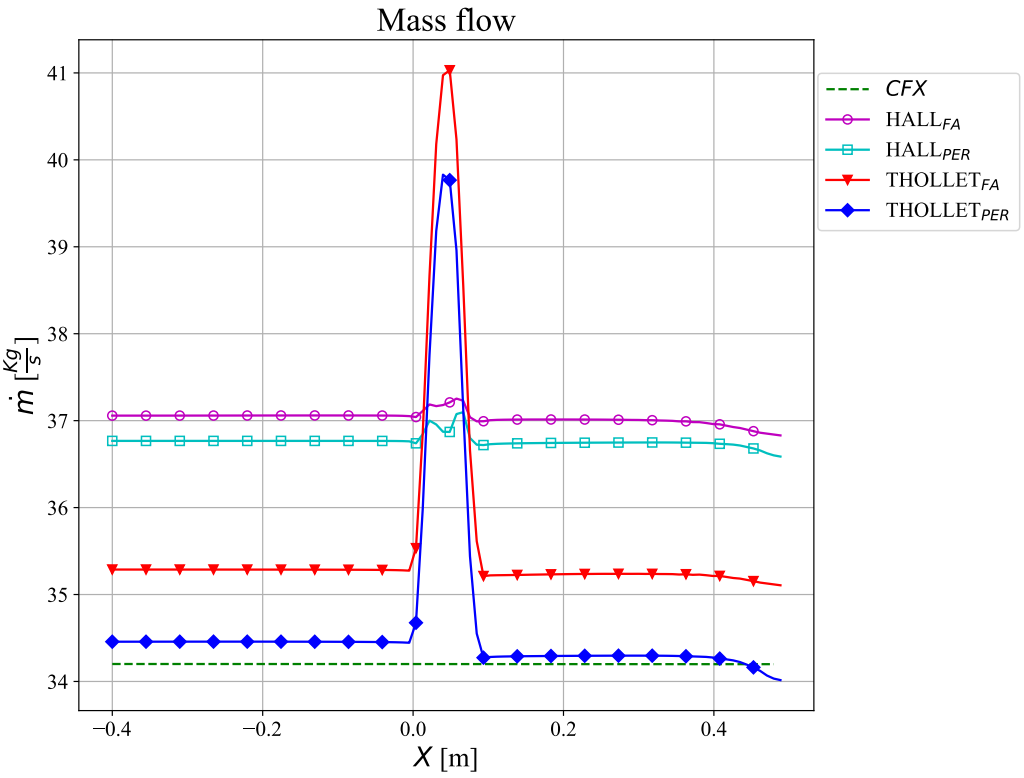

Figure 4.7: Mass residuals show the imbalance across the stage.

Table 4.9: SU2 mass imbalance percentage.

Model	Global $\Delta\dot{m}$	Blade $\Delta\dot{m}$
$\boldsymbol{HALL_{PER}}$	0.49%	0.90%
$\boldsymbol{HALL_{FA}}$	0.56%	0.55%
$\boldsymbol{THOLLET_{PER}}$	1.28%	15.59%
$\boldsymbol{THOLLET_{FA}}$	0.51%	16.28%

4.2.4. Grid convergence study

An effective CFD study requires an accurate grid convergence study in order to validate the results obtained from the simulation. This procedure grants that the produced results are independent from the grid resolution. If no such check is performed, the discretization errors may be severely underestimated and the results may strongly depend from the adopted mesh. This would make impossible to assess the results validity and the influence of different design variables.

The way this verification is carried out is to increase progressively the mesh refinemet, so that the truncation and discretization errors, connected with the numerical problem, decrease. Hence an asymptotic region should be reached and fan estimation of the error connected to the chosen grid resolution could be obtained. No grid convergence study has been performed in CFX, but rather a strongly refined grid has been selected from the beginning in order to obtain reliable results.

Some meaningful results variables must be selected as parameters of merit to perform this verification . The parameters taken into account for this work are the mass flow and the total-to-total isentropic efficiency. The first represents a good indication of the blockage factor implementation in Thollet's formulation, while the latter represents the global blade shape influence over the machine performance, even if it does not consider the local effects in the channel.

The method used to perform the study in this section follows the ASME directives reported in [5] and [18]. Detailed information on the method and its application on this work can be found in Appendix B. Three grid resolution for each direction have been selected in order to study the grid convergence for each one of them, as reported in table 4.10. From the extrapolated value and the result obtained from each grid a relative error can be computed such that the grid quality can be assessed.

Table 4.10: Set of mesh discretization used for sensitivity analysis.

Mesh	Periodic nodes	Full-annulus nodes
Axial coarse	$60x40x1$	$60x40x120$
Axial medium	$80x40x1$	$80x40x120$
Axial fine	$100x40x1$	$100x40x120$
Radial coarse	$60x40x1$	$60x40x120$
Radial medium	$60x60x1$	$60x60x120$
Radial fine	$60x80x1$	$60x80x120$
Tangential coarse	$60x40x1$	$60x40x120$
Tangential medium	$60x40x2$	$60x40x240$
Tangential fine	$60x40x3$	$60x40x360$

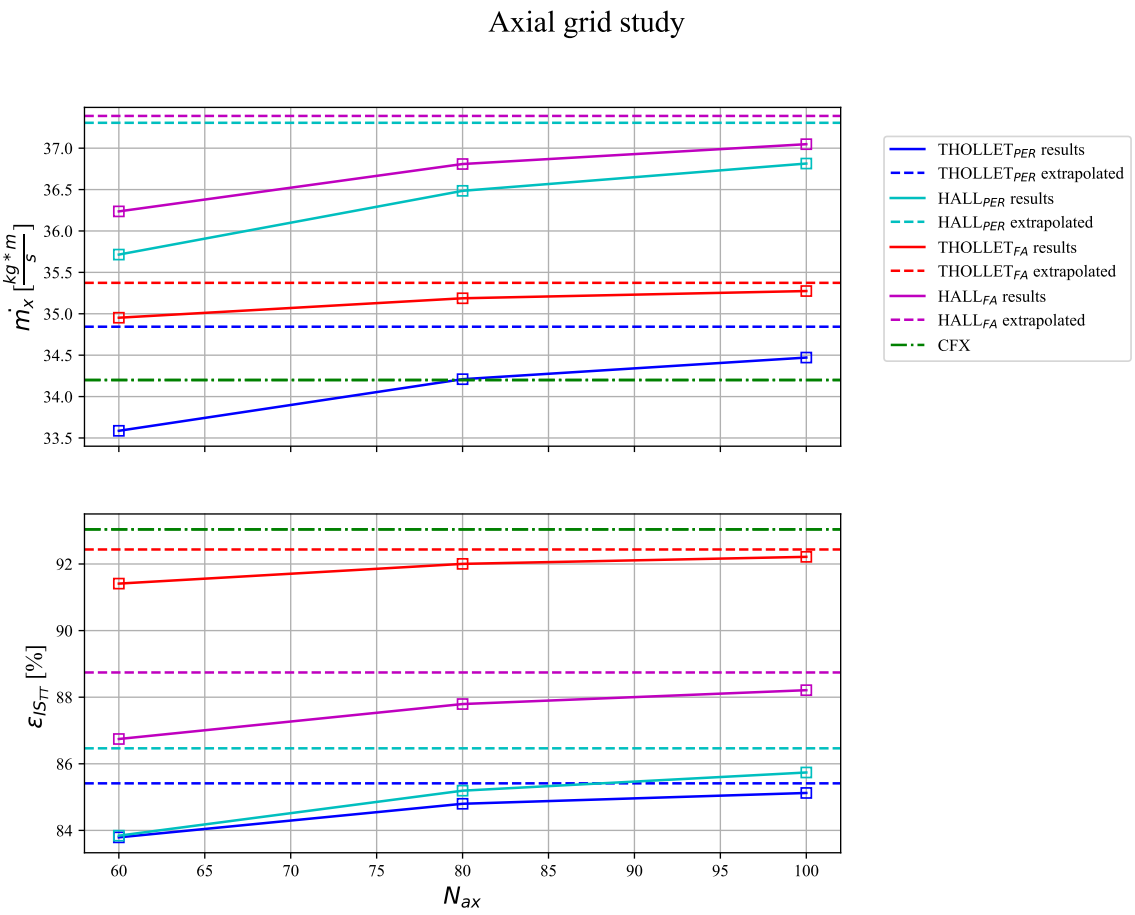

Figure 4.8: Axial grid convergence trend comparison between Hall and Thollet for both periodic and full-annulus domains.

From figure 4.8 it can be observed that the axial node count is a crucial parameter of choice in order to obtain grid independence both for Hall's and Thollet's model. This is related to the need to finely discretize the blade region in order to capture the local flow turning. The most critical points have been identified as the LE and TE, where the blockage gradients are more critical. The axial discretization is also fundamental to avoid significant numerical error due to the high cells dimensions at the inlet and outlet.

Comparing periodic result it can be observed, as expected, that Hall's simulation significantly overestimates the amount of mass flow passing through the channel, while Thollet's model is able to better capture it thanks to the metal blockage effect implementation. Regarding the efficiency, it appears clear how the periodic simulation produces similar results for both models, suggesting that the losses due to the drag parallel force have a limited impact in the transonic fan with respect to other sources.

If the respective full-annulus and periodic results are compared a marked difference can be found. As it is shown from the plot such deviation is significantly higher for the efficiency with respect to the mass flow rate. This is due to the efficiency being a more general source of information, since it depends from multiple variables, thus being more influenced by local flow changes. This difference is further enhanced in Thollet's simulations, reaching more than 5 percentage points. As it will be later explained in section 4.3.5 this is linked to the tangential flow stratification experienced with Thollet's model, which can fully develop only in the FA domain.

The hereby described behaviour can be found also in radial and tangential grid studies (Fig. 4.9 and 4.10) Despite the registered differences between models, the curves present converging trend for every domain. This highlights a successful grid convergence study and the possibility to select a mesh that gives grid-independent results.

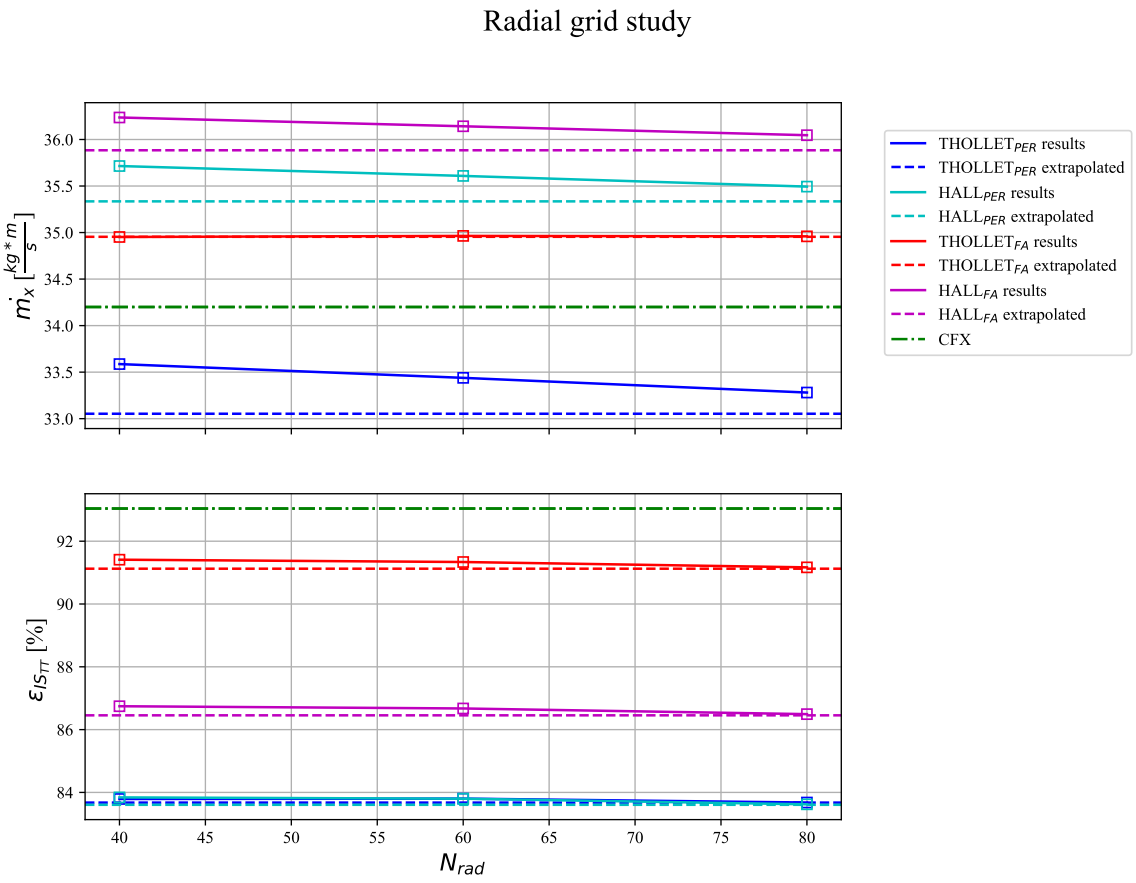

Figure 4.9: Radial grid convergence trend comparison between Hall and Thollet for both periodic and full-annulus domains.

The radial results highlight that refining the grid in this direction does not influence the

studied variables. This is a consequence of ignoring the tip gap and the endwall boundary layer, a preliminary decision that allowed to adopt an homogeneous spanwise discretization. In case these contributes are considered a further study on the grid refinement level near the extremities should be carried over in order to asses the BFM applicability.

An important point of interest that can be drawn from the radial study, as well as from the tangential one, is the periodic Thollet $\dot{m}$ inferior to CFX value. This appears to be in contrast with other simulations and has been associated to the already noted periodic issue. It moreover emphasizes the necessity to increase the axial refinement in order to better represent the blade effect as depicted in Fig.4.8.

For the case here studied the not influential radial discretization allows to reduce the number of mesh elements and to speed up significantly the simulation time in the design process.

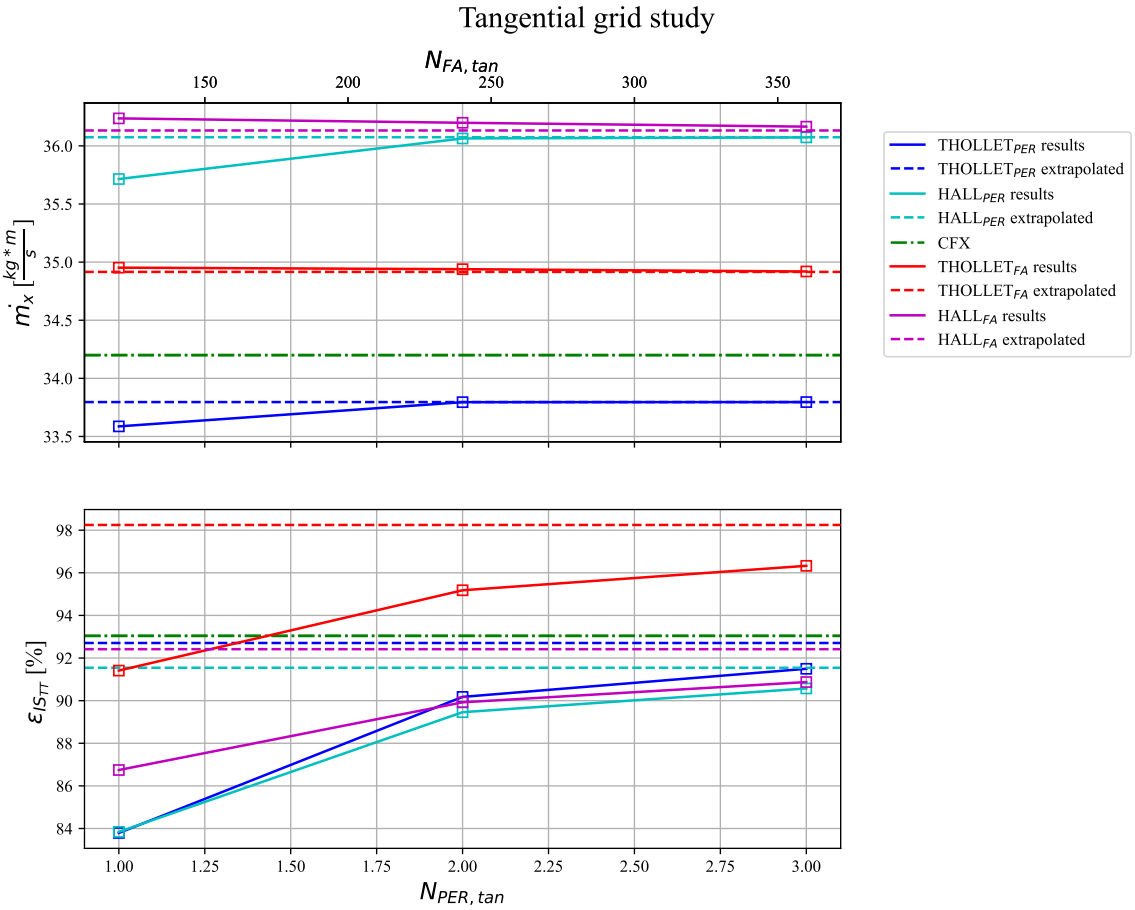

Figure 4.10: Tangential grid convergence trend comparison between Hall and Thollet for both periodic and full-annulus domains.

From the tangential results it can be seen how the refinement in this direction is remarkably influence the machine efficiency. By comparing this graph with the axial study it is possible to observe some significant differences in terms of parameters of merit: while the mass flow appears to be similar to the axial one, the efficiency is much higher than before, with the values from Thollet's model being greater than CFX. On the other hand, mass flow shows almost no dependency from tangential refinement, except for the single periodic cell issue. This suggests once more that BFM could be used with low tangential resolution to obtain the reasonable mass flow rate results, while, for efficiency, it is required to improve the discretization to better resolve the local flow thermodynamics.

From figure 4.10 the influence of periodic boundary condition can be assessed once more: parameters changes are more pronounced in the periodic domain, especially from 1 to 2 periodic tangential nodes. This underlines that the periodic boundaries mismatch can be smoothed using multiple tangential cells.

The following conclusions are listed regarding the grid convergence study:

1. both the efficiency and the mass flow show convergent behaviour for mesh refinement;
2. the convergence rate appears to be monotonic and consistent between the methods;
3. both models show an higher mass flow rate with respect to CFX simulation and a lower efficiency, with the exception of full-annulus Thollet;
4. while mass convergence is independent from tangential resolution efficiency is not;
5. there is a consistent discrepancy between periodic and full-annulus domain results which can be traced back to BC issue. This difference is further enhanced in Thollet's model due the blockage factor implementation (it will be further examined in section 4.3.5);
6. the gain in terms of accuracy passing from a medium to a fine mesh is significantly less than from the coarse to the medium ones (see Appendix B);
7. during this grid convergence study the mass imbalance has been analyzed as well but no significant improvement has been obtained in such sense.

Thanks to the converging grid analysis and to the limited error with respect to asymptotic values, BFM appears to be a good candidate for the scope of the thesis. From the reported conclusion it has been decided to perform all the subsequent computations, for flow analysis and design purposes, using meshes with $100 \times 40 \times 3$ and $100 \times 40 \times 360$ for periodic and full-annulus geometries respectively. This choice is driven by a reasonable

trade-off between accuracy and computational time. A coarser grid could also be used for preliminary computations taking into account the level of error introduced.

4.3. Methods comparison

In this sections the flow results obtained from SU2 and CFX are and the two studied models are evaluated in terms of global performances, in order to assess BFM preliminary design applicability. Afterward the comparison are reported in terms of mass flow averaged results across axial and radial slices. This is useful to highlight the locations of major inconsistencies between BFM and PBC. In each plot 4 curves are reproduced to show the differences between Hall and Thollet for both periodic and full-annulus domains. Subsequently the computational time associated to the method is reported and the refinement influence over computational cost is presented. From the time comparison it is possible to evaluate the method efficiency and to asses whether or not it could be applied in design procedures. In the last subsection the local flow visualization is plotted and the problems related to tangential flow stratification are examined.

4.3.1. Global performance

As previously reported in the grid convergence analysis the periodic domain is currently less accurate then the FA representation. In order to assess BFM applicability to preliminary fan blade design, the global performances of interest have been computed for a mesh with $100 \times 40 \times 360$ nodes.

The comparison between BFM and CFX is shown by table 4.11

Table 4.11: SU2 results.

Parameter	CFX	Hall	Err_{HALL}	Thollet	$Err_{Thollet}$
$\dot{\boldsymbol{m}}$	$34.20\,[kg\ s^{-1}]$	$37.04\,[kg\ s^{-1}]$	8.3%	$35.29\,[kg\ s^{-1}]$	3.19%
$\boldsymbol{\eta}$	93.06%	92.69%	0.4%	97.53%	4.8%
$\boldsymbol{\Pi}$	1.68	1.71	1.79%	1.69	0.60%

The results show an encouraging error level, especially for Thollet's formulation with respect to CFX. While it has been registered a increase in the efficiency error, this model is still able to compute it between 5 percentage point difference, while it well approximate the values of mass flow rate and pressure ratio.

4.3.2. Axial pattern

The plots hereby displayed depict the axial position in meters on the x-axis and the mass flow averaged parameter of choice on the y-axis. The different variables have been normalized over the respective inlet total quantity to better visualize their trend. While the mass flow averaged axial representation does not fully describe BFM features, it is a useful to address its global accuracy.

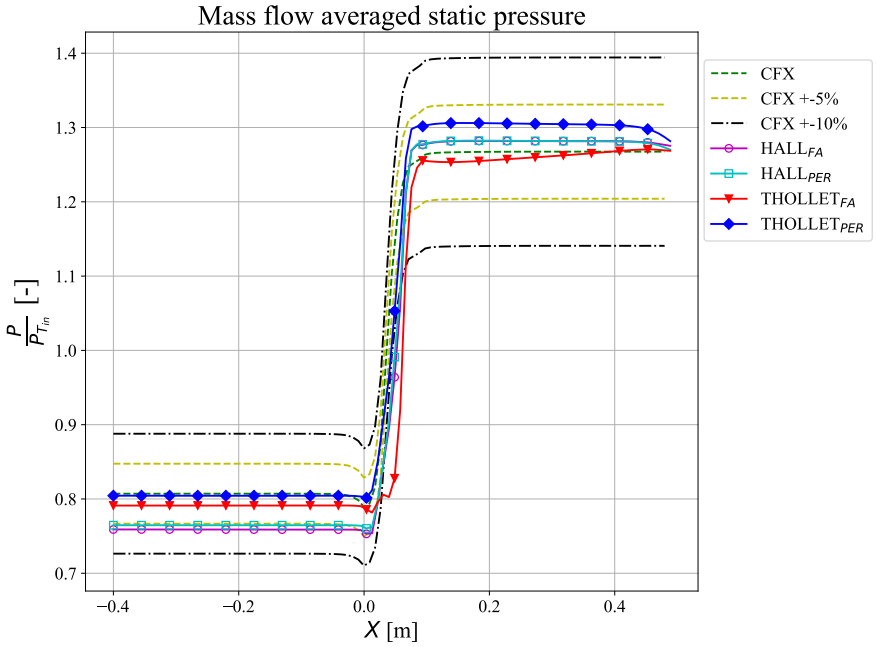

Figure 4.11: Mass flow averaged static pressure trend along axial direction.

From the mass flow averaged pressure trend reported in figure 4.11 it is possible to observe how the BFM results strongly resemble the PBC ones. The relative discrepancy is generally inferior to 5 percentage point, except near the LE for Thollet's full-annulus simulation. From what can be seen full-annulus Thollet's values appear to be closer than Hall's ones to the CFX both at the inlet and at the outlet. Hall's periodic and FA results appear to overlap, while for Thollet's simulation the curves are clearly distinguished. This is a general trend observed also in the following plots.

A similar behaviour can be observed also for the static temperature plotted in figure 4.12. The value decreases for a short period starting from the blade section, then it gets closer to the desired dimension. While this pattern is present in both periodic and full-annulus domains, in the former case it is hindered by the imposed BC.

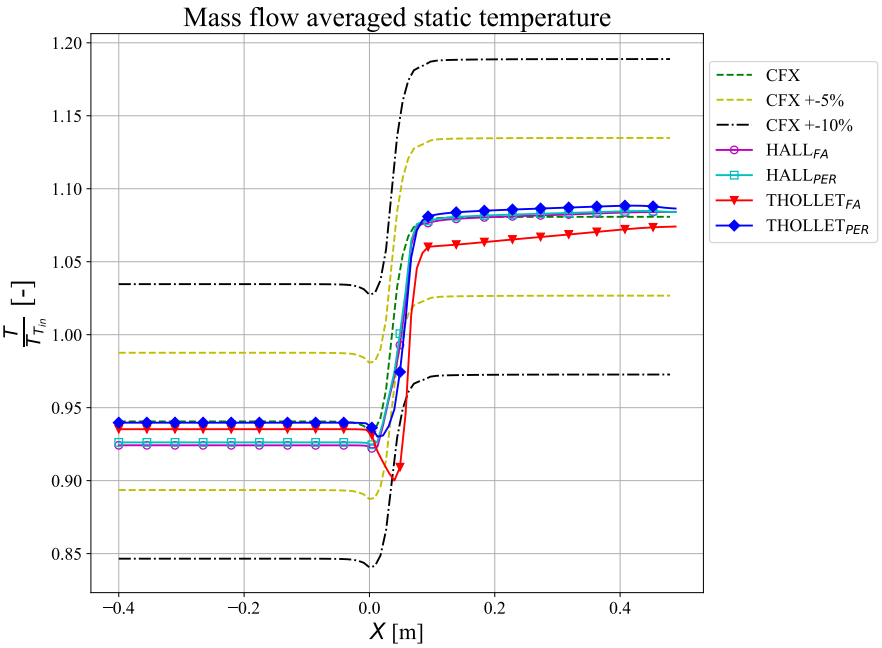

Figure 4.12: Mass flow averaged static temperature trend along axial direction.

Looking at stagnation pressure from figure 4.13, it can be noticed a smoother incremental trend without the LE local drop. While this variable presents local deviation greater than 10% across the blade region, the values at the outer sections strongly agree with CFX results. As in previous graphs, the FA Thollet's simulation is the best one to capture outlet conditions, granting a P_{tot} ratio close to CFX, as already shown in table 4.11.

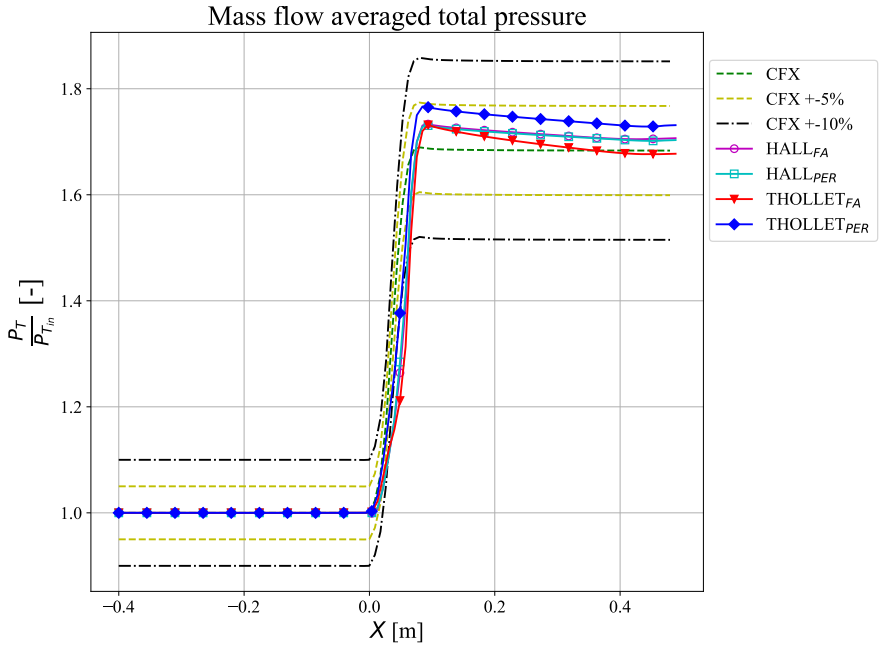

Figure 4.13: Mass flow averaged stagnation pressure trend along axial direction.

Different results are experienced for the stagnation temperature. Their trend is plotted in Fig. 4.14. In this case the full-annulus Thollet produces lower exit temperature values than CFX, while the other methods closely agree on a slightly greater T_{tot}. This distinction is the reason for which the Thollet's isoentropic efficiency, reported in section 4.2.4, is greater than the CFX computed one.

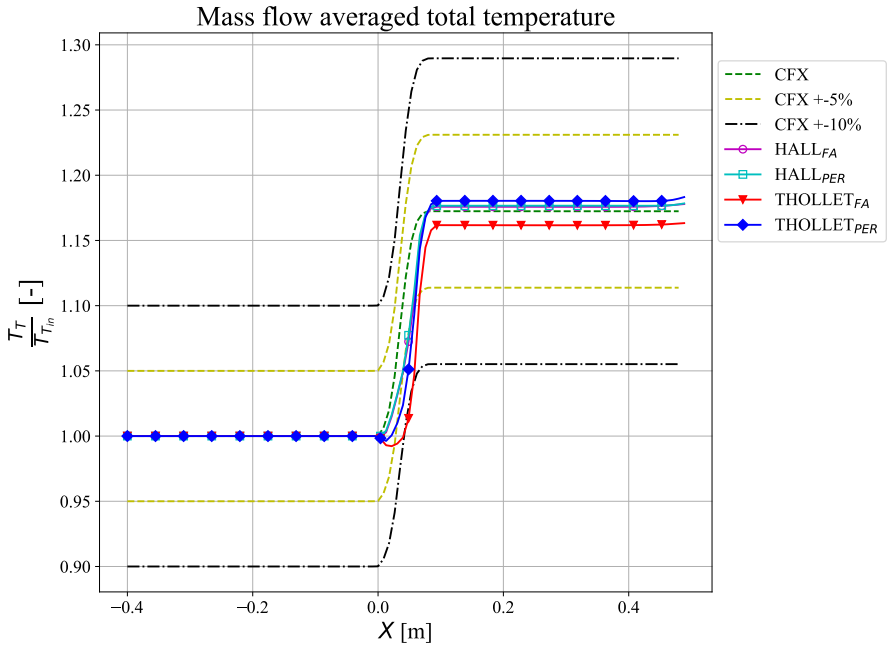

Figure 4.14: Mass flow averaged stagnation temperature trend along axial direction.

Less accurate results are found in the mass flow averaged Mach number in standard frame. This thermodynamic variable seems to remain almost stable in Hall's simulation. Its value is closer to the one registered after the blade. In the blade region it presents a minimum, probably linked to neglecting metal blockage in this model. The lack of such contribution clearly undermine the flow acceleration usually encountered in the converging channel created by the nearby blades. For periodic Thollet's run lower speed is registered before the blade. The flow is in fact accelerated as it encounter the LE thanks to the channel area contraction reproduced by the metal blockage effect. From that point on the results are comparable to Hall's one. On the other hand, for Thollet's FA computations, the Mach exhibits a peak in the blade region. There the local error spikes over the 10 percentage points, just to get back down to the expected value in the outlet section. An interesting aspect is the small Mach rise encountered near the outlet for each simulation. This curvature change is linked to the solver low stability region located at the outlet boundary.

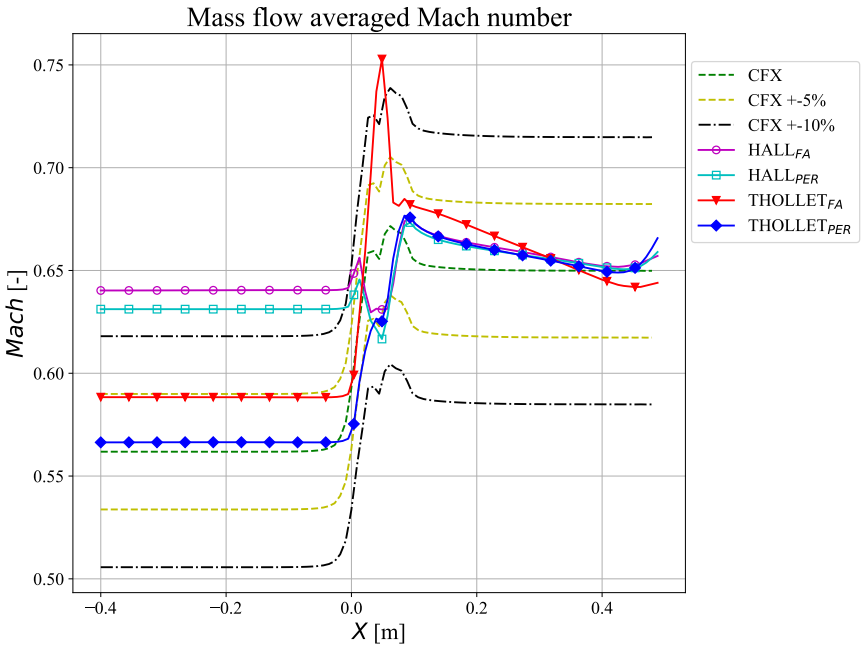

Figure 4.15: Mass flow averaged Mach number trend along axial direction.

Lastly from the flow angle plot 4.16 the deflection imposed in BFM can be assessed. Differently from CFX, in this case, BFM overestimates the local flow turn previous the blade exit. Then, once the forcing term vanishes, the fluid tends to steadily get back to a regular axial direction. While the overturning region near TE is easily distinguishable from CFX, the global trend of the flow turning is well in accordance with it.

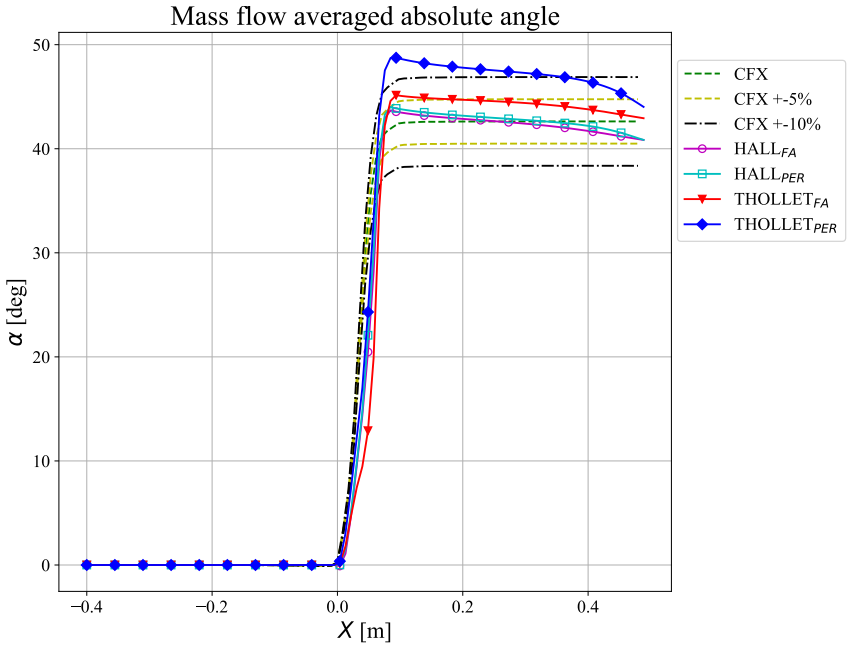

Figure 4.16: Mass flow averaged absolute flow angle trend along axial direction.

4.3.3. Radial pattern

The flow has also been studied in radial direction at 4 distinct axial locations: inlet, LE, TE and outlet. While inlet spanwise variables distribution presents homogeneous properties, as it was noticed also in axial study, different results are experienced near the blade and they are hereby reported. For completeness the plots not reported here have been inserted into Appendix C.

In figure 4.17 it is shown the flow deflection just before the LE. From this plot it can be observed that neglecting the physical blade affects the eventual shock wave position. In CFX a detached shock occurs (see Fig.4.3) before the LE, due to the supersonic flow not being able to curve according to the highly twisted blade. The consequence is that the flow starts turning before the blade, as shown from alpha in this plot. In BFM simulations, since the physical blade is not present, there is no LE shock wave and the flow turning is delayed. This will inevitably affect the quality of results (see section 4.3.5).

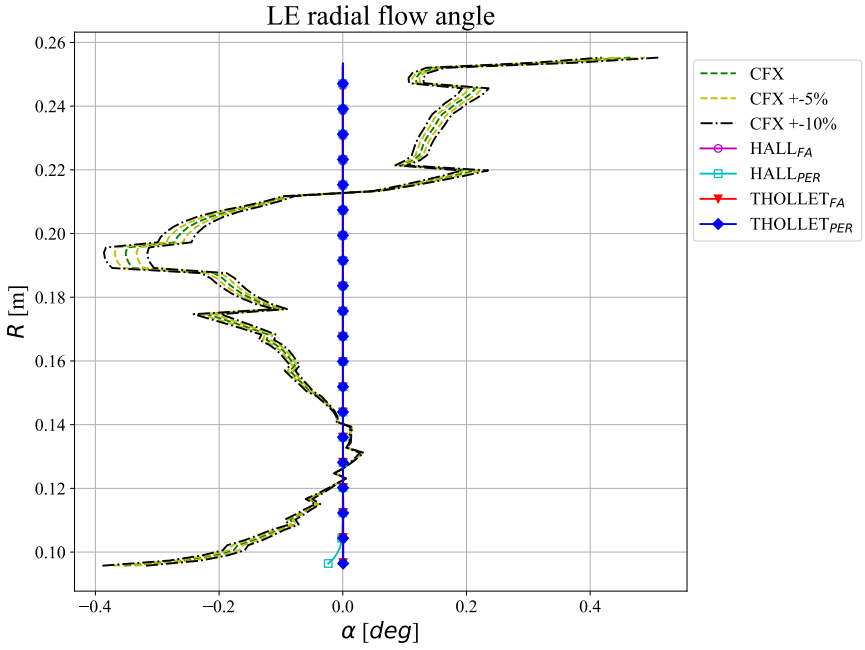

Figure 4.17: Mass flow averaged absolute flow angle trend in radial direction at the LE.

Looking at the values of mass flow averaged Mach number from Fig.4.18,it appears that full-annulus Thollet's representation constitutes a good alternative to CFX. It well represents CFX trend with an error percentage lower than 5 percentage points. Hall's model shows a similar behaviour but translated out of the 10 percentage points bound. This reflects what has been shown in the axial mass trend, which overestimate the value before the blade because the metal blockage was not considered.

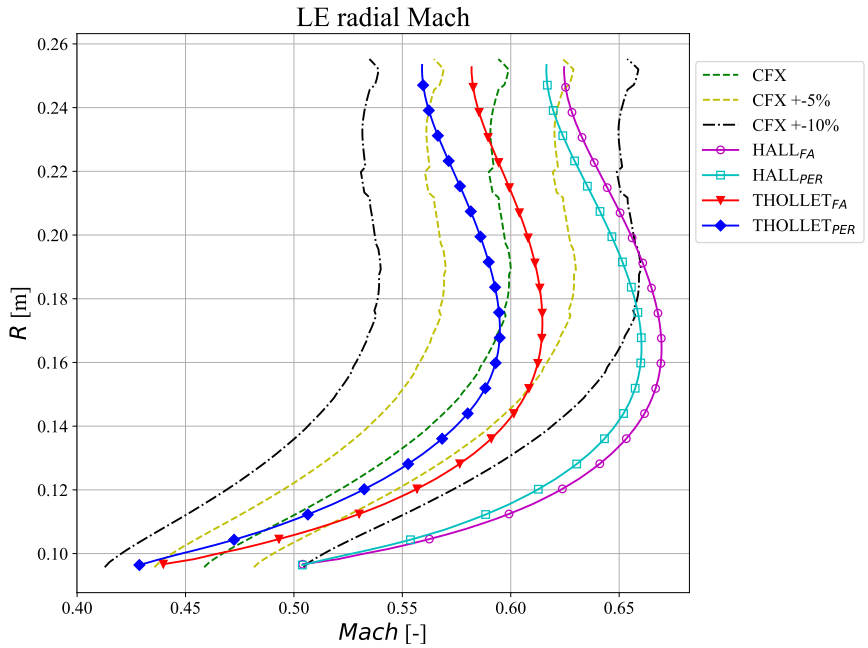

Figure 4.18: Mass flow averaged Mach trend in radial direction at the LE.

In figures 4.20 and 4.19 the total pressure and temperature are represented. In CFX P_{tot} increases along the span to grant the radial equilibrium. In BFM instead the blade appears not to influence the upstream region, leaving the initial channel unchanged from what was imposed at the inlet. This matches what was found in the axial BFM plots.

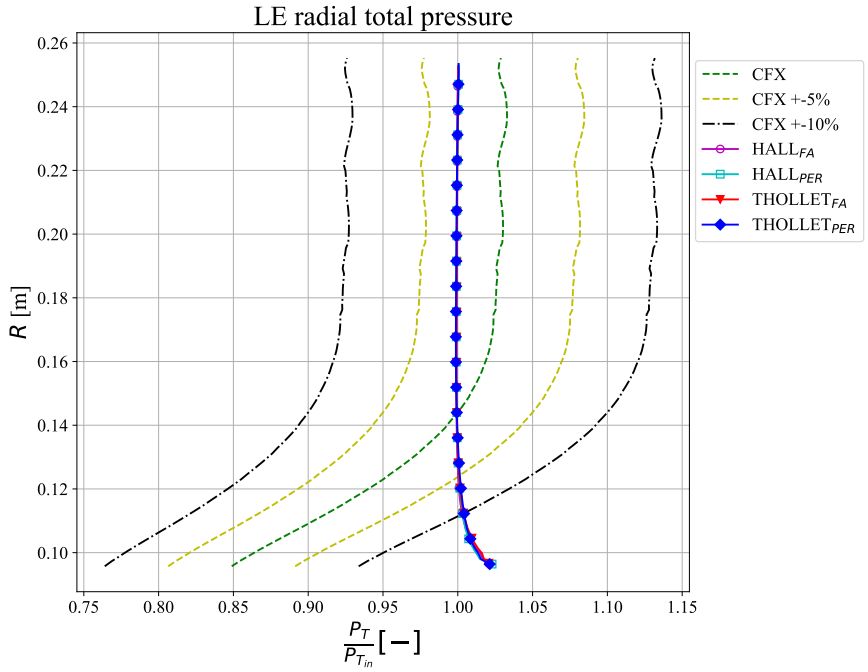

Figure 4.19: Radial total pressure trend at the LE.

The same radial behavior of the total pressure is shown by T_{tot} in Fig. 4.20. The total variable shows no change before the body-force region neither in axial or in radial direction. All the BFM methods produce the same overlapping lines.

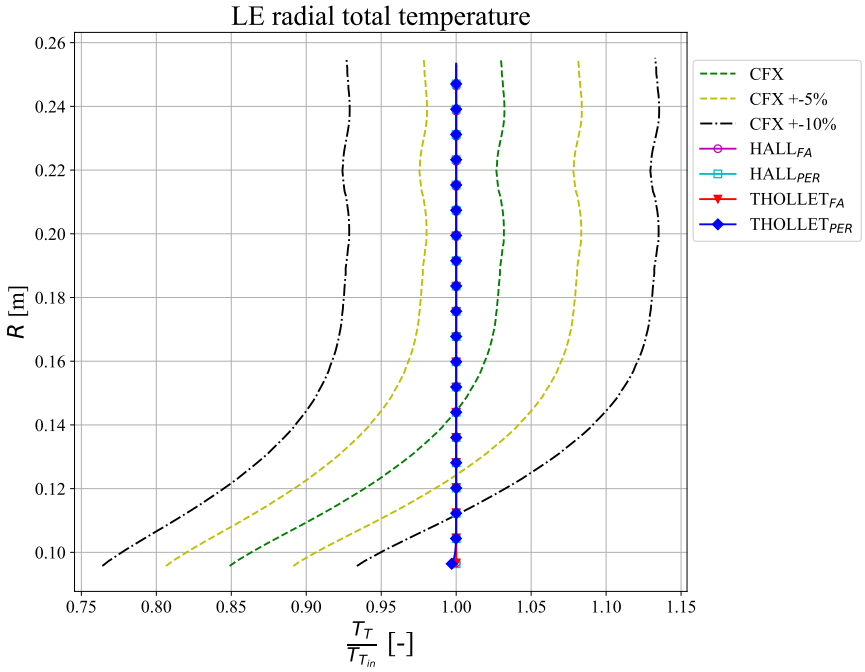

Figure 4.20: Radial total temperature trend at the LE.

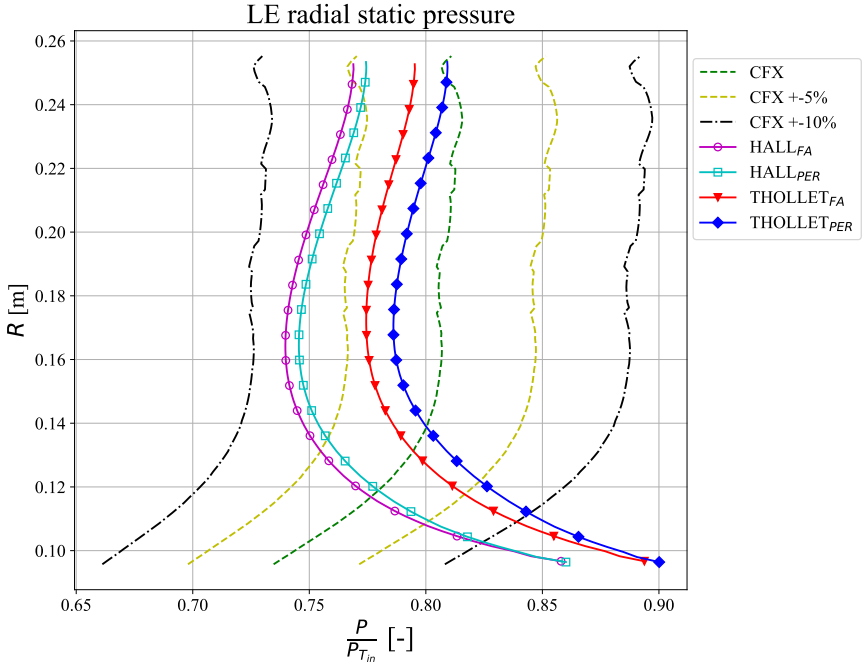

Figure 4.21: Mass flow averaged pressure trend in radial direction at the LE.

Looking at LE static pressure and temperature (Fig. 4.22 and 4.21) BFM reports significant differences with respect to CFX, especially near the hub. While for upper regions the results tends to straighten up as CFX, at lower span section it curves in the opposite direction: here P and T results higher than what CFX predicts. This is due to their total counterpart that is almost constant in radial direction. Thollet's model produces greater error because of the lower dynamic pressure, coming form the higher Mach, which in turn involves a bigger static counterpart for the same total value.

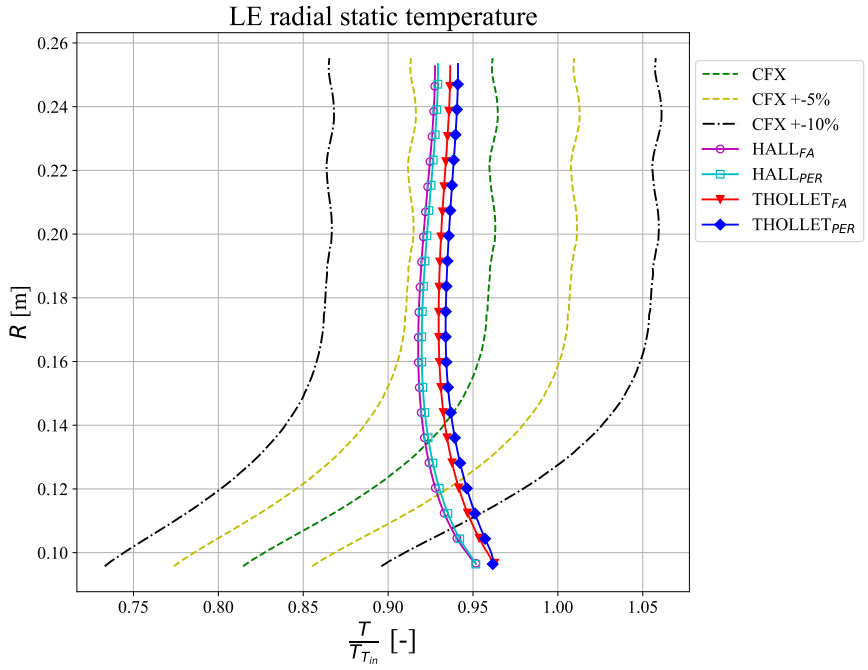

Figure 4.22: Mass flow averaged temperature trend in radial direction at the LE.

At the blade TE section, the homogeneous condition registered in Fig. 4.17 is no more present. Here the turning has been imposed to the flow angle by the force field. As it can be observed from Fig. 4.23, *alpha* values appears to agree for CFX and BFM in the upper span sections, where greater direction change, inked to the more staggered profiles, are reported. Differently, near the hub, the BFM produces an inverse curvature with respect to the other CFD computation, inducing pronounced errors. In this case Hall's solution is closer to the CFX one with respect to Thollet's one. As it will be shown in section 4.3.5, this is caused by the presence of tangential flow stratification issue in Thollet's FA simulation. Such non physical effect prevents the model from matching the expected results, especially in low span regions, where it has been shown to be most influential. The periodic Thollet's results present the same trend as Hall's ones, but they are shifted due to the additional source terms present in the equations.

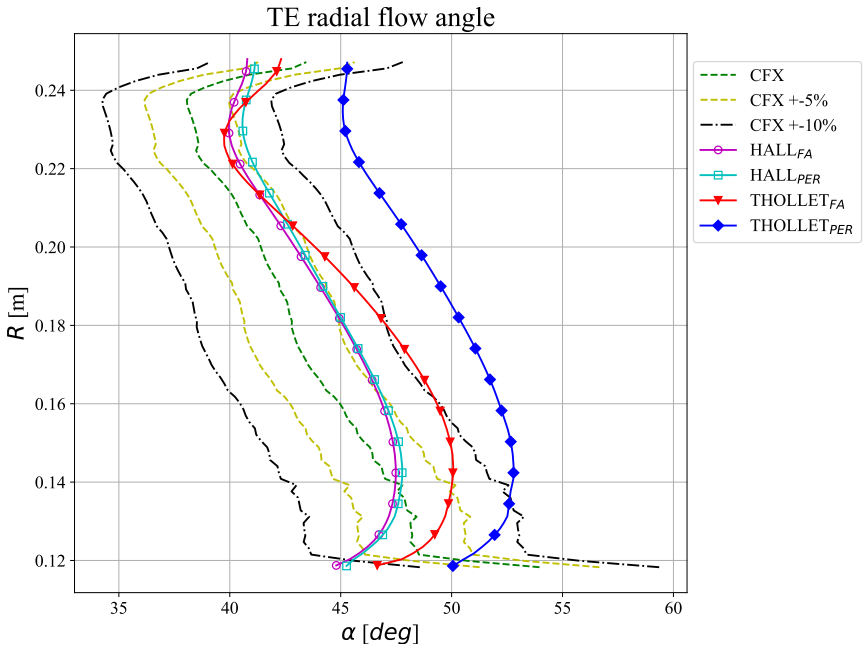

Figure 4.23: Mass flow averaged absolute flow angle trend in radial direction at the TE.

From figure 4.24 the TE Mach number can be studied. Differently from what was found at the LE, here all the BFM computations seem to well reproduce CFX curves, falling into the 5 percentage points boundary. The only exception is made by Thollet's FA simulation near the blade extremities.

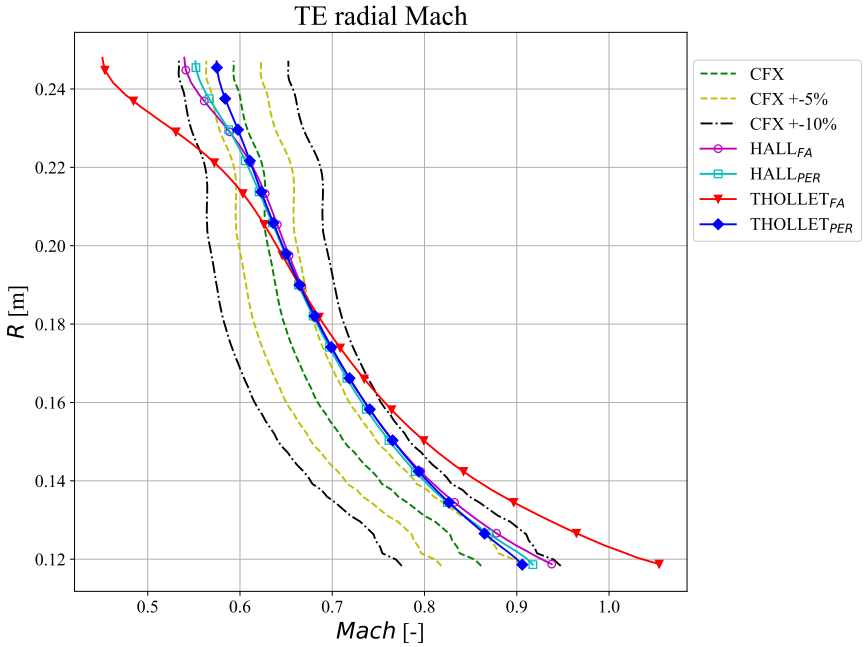

Figure 4.24: Mass flow averaged Mach trend in radial direction at the TE.

In Fig. 4.25 the total pressure after the blade is reported. Similarly to what was shown at the LE, also here BFM trends are almost linear. The radial P_{tot} rise found is in fact significantly smaller then what CFX predicts. The completely different FA Thollet's results highlights that this model is not currently suited for accurate local flow representation.

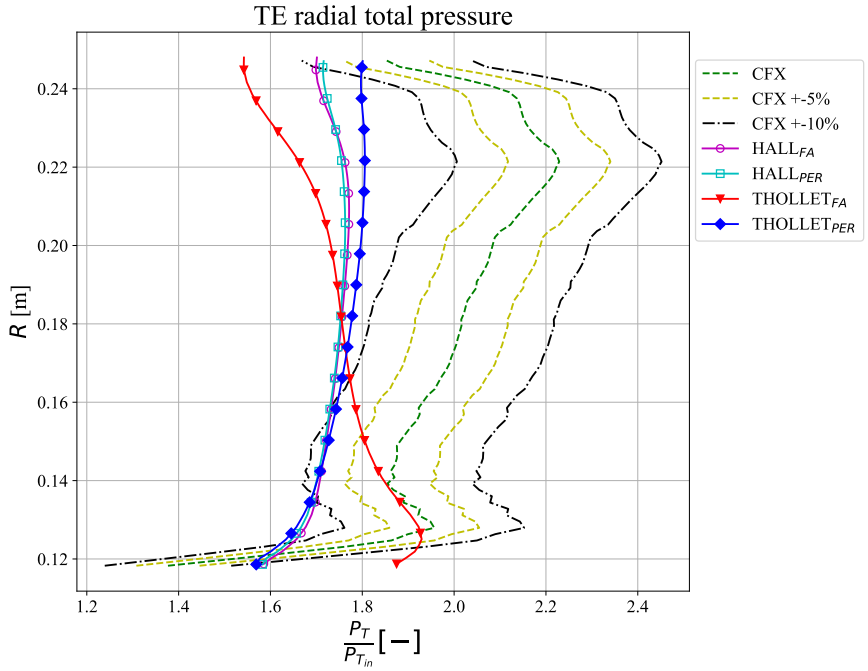

Figure 4.25: Radial total pressure trend at the TE.

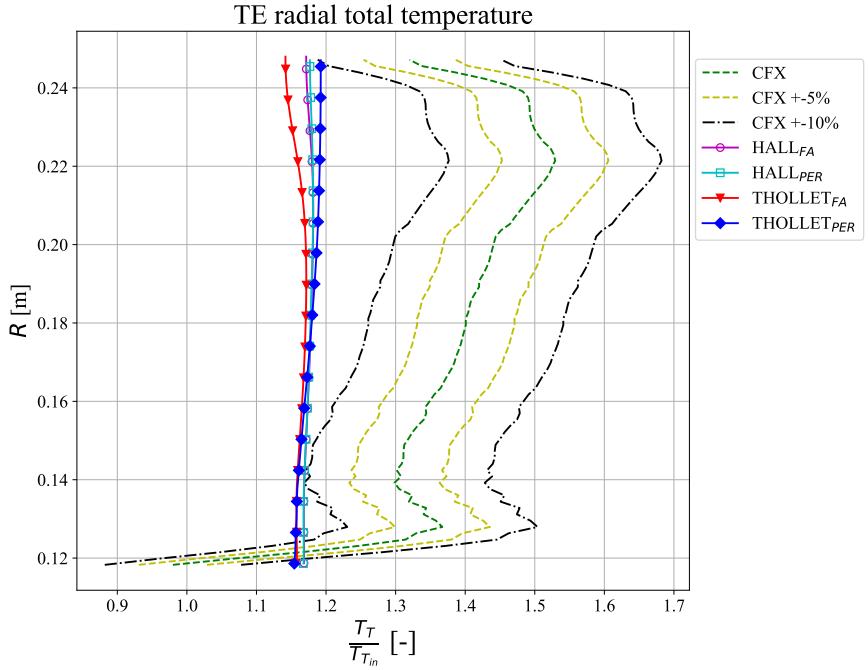

Figure 4.26: Radial total temperature trend at the TE.

Similarly to P_{tot}, also the BFM total temperature at the TE appears to be radially constant. Both the these variables plots are characterized by a substantial error greater than 10%. As evinced from Fig. 4.26 this thermodynamic variable does not suffer from the stratification influence as found for total pressure. This is shown also in plots 4.35, 4.36 and 4.37. It appears that BFM smears out the flow after the blade. The radial pattern is indeed mildly curved and does not report the local bumps registered in CFX. This is probably attributable to the wake modelization that was not computed in BFM using Euler solver, and to the shock wave absence which differently affect the various spanwise sections. The only distinction between shroud and the hub region, in BFM, is linked to rotational velocity imposed to the flow, as the BL separation on the highly staggered profiles is not captured.

Close behaviour to the total pressure and temperature can be witnessed for thei static counterparts from Fig. 4.27 and 4.28. While it appears that FA Thollet's solution falls in line with the other methods, suggesting that the main difference comes from the dynamic component stratification, the general trend still remains out the acceptable 10 percentage boundary. As previously concluded in axial trend the BFM is not precise enough to capture local behaviour near the blade TE, but it would eventually produce reasonable global results.

Similar considerations described for the TE can be made for the outlet region plots, as reported in Appendix C.

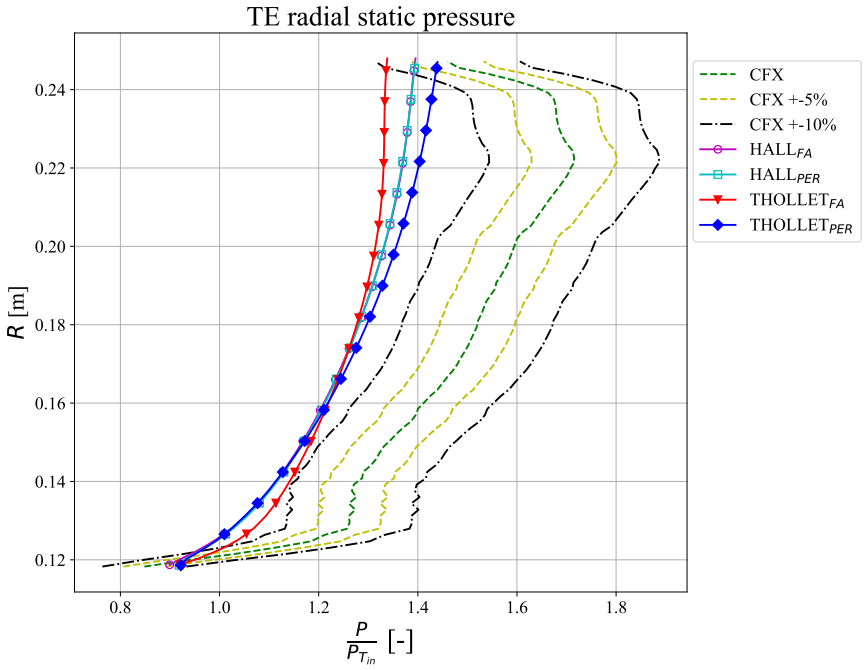

Figure 4.27: Mass flow averaged pressure trend in radial direction at the TE.

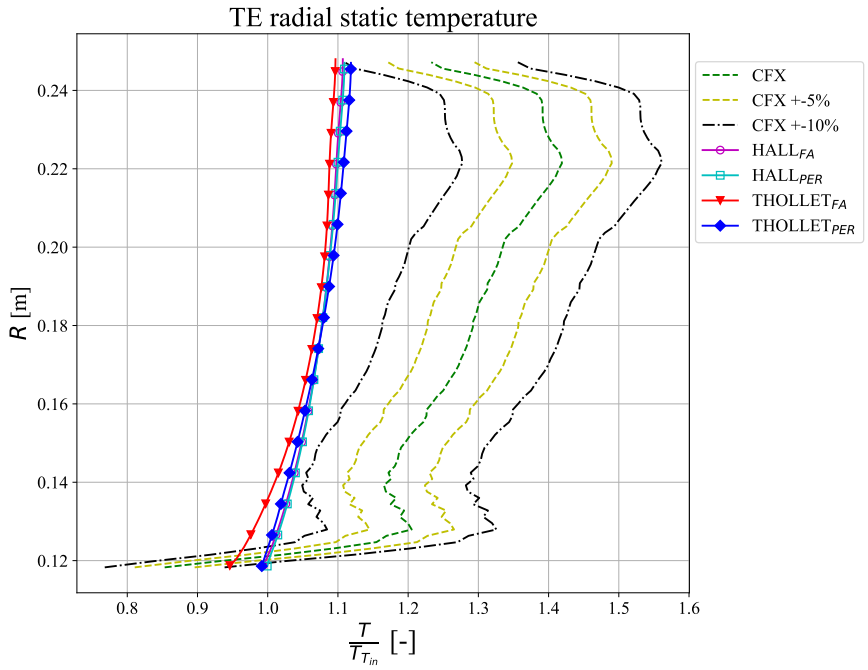

Figure 4.28: Mass flow averaged temperature trend in radial direction at the TE.

4.3.4. Computational cost

In order to be effective for design purposes, the model must be demonstrated to be time efficient. The simulations have been initially performed using a single processor on a personal computer to asses this quality, then for the iteration purposes the full-annulus ones have been switched to a more powerful machine in order to reduce the required resources cost.Several grid refinement level have been analyzed as shown in section 4.2.4 and the necessary computational time has been compared to CFX one. The results here shown refer to Thollet's model, but close values are obtained also for Hall's simulations.

Table 4.12: Computational cost comparison.

Method	$Time_{interpolation}$ [s]	$Time_{iteration}$ [s]	$Time_{total}$ [s]	$Elements$
CFX	-	32.64	24480	$2.1922e^6$
BFM (100x40x360)	1363	40.62	22950	$4.32e^6$
BFM (100x40x3)	17	0.225	1373	$3.6e^4$
BFM (100x40x2)	12	0.179	1331	$2.4e^4$
BFM (100x40x1)	8	0.087	1409	$1.2e^4$

An interesting conclusion can be drawn from the time comparison: from the current limitations encountered in periodic the periodic simulation (see section 4.2.3) it is clear

that the time saving is much lower than what it can be achieved. The reduced stability shown in Fig.4.6 does indeed hinder the great time saving capabilities of the method. Despite the significant reduction in time required to perform each iteration, it is in fact necessary to perform at least one order more steps to make a periodic simulation converge. If the current stability issue is fixed, and the number of iterations becomes comparable to the 600 required in FA simulations, the model could be optimized to require less than 50 $[s]$ to fully converge, with a time saving of around 4 order of magnitude with respect to PBC.

Taking into account the limitations of the different methods, the full-annulus domain was the one selected to proceed in this thesis work. While the time requested is almost the same of the CFX, it must be kept in mind that the number of nodes used for the discretization is twice as much, and that with this method can be used to study flow non-uniformities as well. The amount of time saving obtained with BFM does classify it as an extremely attractive tool and extensively fulfill the requirements researched in a design tool.

4.3.5. Tangential Stratification of the Solution

With the aim to better understand the reasons behind the BFM behaviour the flow local pattern has been examined in detail. In particular the causes behind Thollet's full-annulus deviations from the other models, prevuiously anticipatd in sections 4.3.2 and 4.3.3, are hereby researched. This model does present a constant difference from the results obtained in the periodic domain, differently from what appears in Hall's case. This deviation shows a peak in the blade region as especially represented in figures 4.11, 4.12 and 4.15.

The annular flow domain has been unrolled and plotted at 3 different blade span as depicted in Fig.4.29. The cylindrical slice has been represented in function of the tangential angle θ measured in the plane (X,Y). The relative Mach number distribution is plotted such that a comparison can be made between Hall's and Thollet's results. At the same time is possible to confront the results also with CFX and experimental data from Fig.4.3. Remaining flow diagrams are reported in Appendix C.

Some conclusions can be drawn from observing the flow Mach number:

- No upstream influence of the blade region;
- Thollet's implementation shows a certain level of flow stratification in tangential direction, which seems to diminish with the span;
- both models fail to capture the LE shock wave.

Regarding the transonic flow behaviour in BFM, it can be noted that no shock wave is reported in these plots. Due to the absence of the physical blade, the model is in fact unable to see the metal edge inducing the detached shock wave. It has been demonstrated in [23] that the formulation is indeed able to capture the shock induced by pressure driven flows, such as in a supersonic nozzle, but, as the author reported, future work is necessary to obtain local dependency on the LE effect.

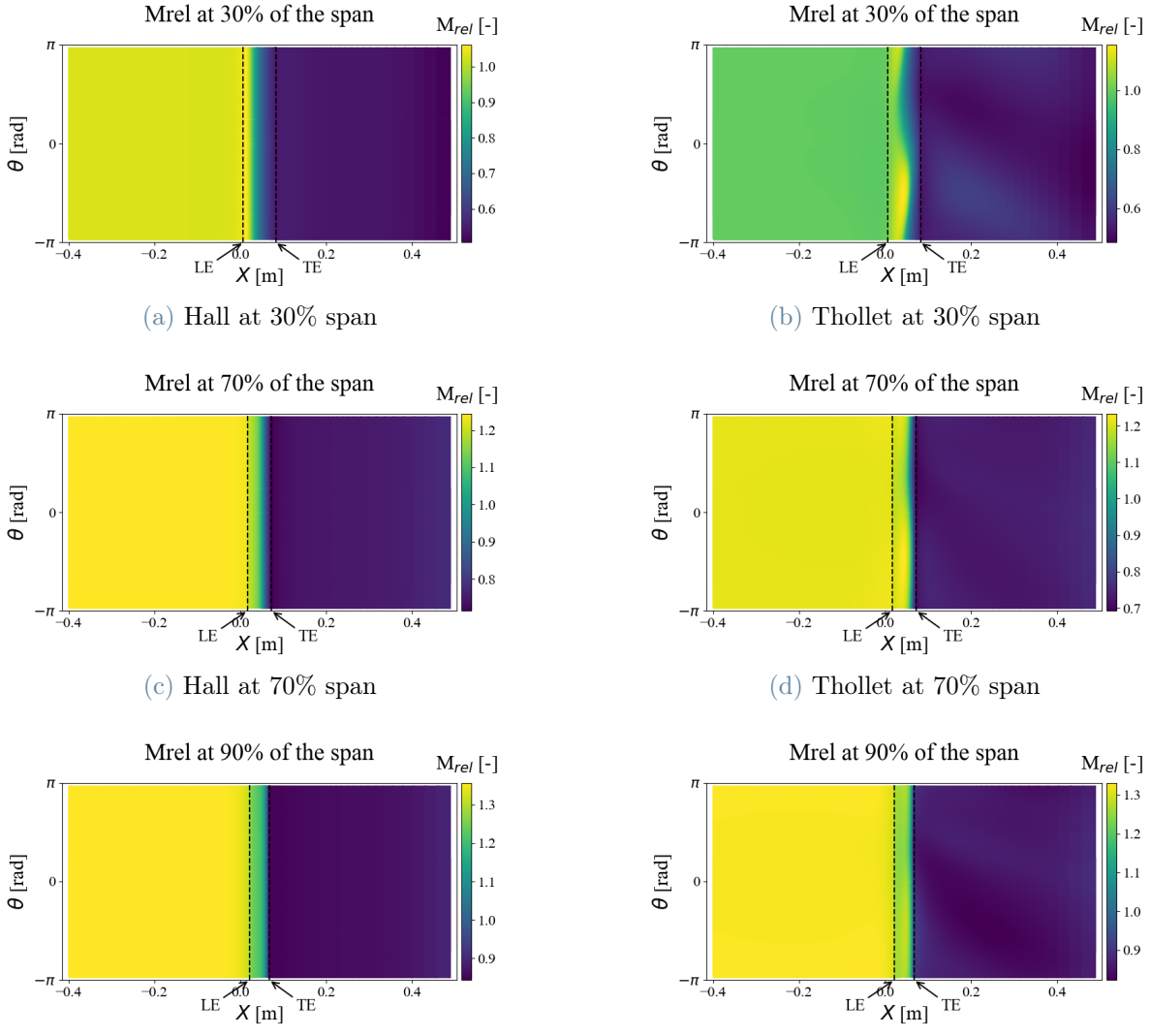

(a) Hall at 30% span

(b) Thollet at 30% span

(c) Hall at 70% span

(d) Thollet at 70% span

(e) Hall at 90% span

(f) Thollet at 90% span

Figure 4.29: Comparison between Hall's and Thollet's resulting flows. The blade-to-blade plane view at different spanwise sections show the flow stratification in tangential direction.

The flow stratification in Thollet it appears clear from the undulatory trend of variables encountered from midblade. From the results it can be assessed that this effect has greater

influence near the hub with respect to the tip section. This is true for most of the flow variables with the exception of momentum, which increases along height of the blade (see Fig.4.35, 4.36 and 4.37). Such issue can be qualitatively assessed looking at the flow across cylindrical slices from figures 4.31, 4.32, 4.33 and 4.34. As it was speculated in previous sections the tangential stratification can fully develop only in FA Thollet's simulations, and not in periodic one. The reason is believed to be the strict BC imposed on the second domain which prevent the phenomena to have the same magnitude in the single channel as shown from Fig. 4.30. The flow stratification is not present at all in Hall's simulation. It can then be associated to an incorrect blockage factor implementation, which constitutes the only difference between the methods.

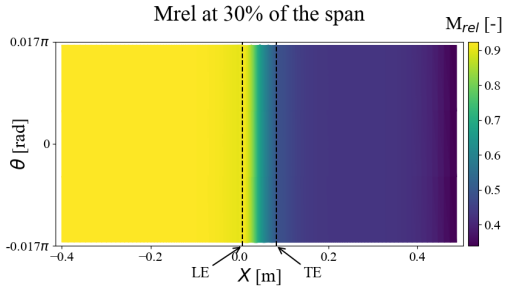

(a) Periodic Thollet at 30% span

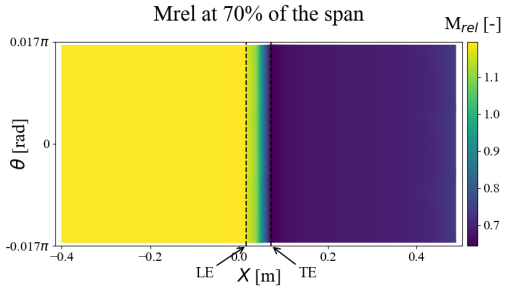

(b) Periodic Thollet at 70% span

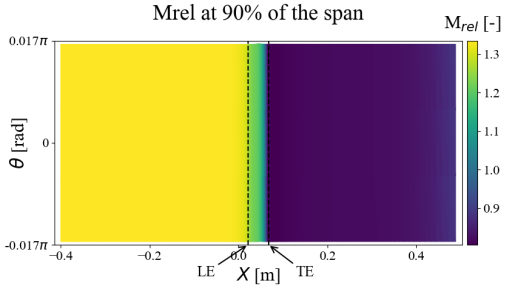

(c) Periodic Thollet at 90% span

Figure 4.30: Periodic Thollet's resulting flows. The blade-to-blade plane view at different spanwise sections show no stratification in tangential direction.

The flow stratification effect can be quantified in terms of tangential flow variables standard deviation from figures 4.35, 4.36 and 4.37. This behaviour represent a non physical characteristic for such axis-symmetric problem and can be traced back to a problem in the blockage factor implementation, the only source of difference between Hall and Thollet. Unfortunately it was not possible to find out and fix this error in the time span of this work.

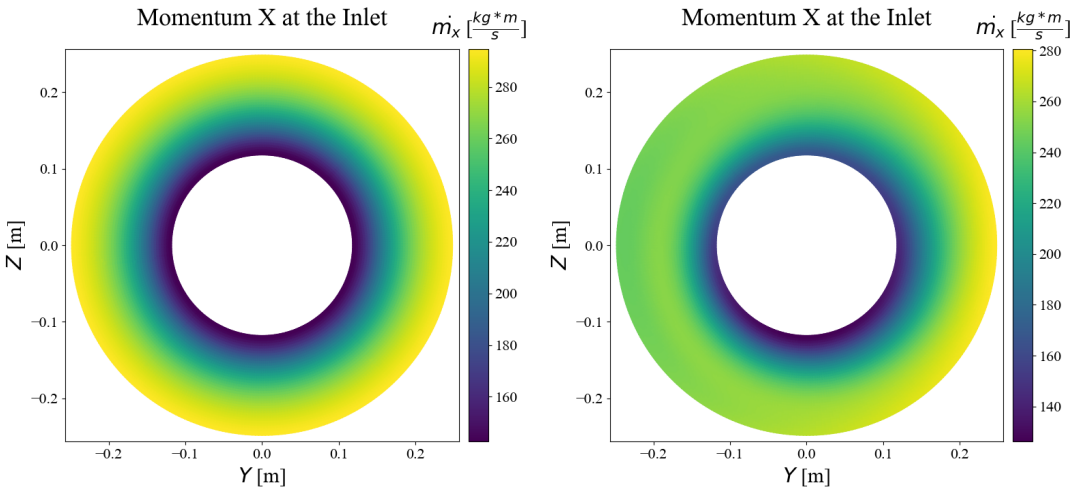

(a) Hall at the inlet (b) Thollet at the inlet

Figure 4.31: Comparison between Hall's an Thollet's resulting flows. Circular sections at the inlet circular section.

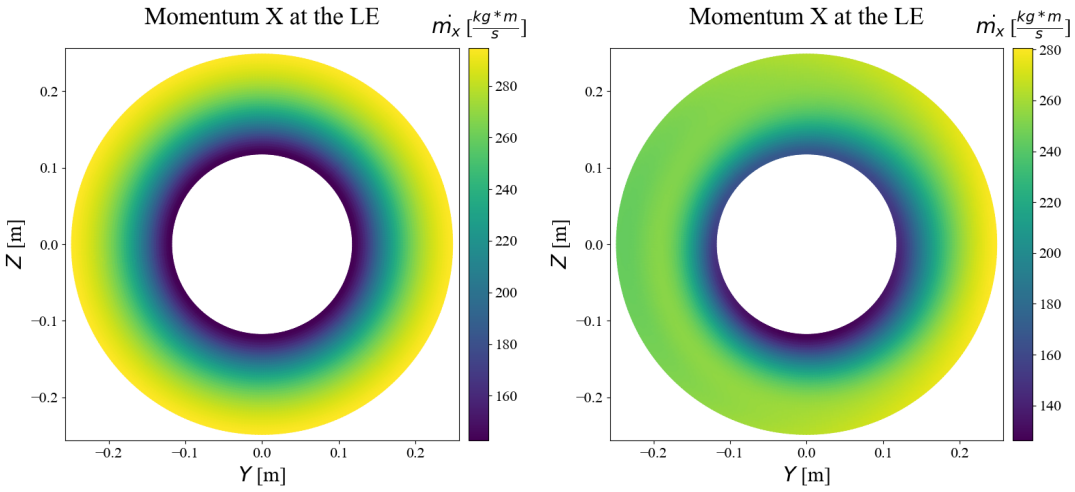

(a) Hall at the LE (b) Thollet at the LE

Figure 4.32: Comparison between Hall's an Thollet's resulting flows. Circular sections at the LE circular section.

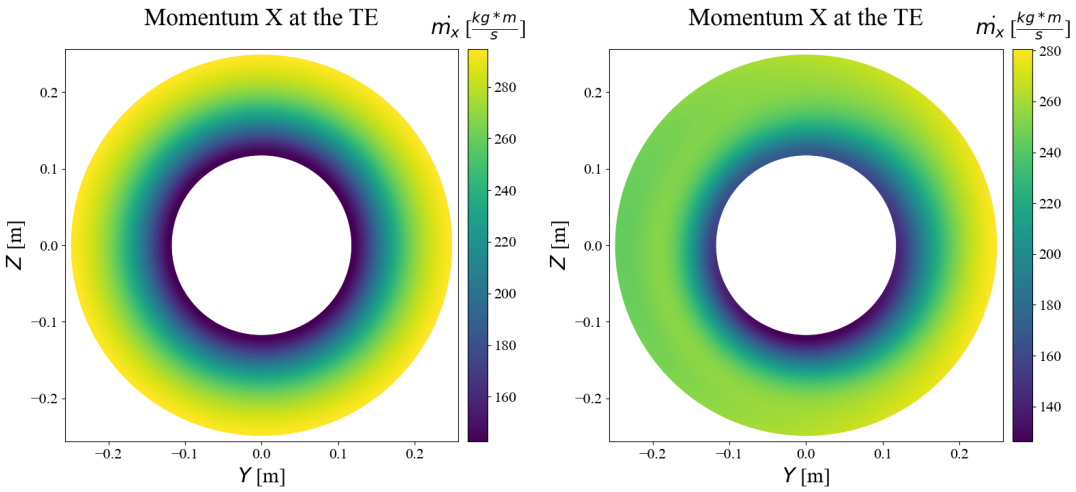

(a) Hall at the TE (b) Thollet at the TE

Figure 4.33: Comparison between Hall's an Thollet's resulting flows. Circular sections at the TE circular section.

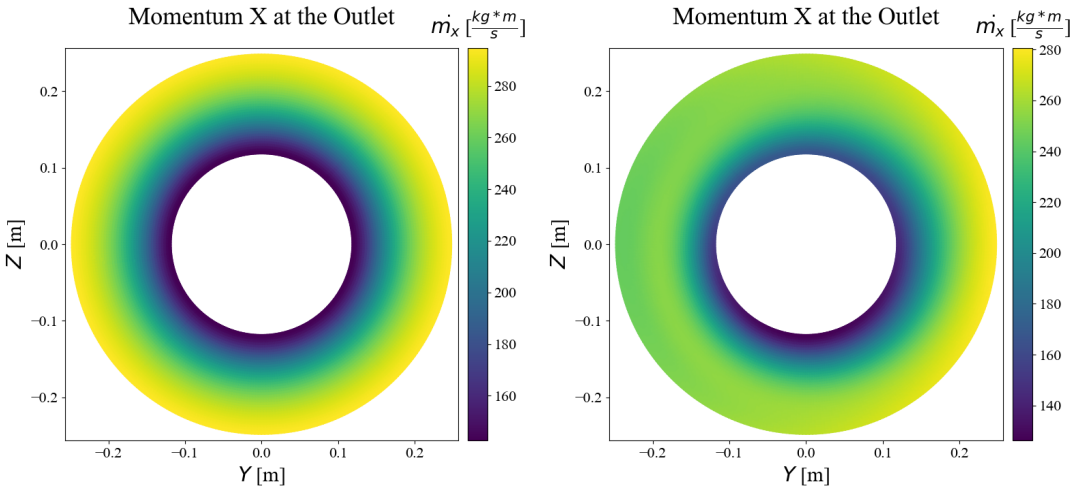

(a) Hall at the outlet (b) Thollet at the outlet

Figure 4.34: Comparison between Hall's an Thollet's resulting flows. Circular sections at the outlet circular section.

The intensity of this effect can be computed from the standard deviation of different variables extracted at the same 3 span location. A deviation of up to 17.4% can be captured for Thollet's simulation. This error is generally less influential for the total thermodynamic variables than for static ones. Moreover it is usually localized in the

blade region, while it seems to decrease proceeding towards the exit section.

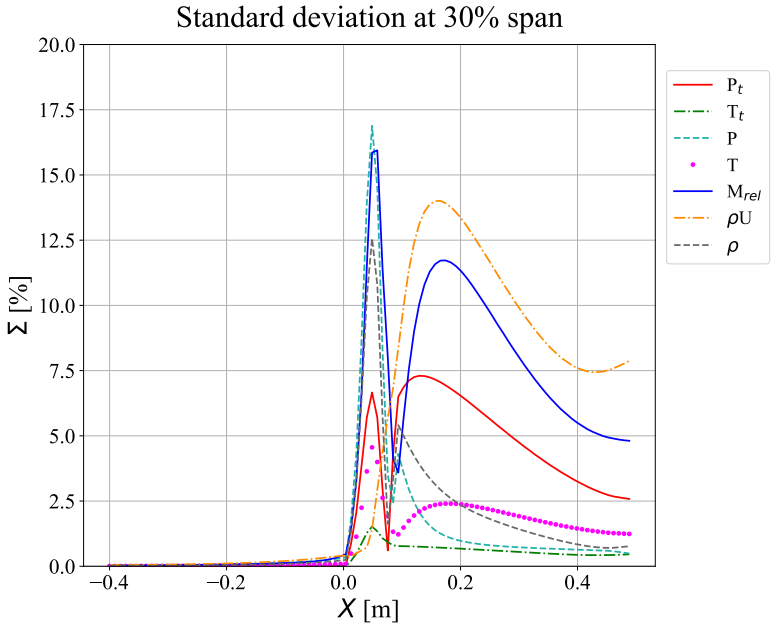

Figure 4.35: Flow variables standard deviation at 30% of the span.

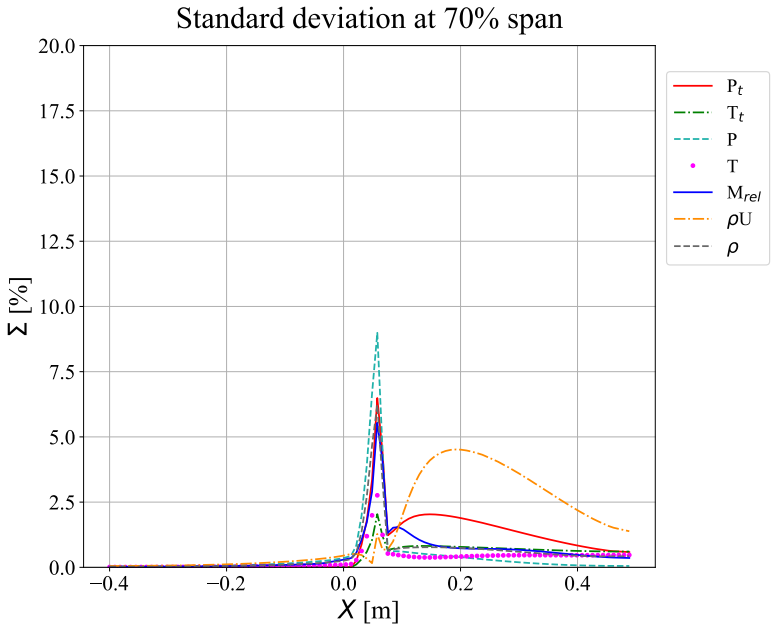

Figure 4.36: Flow variables standard deviation at 70% of the span.

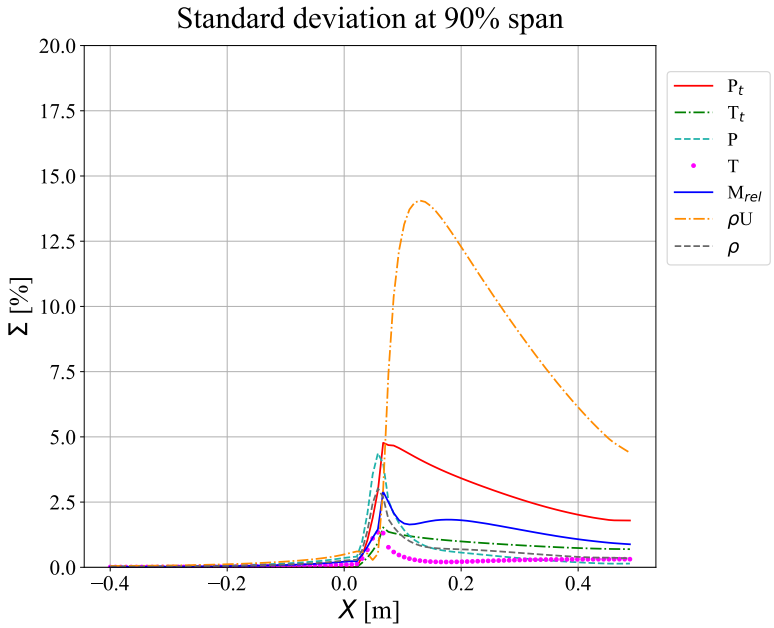

Figure 4.37: Flow variables standard deviation at 90% of the span.

In light of these findings the validity of the current Thollet's BFM and its applicability to blade shape design has been questioned. The local resolution of the current code implementation is not satisfying the accuracy requirement for shape 3D shape design since it is unable to capture neither the LE influence over shock waves nor the correct effect of blockage factor. According to the reported limitations some future development has been theorized in chapter 6.

Despite the level of local inaccuracy shown, according to the overall close match of efficiency and mass flow rate, the Thollet's full-annulus formulation has been used to perform a sensitivity analysis. It has then been compared to the overall less accurate Hall's model in order to understand whether without local flow stratification BFM can currently be applied in design optimization. Results for this evaluation are reported in the following chapter.

5 | Sensitivity analysis

Before being able to perform an optimization cycle, a sensitivity analysis must be carried out. Such study is necessary to understand whether or not BFM is a valid alternative to classical CFD methods for gradient based blade shape optimization. This procedure moreover reduces the number of significant design variables requested for the optimization, as it highlightsvariables of most significance to the objective.

To check if BFM fits gradient based blade optimization, the objective functions derivatives over the design variables are compared between CFX and BFM results. If they do not show similar trends then a subsequent optimization with BFM would not produce reasonable geometries. Initially the periodic simulation was chosen to perform the sensitivity analysis. The decision was driven by the time required by single passage simulation. After the discovery of periodic boundary conditions issues in SU2, the writer decided to carry out the sensitivity analysis using full-annulus simulations, trying to avoid numerical error introduced in the periodic domain at the cost of minor time efficiency.

Due to the computational cost associated with full-annulus simulations, a limited number of design variables have been selected for the study. The sensitivity analysis was carried out for both Hall's and Thollet's model to confront the results and to evaluate their state of the art applicability in the design phase. The selected objective function is the total-to-total isentropic efficiency, as this is a good indicator of the overall design variables influence.

With the aim to perform a initial sensitivity analysis it has been decided to adopt finite forward differences as derivatives approximation. The derivatives are then computed according to:

$$\frac{\partial F}{\partial \gamma} = \frac{F(\gamma + h) - F(\gamma)}{h} + o(h) \tag{5.1}$$

where F is the objective function (the efficiency in this case), γ is a generic design variable and h is the prescribed step size. This derivative approximation is less accurate than a centered finite difference or other possible methods such ax complex step, but it has been

selected anyway because it requires just two points to be estimated, thus a limited number of simulations.

A limitation to be accounted for in the use of finite difference is the cancellation error arising from too small step size. The step should be selected as a trade-off between the truncation error, induced by high values, and the cancellation error, produced by small ones. An analysis over the design space should be performed to obtain an idea of the best step size for the problem. Clearly this is not feasible with the computational cost associated with CFX simulation. It has then been decided to adopt the default step from Dakota [3]. The program uses an h value equal to the maximum between 0.01% of the selected parameter and 10^{-4}, as this has been reported to be a good compromise for the errors.

Between the different possible SA procedures in Dakota, a centered parameter study was adopted. With this choice each variable is studied separately from the other, neglecting the possible cross effect. It was selected because it requires only $N \times M$ simulations, where N i the number of variables and M is the number of of points needed for the derivative estimation. It is in fact unfeasible to perform a complete grid study of all variables due to the computational cost being M^N [3].

Since the LE and TE are the critical regions for BFM formulations and they strongly affect the shock wave influence, the design variables selected for this study, according to Parablade, are:

- the curvature radii at the 4 design sections LE and TE;
- the tangent distances at the 4 design sections LE and TE.

The analysis results reported in Fig.5.1 show that BFM is able to capture the most significant design variables, but it severely underestimates their effect . Both CFX and BFM agree that the tangent values at the LE and TE of the blade do not influence the overall efficiency. As such they can be initially omitted from design optimization variables. On the other hand, looking at the LE curvature radii influence, a certain level of error can be observed: even if they both recognize this as the most influential value, a substantial difference is found in the gradient absolute value. CFX highlights the efficiency dependency from LE supersonic conditions. It is in fact shown how the major influence is located near the tip, where strong oblique shock waves develop. The curvature radius change does indeed affect the shock distance and subsequently the impingement point on the nearby blades, as shown in Fig.4.3. This in turn affects the boundary layer separation on the suction side and the resulting machine efficiency. This effect decreases

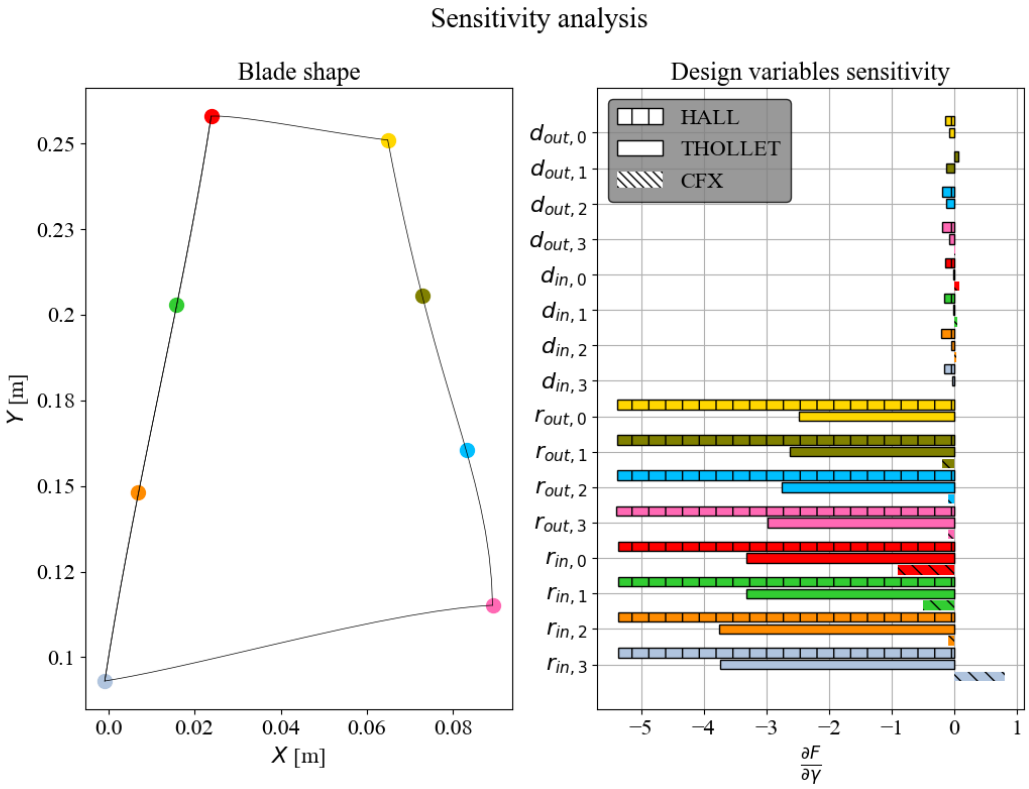

Figure 5.1: Sensitivity analysis.

near the hub where the the relative flow velocity is smaller and the blade profiles are less staggered. BFM shows a negative curvature radius influence instead, as it does not take into consideration the supersonic behaviour of the flow.

By comparing the results obtained for Hall's and Thollet's models, it is clear that the first one is less accurate. The curvature radius at the LE and TE can affect the BFM solution either in terms of normal force, or as blockage factor as reported in eq.2.13. In the first case the effect is linked to the change of local angle of attack δ. This is influenced by both edges at the same manner, and leads to constant finite differences across the span. By contrast the blockage factor, present only in Thollet's formulation, appears to damp the negative BFM derivatives, producing lower SA errors with respect to Hall's model. Despite the improvement Thollet's model is still not able to reproduce the CFX results. Another noticeable mismatch can be found at the TE. Here CFX shows little sensitivity to curvature radii since the flow has already separated and the pressure is no more recovered, thus the shape has lower impact. Since BFM does not consider the actual physical blade presence, but rather inserts the BL effect with the flat plate model, no shock wave impingement and separation are accounted for. Consequently the design variables influence in the TE region shows similar effect as at the LE, leading to

an incorrect gradient estimation

Due to the several limitations and shortcomings encountered during this work, as well as the discouraging results obtained from SA, it was not possible to perform optimization run. Nonetheless a gradient based constrained optimization has been implemented in the workflow using Dakota, allowing for future optimization studies.

6 | Conclusions and way forward

The target of this thesis was to develop an automated workflow for fan stage design using BFM, and to verify its applicability to real life case. The result was a clear and segmented python process, which encloses several features such as initial design script, automatic meshing and sensitivity analysis.

Following the thesis layout, a first introduction to the body force model reasons and hypothesis has been presented, as well as the possible application in the design process for fan blades. After that, the virtual environment and software settings to reproduce this work has been fully reported. The complete script package can be downloaded from the bitbucket repositories [11] that can be found at

$$https://bitbucket.org/gmrx96/workspace/projects/BFM$$

The process was then applied to NASA Rotor67 to verify its efficiency and effectiveness, as well as evaluating the solver quality. With this application it has been shown the good agreement between BFM and high-fidelity CFD for preliminary design. Lastly a brief sensitivity analysis has been performed in order to assess possible optimization applicability. This thesis has also been able to spot some major flows and development areas that, due to time constraints, were not possible to be explored in the present work.

While BFM was characterized as not being able to be used as a fan blade shape design tool at the time being it was possible to determine the main development areas to be implemented in the future. The author is confident that such correction could drastically improve this method possibilities for fan design.

From the obtained results the research questions can be answered:

1. **What are the differences between BFM and physical blade transonic fan simulations results?**

   (a) **Which level of domain discretization is required to achieve grid convergence in BFM?** As found in grid convergence study in section 4.2.4 a

relative coarse mesh can be used for BFM simulation, especially capitalizing on radial discretization, which was shown being not influential for the case at hand. The most important discretization direction is the axial one, which will be the main driver for mesh refinement. While tangential refinement was expected not to influence too much the results quality, some unfortunate periodicity issues were encountered. This limitation made the use a single tangential cell counterproductive and forced the use of a fine full-annulus grid.

(b) **What discrepancies can be found in terms of global and local flow characteristics?** Both Hall's and Thollet's formulations for the BFM appear to reproduce the global flow behaviour with a reasonable level of error. Between the two, the second is better at capturing the expected mass flow rate thanks to the blockage model implementation, but shows non physical tangential flow stratification, leading to higher efficiency discrepancy. Both models can be reasonably adopted for preliminary design, but the major drawback of not being able to reproduce inlet shock does prevent from blade shape design optimization at the moment.

(c) **How do the simulation results differ between the two BFM implementations in SU2? What are the results differences between single-passage and full-annulus simulations?** The two methods mainly differ in terms of resulting mass flow. While Thollet is closer to CFX value thanks to blockage factor, it still overestimates $\dot{m}$ by couple percentage points. By performing both periodic single-passage and full-annulus domain simulations, significant difference were found in terms of mass flow rate and efficiency. This has been linked to the BC issue encountered in the current work. The difference is further stressed in Thollet's formulation, probably due to current blockage factor implementation in SU2 code, which induces flow stratification that fully develops in FA domain.

2. **To which degree can BFM approach be used for blade shape optimization in transonic fans?**

(a) **What level of time saving with respect to classical approach can be achieved with this model?** The works showed that a full-annulus simulation, with double the number of nodes of a single passage CFX, does take less time than the latter, clearly highlighting the advantage of the method. In the periodic BFM case, even if the computational efficiency should be higher, the time saving was limited to 1 order of magnitude due to low stability. As it

has been reported in the section 4.3.4 the author is confident that it will be possible to obtain a time saving of almost 4 order of magnitude in the future.

(b) **How close are the sensitivity analysis results from BFM and physical blade simulations?** While SA analysis was able to eliminate the influence of some of the design variables, it was impossible to correctly address the effect of the most important ones due to current model limitations. This prevented from performing a blade shape gradient based optimization.

(c) **Which features must be implemented in order to improve BFM design applicability?** According to the results obtained in this work 3 main development areas for the model have been identified:

i. SU2 stability should be improved both in terms of periodic and outlet boundary condition. This would result in greater time savings for the fast periodic BFM simulations;

ii. the Thollet's blockage factor implementation and the blade interpolation should be revised, with the aim of fixing the current flow stratification;

iii. the LE shock influence should be modeled in order to reliably apply the model to common transonic fan blades.

Of the three suggested point for model improvement the latter constitutes the most challenging one. While the first two can be addressed with a relative low effort, modeling inlet oblique shock wave influence without the blade presence appears to be a difficult task, as also reported in [23]. As Thollet speculated such losses relations may be obtained from future large CFD database creation or from a more complex modeling based on physical principles. In both cases significant research efforts are required.

Other possible method improvements not being discussed in this thesis can be the implementation of aerodynamic blockage factor to better capture the effective mass flow, the introduction of blade tip gap with a flow correction inserted in SU2 and more general profile losses model which takes into account also blade wake 3D effect.

Bibliography

[1] R. Agromayor, N. Anand, J.-D. Müller, M. Pini, and L. O. Nord. A unified geometry parametrization method for turbomachinery blades. *Science Direct*, 2020.

[2] ANSYS. Ansys® academic research mechanical and cfd, 2019. Release 2019R3.

[3] Brian M. Adams et al. . *Dakota, A Multilevel Parallel Object-Oriented Framework for Design Optimization, Parameter Estimation, Uncertainty Quantification, and Sensitivity Analysis: Version 6.15 User's Manual.* Sandia NationalLaboratories, Albuquerque, 11 2021.

[4] E. C. Bunschoten. Turbomachinery analysis and design using body-force modeling in su2. Master's thesis, Aerospace Propulsion and Power Engineering, TU Delft, 10 2020.

[5] I. B. Celik, U. Ghia, P. J. Roache, and C. J. Freitas. Procedure for estimation and reporting of uncertainty due to discretization in cfd applications. *Journal of fluids Engineering-Transactions of the ASME*, 2008.

[6] C. Chahine. *Multidisciplinary Design Optimisation of Aero-Engine Fan Blades*. PhD thesis, University of Oxford, February 2019.

[7] J. D. Denton. Some limitations of turbomachinery cfd. In *ASME Turbo Expo 2010: Power for Land, Sea, and Air*, pages 735–745. ASME, 2010.

[8] J. D. Denton. Multall: An open source, cfd based, turbomachinery design system. *ASME Turbo Expo 2017*, 2017.

[9] D.K.Hall. *Analysis of civil aircraft propulsors with boundary layer ingestion*. PhD thesis, Department of Aeronautics and Astronautics, Massachusetts Institute of Technology, February 2015.

[10] Gabriele Morvillo. Application of body force modeling to aeroengine fan blade design - executive summary, 2022.

[11] Gabriele Morvillo. Bfm fan design. `https://www.grc.nasa.gov/www/wind/valid/tutorial/spatconv.html`, 2022. Last checked: 2022-03-31.

[12] C. Hughes. The promise and challenges of ultra high bypass ratio engine technology and integration. *Aero Sciences Meeting*, 2011.

[13] A. P. Kottapalli. *Development of a body force model for centrifugal compressors*. PhD thesis, Department of Aeronautics and Astronautics, Massachusetts Institute of Technology, September 2013.

[14] M. Latour. Body force modeling of axial turbomachinery for analysis and design optimization. Master's thesis, Aerospace Propulsion and Power Engineering, TU Delf, 4 2020.

[15] J. Li, H. Chen, Y. Liu, J. Wang, and X. Yang. Aerodynamic design and optimization of a high-loaded axial fan stage using a curvature control method. *Journal of Mechanical Science and Technology*, 2019.

[16] F. Marble. Three dimensional flow in turbomachines,. *High Speed Aerodynamics and Jet Propulsion*, page 83.166, 1964.

[17] Microsoft. Wsl. `https://docs.microsoft.com/en-us/windows/wsl/install`, 2022. Last checked: 2022-02-24.

[18] NASA. Examining spatial grid convergence. `https://www.grc.nasa.gov/www/wind/valid/tutorial/spatconv.html`, 2021. Last checked: 2022-02-24.

[19] A. Peters. *Ultra-Short Nacelles for Low Fan Pressure Ratio Propulsors*. PhD thesis, Department of Aeronautics and Astronautics, Massachusetts Institute of Technology, February 2014.

[20] W. A. Sorensen. *A Body Force Model for Cavitating Inducers in Rocket Engine Turbopumps*. PhD thesis, Department of Aeronautics and Astronautics, Massachusetts Institute of Technology, September 2014.

[21] A. J. Strazisar, J. R.Wood, M. D. Hathaway, and K. L. Suder. Laser anemometer measurements in a transonic axial-flow fan rotor. Technical Report 2879, NASA, 11 1989.

[22] SU2 development team. Su2 issues and development areas. `https://github.com/su2code/SU2/issues/1487`, 2022. Last checked: 2022-02-24.

[23] W. Thollet. *Body force modeling of fan-airframe interactions*. PhD thesis, ED MEGeP : Dynamique des fluides, Université Fédérale de Toulouse, July 2017.

[24] Timofey Mukha. Turbulucid. `https://github.com/timofeymukha/turbulucid`, 2021. Last checked: 2022-02-24.

[25] A. Uranga, M. Drela, E. M. Greitzer, N. A. Titchener, M. K. Lieu, N. M. Siu, A. C. Huangk, G. M. Gatlin, and J. A. Hannon. Preliminary experimental assessment of the boundary layer ingestion benefit for the d8 aircraft. *52nd Aerospace Sciences Meeting*, 2014.

[26] Y.Gong. *A computational model for rotating stall and inlet distortions in multistage compressors*. PhD thesis, Department of Aeronautics and Astronautics, Massachusetts Institute of Technology, February 1999.

A | Configuration files

In this Appendix the initial configuration file used for the NASA Rotor67 study is reported. More information about this input file and the one for designing a new geometry can be found at the repository [citare la mia repository]. The initial text file to be compiled is subdivided into 5 blocks. The block subdivision helps to tune the program according to the problem to be represented.

Table A.1: Machine data.

Design variable	Type/Value
Geometry	Existing
Machine Name	Rotor67
Stage number	1
Row number	1
Dimensions	3
Machine type	Compressor
RPM	16043
$\boldsymbol{P_{t,in}}$	101325 $[Pa]$
$\boldsymbol{T_{t,in}}$	288.15 $[K]$
$\boldsymbol{P_{out}}$	126644 $[Pa]$

Table A.2: Program options.

Design variable	Type/Value
Plot blade	No
Mesh for BFM	Yes
BFM formulation	Thollet
Sensitivity	No
Optimization	No
CFX postprocess	No
BFM postprocess	Yes
Plot results	Yes

Table A.3: Freestream properties.

Design variable	Type/Value
$\boldsymbol{T_{in}}$	271.52 $[K]$
$\boldsymbol{P_{in}}$	82242.7 $[Pa]$
$\boldsymbol{\rho_{in}}$	1.055 $[kg\,m^{-3}]$
$\boldsymbol{M_{in}}$	0.554
$\boldsymbol{u_{in}}$	183.083 $[m\,s^{-1}]$

Table A.4: Gas properties.

Design variable	Type/Value
R	287.15 $[J\,kg^{-1}\,K^{-1}]$
$\boldsymbol{\gamma}$	1.4
Cp	1006 $[J\,kg^{-1}\,K^{-1}]$

Table A.5: Mesh parameters.

Design variable	Type/Value
Wedge angle	3 $[degrees]$
Axial points	100
Radial points	40
Tangential points	3
First offset	$1.5e^{-5}$
Inlet factor	1.2
LE factor	1.2
TE factor	1.2
Outlet factor	1.2

In case of a design geometry the file has the same structure but in the machine data block must be added the turbomachinery parameters of merit:

- the reaction rate χ;
- the flow coefficient ϕ;
- the work coefficient ψ.

Moreover a set of geometry parameters related to the machine must be given in order to operate the preliminary shape definition in Meangen.

In order to produce the geometry from Parablade it is also necessary to add to the path a configuration file containing the blade referred to in Table A.1. It has to be obtained beforehand as described in chapter 3 from the blade matching procedure. Such file contains the following information for Parablade:

Table A.6: Parablade configuration file.

Design variable	Values
Blades number	22
Sections	11
$\boldsymbol{X_{LE}}$	$-0.0012,\ 0.0062,\ 0.0171,\ 0.0238$
$\boldsymbol{Y_{LE}}$	$-0.0001,\ 0.0008,\ -0.0076,\ 0.0003,\ 0.0007$
$\boldsymbol{Z_{LE}}$	$0.0957,\ 0.1520,\ 0.2044,\ 0.2553$
$\boldsymbol{X_{TE}}$	$0.0897,\ 0.0895,\ 0.0777,\ 0.0690,\ 0.0652$
$\boldsymbol{Z_{TE}}$	$0.1179,\ 0.1617,\ 0.2011,\ 0.2482$
$\boldsymbol{X_{hub}}$	$0.0228,\ 0.0654$
$\boldsymbol{Z_{hub}}$	$0.1005,\ 0.1166$
$\boldsymbol{X_{shroud}}$	$0.0303,\ 0.0509$
$\boldsymbol{Z_{shroud}}$	$0.2558,\ 0.2504$
Stagger	$12.8030,\ 23.8062,\ 48.9394,\ 57.4845,\ 63.1321$
$\boldsymbol{\Theta_{in}}$	$37.8894,\ 40.0863,\ 40.3733,\ 30.0402$
$\boldsymbol{\Theta_{out}}$	$-19.3142,\ 15.0711,\ 40.0941,\ 44.8254$
$\boldsymbol{r_{in}}$	$0.0007,\ 0.0019,\ 0.0020,\ 0.0009$
$\boldsymbol{r_{in}}$	$0.002,\ 0.0001,\ 0.0001,\ 0.0004$
$\boldsymbol{d_{in}}$	$0.3372,\ 0.2647,\ 0.3325,\ 0.3613$
$\boldsymbol{d_{in}}$	$0.3611,\ 0.3233,\ 0.5112,\ 0.4836$
$\boldsymbol{t_{up,1}}$	$0.0026,\ 0.0191,\ 0.0001,\ 0.02314$
$\boldsymbol{t_{up,2}}$	$0.0178,\ 0.0225,\ 0.0198,\ 0.0350$
$\boldsymbol{t_{up,3}}$	$0.0426,\ 0.0201,\ 0.0132,\ 0.0245$
$\boldsymbol{t_{up,4}}$	$0.0535,\ 0.0157,\ 0.0288,\ 0.0104$
$\boldsymbol{t_{up,5}}$	$0.0379,\ 0.0087,\ 0.0001,\ 0.0243$
$\boldsymbol{t_{up,6}}$	$0.0195,\ 0.0205,\ 0.0001,\ 0.0057$
$\boldsymbol{t_{low,1}}$	$0.0141,\ 0.0226,\ 0.0001,\ 0.0001$
$\boldsymbol{t_{low,2}}$	$0.0327,\ 0.0456,\ 0.0001,\ 0.0001$
$\boldsymbol{t_{low,3}}$	$0.0403,\ 0.0833,\ 0.0054,\ 0.0325$
$\boldsymbol{t_{low,4}}$	$0.0362,\ 0.0750,\ 0.0388,\ 0.0419$
$\boldsymbol{t_{low,5}}$	$0.0305,\ 0.0494,\ 0.0465,\ 0.0376$
$\boldsymbol{t_{low,6}}$	$0.0004,\ 0.0230,\ 0.0132,\ 0.0237$

B | GCI evaluation

In order to perform the grid convergence study a standardized procedure should be followed such that results are easily interpreted. According to this need the widely diffused Roche methodology was selected. This methodology is widely documented in [5] and [18].

The aim of this process is to obtain the GCI (Grid Convergence Index), a quantitative measure of discretization error introduced in a certain grid with respect to the expected asymptotic numerical value. A successful analysis should produce a decreasing GCI for progressively more refined grids. To apply this method at least 3 levels of grid refinements are required. In the case studied it has been decided to perform a grid convergence study for each direction separately, as shown in table 4.10, instead of a global one. This was done to have better insight of each direction influence over the results, and also to find the most efficient mesh for optimization purposes. It was in fact necessary to obtain a relatively accurate mesh with the minimum number of elements to speed up the simulations.

The Roche method is based on the refinement factor notion in order to estimate the convergence order of the method:

$$r_{i+1,i} = \frac{h_{i+1}}{h_i} \quad with\ i = 1, 2 \tag{B.1}$$

where the lower subscripts represent the more refined grids. With the refinement ratio and the evaluated output function φ, it is possible to estimate the convergence order p of the studied direction:

$$p = \frac{1}{ln(r_{2,1})} \left| ln \left| \frac{\varphi_3 - \varphi_2}{\varphi_2 - \varphi_1} \right| + q(p) \right| \tag{B.2}$$

where

$$q(p) = ln \left(\frac{r_{2,1}^p - sgn(\frac{\varphi_3 - \varphi_2}{\varphi_2 - \varphi_1})}{r_{3,2}^p - sgn(\frac{\varphi_3 - \varphi_2}{\varphi_2 - \varphi_1})} \right) \tag{B.3}$$

From the convergence order the extrapolated value for convergence can be obtained using

Richardson's formula.

$$\varphi_{extr} = \frac{r_{2,1}^{p}\varphi_1 - \varphi_2}{r_{2,1}^{p} - 1} \tag{B.4}$$

According to this value the discretization error e_{extr} associated to each grid can be computed as well as the GCI in order to evaluate the quality of the mesh:

$$e_{extr,j} = \left| \frac{\varphi_{extr} - \varphi_j}{\varphi_{extr}} \right| \quad with\, j = 1, 2, 3 \tag{B.5}$$

$$GCI_{i+1,i} = \frac{1.25 \left| \frac{\varphi_i - \varphi_{i+1}}{\varphi_i} \right|}{r_{i+1,i} - 1} \tag{B.6}$$

According to the methodology presented the grid convergence was evaluated for both mass flow and efficiency parameters of merit. The obtained results are reported below for each direction. If a global GCI is requested it is possible to estimate it by a simple superposition of the values along each axis.

Table B.1: Periodic Thollet mass flow grid convergence.

	Ax	Rad	Tan
p	2.38	1.83	8.01
$\boldsymbol{\varphi_{extr}}$	34.84	33.05	33.80
$\boldsymbol{err_3}$	3.61%	1.62%	0.62%
$\boldsymbol{err_2}$	1.82%	1.17%	0.02%
$\boldsymbol{err_1}$	1.07%	0.67%	$9e^{-5}$%
$\boldsymbol{GCI_{32}}$	2.32	0.50	$3e^{-3}$
$\boldsymbol{GCI_{21}}$	1.35	0.86	$1e^{-4}$

Table B.2: Periodic Thollet efficiency grid convergence.

	Ax	Rad	Tan
p	3.38	14.06	1.82
$\boldsymbol{\varphi_{extr}}$	85.41%	83.68%	93.71%
$\boldsymbol{err_3}$	1.90%	0.14%	9.62%
$\boldsymbol{err_2}$	0.72%	0.15%	2.72%
$\boldsymbol{err_1}$	0.34%	$3e^{-3}$%	1.31%
$\boldsymbol{GCI_{32}}$	0.91	$6e^{-5}$	3.51
$\boldsymbol{GCI_{21}}$	0.42	$3e^{-3}$	1.65

Table B.3: Full-annulus Thollet mass flow grid convergence.

	Ax	Rad	Tan
p	2.84	2.40	4.60
φ_{extr}	35.38	35.00	34.92
err_3	1.19%	$6e^{-3}$%	0.11%
err_2	0.53%	0.03%	0.07%
err_1	0.28%	0.01%	0.01%
GCI_{32}	0.66	0.03	$2e^{-3}$
GCI_{21}	0.35	0.02	0.01

Table B.4: Full-annulus Thollet efficiency grid convergence.

	Ax	Rad	Tan
p	3.00	5.60	1.16
φ_{extr}	92.44%	91.12%	98.24%
err_3	1.11%	0.32%	6.96%
err_2	0.47%	0.23%	3.12%
err_1	0.24%	0.05%	1.95%
GCI_{32}	0.59	0.01	4.03
GCI_{21}	0.30	0.06	2.49

Table B.5: Periodic Hall mass flow grid convergence.

	Ax	Rad	Tan
p	2.30	1.89	5.11
φ_{extr}	37.31	35.34	36.06
err_3	4.27%	1.08%	1.00%
err_2	2.20%	0.77%	0.03%
err_1	1.39%	0.45%	$3e^{-3}$%
GCI_{32}	2.82	0.32	0.04
GCI_{21}	1.67	0.56	$5e^{-3}$

Table B.6: Periodic Hall efficiency grid convergence.

	Ax	Rad	Tan
p	2.52	8.87	1.89
φ_{extr}	86.47%	83.61%	91.54%
err_3	3.03%	0.28%	8.41%
err_2	1.47%	0.23%	2.27%
err_1	0.84%	0.02%	1.06%
GCI_{32}	1.87	$2E^{-3}$	2.91
GCI_{21}	1.06	0.02	1.34

Table B.7: Full-annulus Hall mass flow grid convergence.

	Ax	Rad	Tan
p	2.38	1.62	1.72
φ_{extr}	37.39	35.88	36.13
err_3	3.08%	0.98%	0.28%
err_2	1.55%	0.72%	0.18%
err_1	0.91%	0.45%	0.09%
GCI_{32}	1.97	0.35	0.06
GCI_{21}	1.15	0.56	0.11

Table B.8: Full-annulus Hall efficiency grid convergence.

	Ax	Rad	Tan
p	2.59	6.08	1.19
φ_{extr}	88.74%	86.46%	92.42%
err_3	2.25%	0.36%	6.24%
err_2	2.07%	0.25%	2.70%
err_1	0.60%	0.04%	1.67%
GCI_{32}	1.35	0.01	3.47
GCI_{21}	0.75	0.05	2.12

C | Plots

C.1. Radial plots

All the plots here represented show mass flow averaged values along x-axis and radial position along y-axis

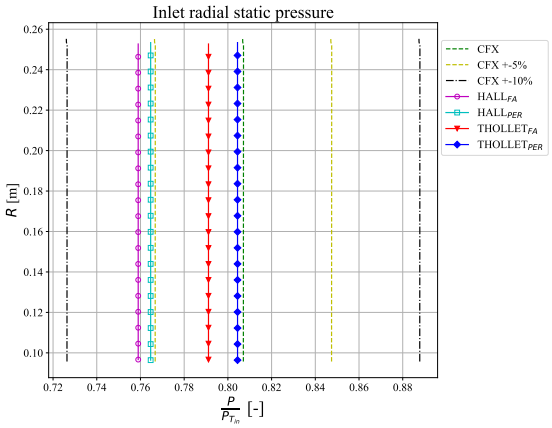

Figure C.1: Radial pressure trend at the inlet

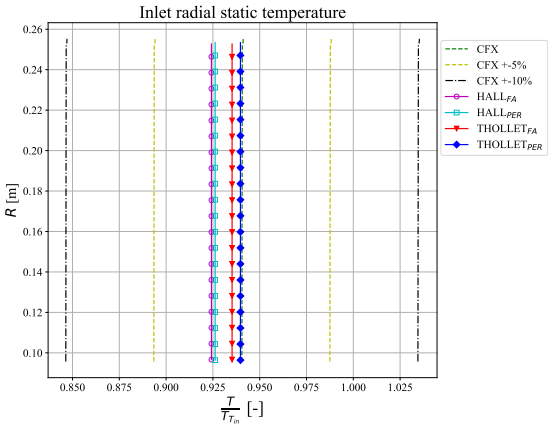

Figure C.2: Radial temperature trend at the inlet.

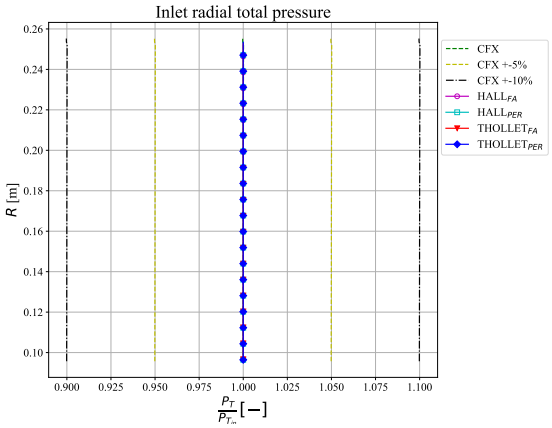

Figure C.3: Radial total pressure trend at the inlet.

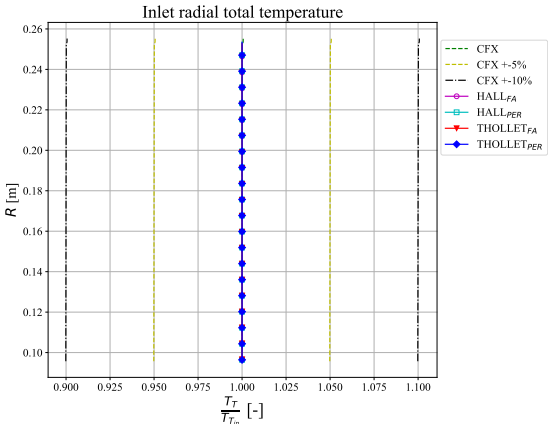

Figure C.4: Radial total temperature trend at the inlet.

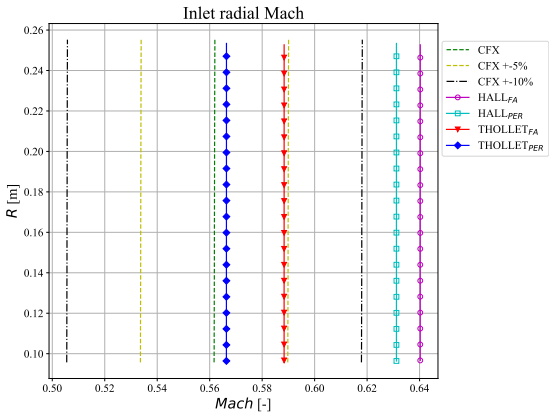

Figure C.5: Radial Mach trend at the inlet.

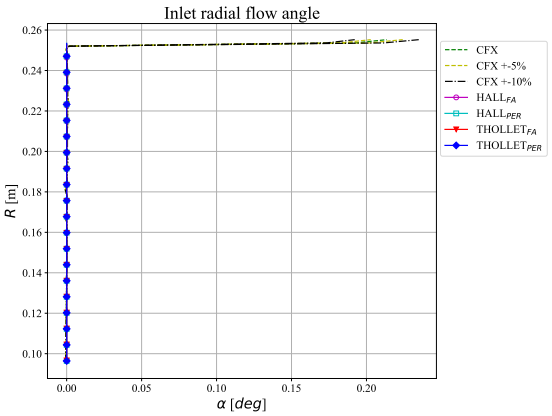

Figure C.6: Radial flow angle trend at the inlet.

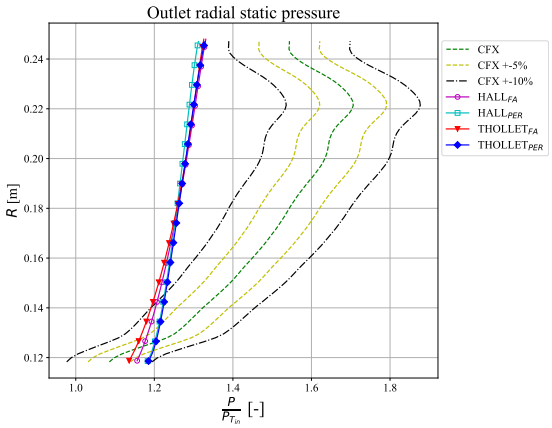

Figure C.7: Radial pressure trend at the outlet.

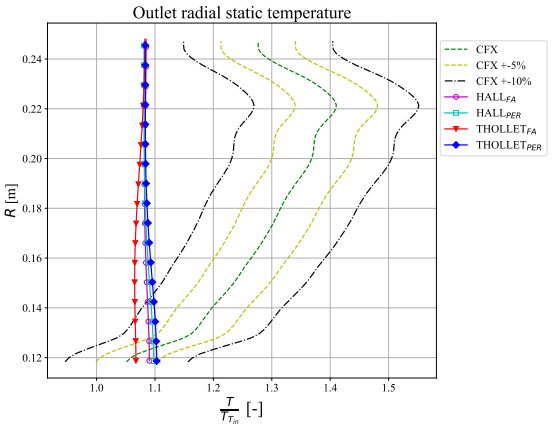

Figure C.8: Radial temperature trend at the outlet.

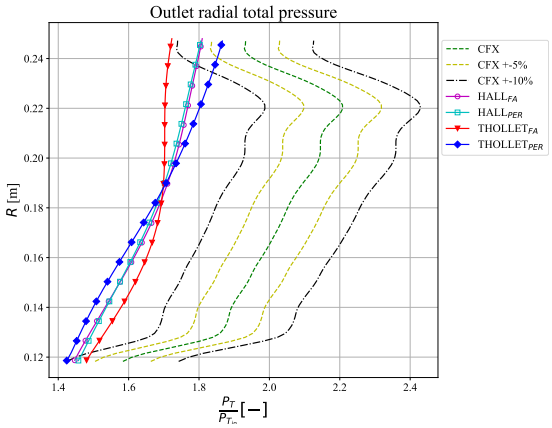

Figure C.9: Radial total pressure trend at the outlet.

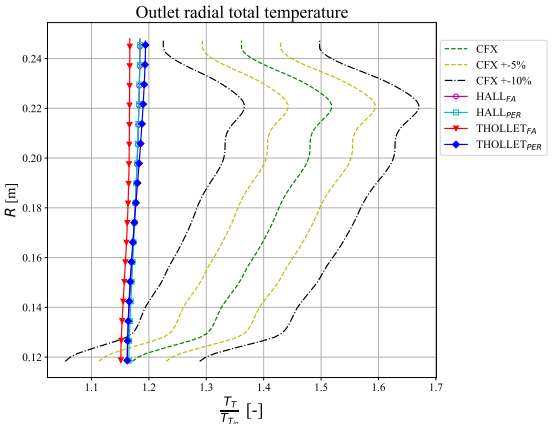

Figure C.10: Radial total temperature trend at the outlet.

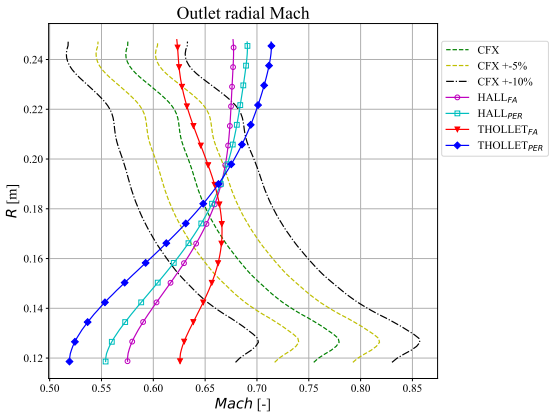

Figure C.11: Radial Mach trend at the outlet.

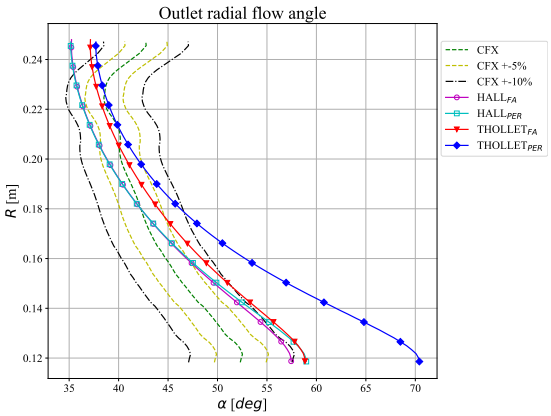

Figure C.12: Radial flow angle trend at the outlet.

C.2. Flow plots

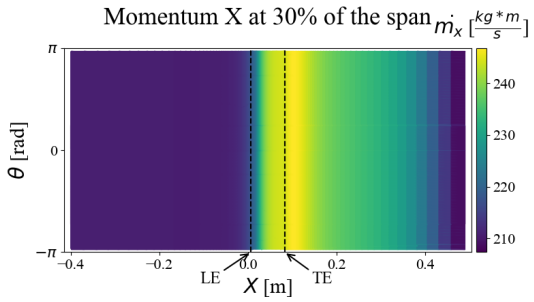

(a) Hall at 30% span

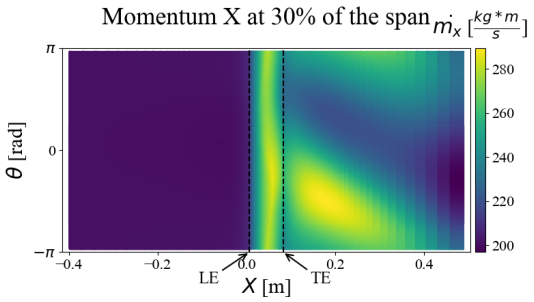

(b) Thollet at 30% span

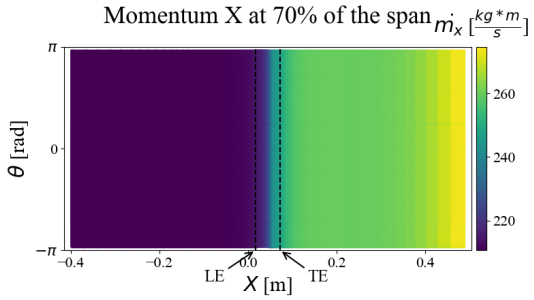

(c) Hall at 70% span

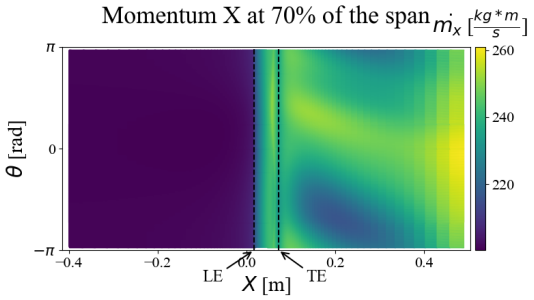

(d) Thollet at 70% span

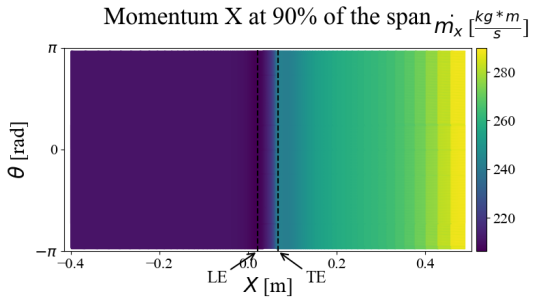

(e) Hall at 90% span

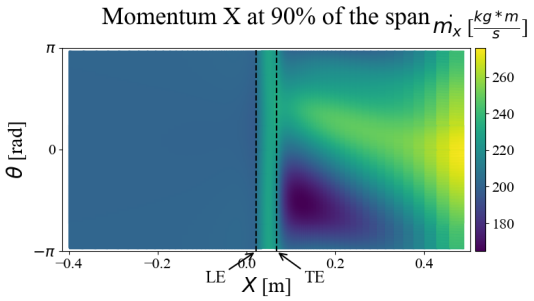

(f) Thollet at 90% span

Figure C.13: Momentum comparison between Hall and Thollet. Blade-to-blade plane view at different spanwise sections.

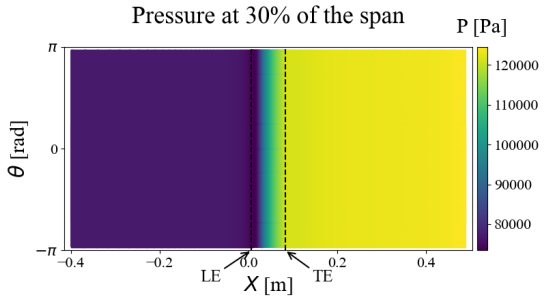

(a) Hall at 30% span

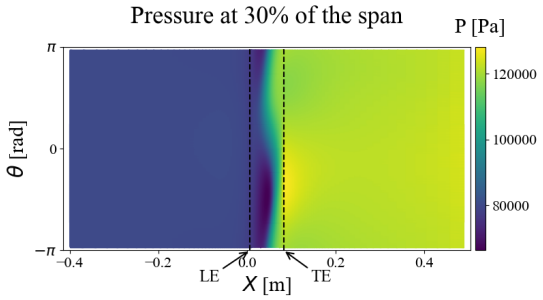

(b) Thollet at 30% span

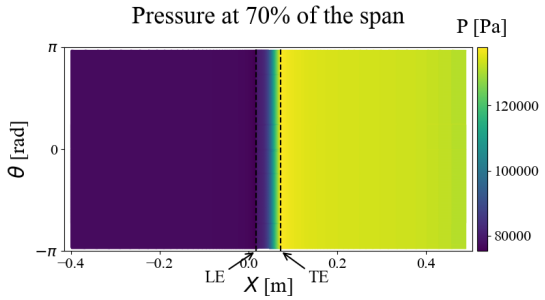

(c) Hall at 70% span

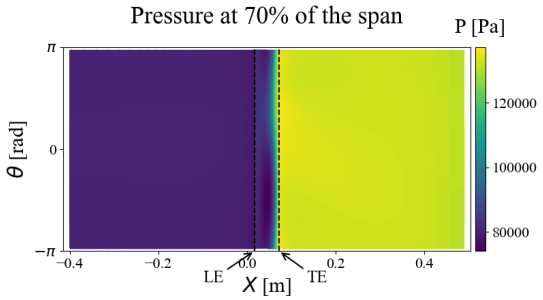

(d) Thollet at 70% span

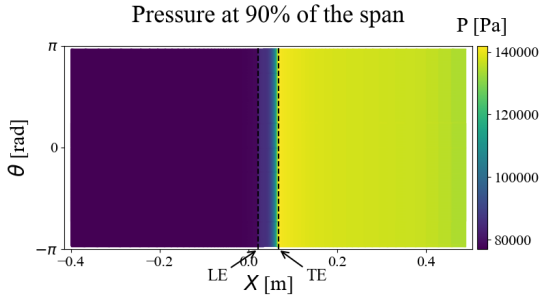

(e) Hall at 90% span

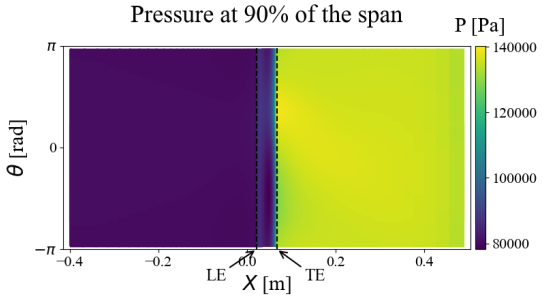

(f) Thollet at 90% span

Figure C.14: Pressure comparison between Hall and Thollet. Blade-to-blade plane view at different spanwise sections.

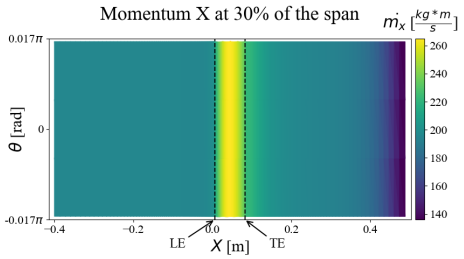

(a) Periodic Thollet at 30% span

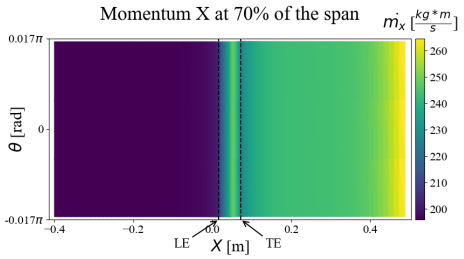

(b) Periodic Thollet at 70% span

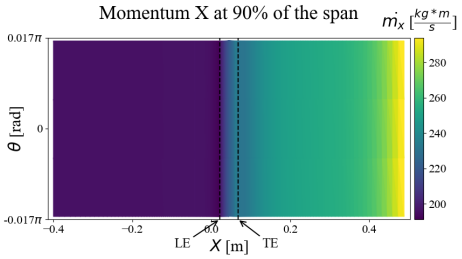

(c) Periodic Thollet at 90% span

Figure C.15: Periodic Thollet's momentum. Blade-to-blade plane view at different spanwise sections.

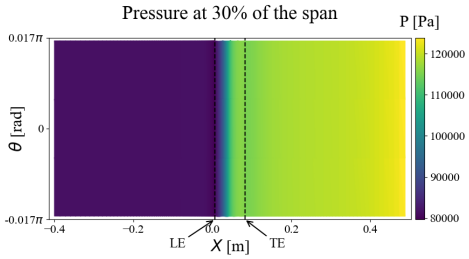

(a) Periodic Thollet at 30% span

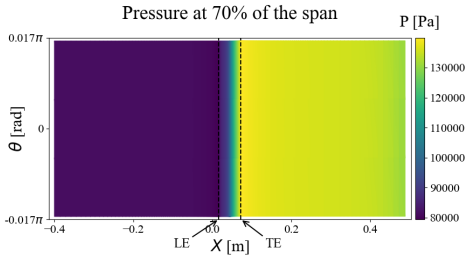

(b) Periodic Thollet at 70% span

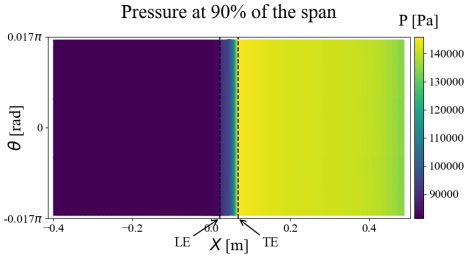

(c) Periodic Thollet at 90% span

Figure C.16: Periodic Thollet's pressure. Blade-to-blade plane view at different spanwise sections.

List of Figures

List of Tables

List of Symbols

Acronyms

BC	Boundary Condition
BL	Boundary Layer
BLI	Boundary Layer Ingestion
BFM	Body-Force Model
CFD	Computational Fluid Dynamics
CFL	Courant-Friedrichs-Lewy
GCI	Grid Convergence Index
HPC	High Performance Computing
LE	Leading Edge
PBC	Physical Blade Symulation
RANS	Reynolds Averaged Navier-Stokes
TE	Trailing Edge

Roman symbols

$\boldsymbol{b}$	Blockage factor	[-]
$\boldsymbol{c}$	Blade chord	[m]
$\boldsymbol{C_{Da}}$	Annulus drag coefficient	[-]
$\boldsymbol{C_{Ds}}$	Secondary drag coefficient	[-]
$\boldsymbol{C_f}$	Friction factor	[-]
$\boldsymbol{C_p}$	Isobaric specific heat	$[J\,kg^{-1}\,K^{-1}]$
$\boldsymbol{F}$	Force	$[kg\,m\,s^{-2}]$
$\boldsymbol{F_{BFM}}$	BFM momentum source	$[kg\,m^{-2}\,s^{-2}]$
$\boldsymbol{H}$	Boundary layer shape factros	[-]
$\boldsymbol{h}$	Blade height	[m]
$\boldsymbol{K_{Mach}}$	Compressible correction factor	[-]
$\boldsymbol{\dot{m}}$	Mass flow rate	$[kg\,s^{-1}]$

$\boldsymbol{N_{ax}}$	Axial nodes number	[-]
$\boldsymbol{N_b}$	Blades number	[-]
$\boldsymbol{N_{rad}}$	Radial nodes number	[-]
$\boldsymbol{N_{tan}}$	Tangential nodes number	[-]
$\boldsymbol{n}$	Camber normal vector	[-]
$\boldsymbol{P}$	Pressure	[Pa]
$\boldsymbol{Q_{BFM}}$	BFM energy source	$[J\,m^{-3}]$
$\boldsymbol{R}$	Gas constant	$[J\,kg^{-1}\,K^{-1}]$
$\boldsymbol{r}$	Radius	[m]
$\boldsymbol{Re}$	Reynolds number	[-]
$\boldsymbol{S_{BFM}}$	BFM mass source	$[kg\,m^{-3}]$
$\boldsymbol{s}$	Blade camberline pitch	[m]
$\boldsymbol{s'}$	Blade effective actual pitch	[m]
$\boldsymbol{T}$	Temperature	[K]
$\boldsymbol{t}$	Thickness	[m]
$\boldsymbol{u}$	Absolute velocity	$[m\,s^{-1}]$
$\boldsymbol{u_e}$	Exhaust velocity	$[m\,s^{-1}]$
$\boldsymbol{u_{fs}}$	Free stream velocity	$[m\,s^{-1}]$
$\boldsymbol{w}$	Relative velocity	$[m\,s^{-1}]$
$\boldsymbol{Y}$	Losses	[-]
$\boldsymbol{y+}$	First mesh element offset	[-]

Greek symbols

$\boldsymbol{\alpha}$	Absolute flow angle	[°]
$\boldsymbol{\beta}$	Relative flow angle	[°]
$\boldsymbol{\gamma}$	Specific heat ratio	[-]
$\boldsymbol{\delta}$	Angle of attack	[°]
$\boldsymbol{\epsilon}$	Tip gap	[m]
$\boldsymbol{\varepsilon}$	Error	[-]
$\boldsymbol{\eta}$	Efficiency	[-]
$\boldsymbol{\theta}$	Tangential angle	[°]
$\boldsymbol{\vartheta}$	Boundary layer momentum thickness	[m]
$\boldsymbol{\mu}$	Dynamic viscosity	$[Pa\,s]$
$\boldsymbol{\Pi}$	Pressure ratio	[-]

$\boldsymbol{\rho}$	Density	$[kg\,m^{-3}]$
$\boldsymbol{\sigma}$	Solidity	[-]
$\boldsymbol{\Sigma}$	Standard deviation	
$\boldsymbol{\tau}$	Stress tensor	[Pa]
$\boldsymbol{\phi}$	Flow coefficient	[-]
$\boldsymbol{\chi}$	Reaction rate	[-]
$\boldsymbol{\psi}$	Work coefficient	[-]
$\boldsymbol{\Omega}$	Rotation velocity	$[rad\,s^{-1}]$

Subscripts and abbreviations

$\boldsymbol{Ax}$	Axial
$\boldsymbol{corr}$	Corrected
$\boldsymbol{extr}$	Extrapolated
$\boldsymbol{FA}$	Full-annulus
$\boldsymbol{in}$	Inlet
$\boldsymbol{is}$	Isentropic
$\boldsymbol{iter}$	Iteration
$\boldsymbol{low}$	Lower face
$\boldsymbol{n}$	Normal
$\boldsymbol{out}$	Outlet
$\boldsymbol{PER}$	Periodic
$\boldsymbol{p}$	Parallel
$\boldsymbol{PS}$	Pressure side
$\boldsymbol{Rad}$	Radial
$\boldsymbol{ref}$	Reference
$\boldsymbol{rel}$	Relative
$\boldsymbol{SS}$	Suction side
$\boldsymbol{t}$	Total
$\boldsymbol{Tan}$	Tangential
$\boldsymbol{\theta}$	Tangential
$\boldsymbol{tot}$	Total
$\boldsymbol{TT}$	Total-to-total
$\boldsymbol{up}$	Upper face

Ringraziamenti

Vorrei, in questa fin troppo breve pagina, ringraziare tutti coloro che abbiano data la possibilità di conseguire questo incredibile obiettivo.

Ringrazio innanzitutto il Prof. Gaetani per avermi permesso di concludere il ciclo di studi con questa emozionante tesi e per la sua disponibilità. Devo anche ringraziare E.C. Bunschoten, mio supervisor presso la TU Delft, per la sua incrollabile dedizione e per tutto il tempo da lui dedicato a chiarire i miei dubbi e a guidarmi in questo arduo progetto.

Un ringraziamento speciale va alla mia famiglia, senza la quale non sarei qui in questo momento. Ringrazio i miei genitori che hanno sempre creduto in me e sostenendomi nei momenti bui. Vi sono incredibilmente riconoscente per tutti i vostri sacrifici volti a far realizzare i miei sogni. Grazie a mia sorella, che nonostante le litigate mi ha sempre "accudito" quando a casa, ai miei zii, che si sono sempre dimostrati disponibili nel momento del bisogno, ai nonni, che mi hanno reso la persona che sono ora e tra mille acciacchi non hanno mai smesso di fare il tifo per me.

Devo poi ringraziare Valentina per essermi stata vicina nonostante la distanza fisica, allietando le mie giornate con la sua voce e sostenendomi in questa ultima impresa. Ringrazio poi il gruppo di nerd di cui sono fiero di far parte, composto da Roberto, Marco, Alessandro e Gabriele, per la magica spensieratezza che riuscite a garantirmi.

Un grazie agli amici romani e agli ex colleghi Claudia, Giacomo, Vincenzo, Flavia e Pietro, che sebbene sia difficile vedere cercano ogni volta di organizzare in mille modi.

Un ringraziamento speciale va poi ai commensali della Casa dello Studente con cui ho condiviso innumerevoli cene e più birrette "tranquille" di quante probabilmente ricordi: Edoardo, Marcello, Dalila, Carlo, Lorenzo e Serena.

La mia gratudine va anche ai compagni di studio e progettisti di razzi Luca, Gianclaudio, Andrea, Filippo e Federico per avermi insegnato cosa significhi far parte di un ambiente stimolante come quello del Politecnico.

Ringrazio infine tutti i compagni di avventure con cui ho condiviso in parte il mio viaggio e con i quali, lungo il percorso, posso aver perso i rapporti. Farete sempre parte di me.